optical
tissue identification

G.C. Langhout

OPTICAL TISSUE IDENTIFICATION

WEEFSELDIFFERENTIATIE MET BEHULP VAN LICHT

PROEFSCHRIFT

ter verkrijging van
de graad van doctor aan de Universiteit Twente,
op gezag van de rector magnificus,
prof. dr. T.T.M. Palstra,
volgens besluit van het College voor Promoties
in het openbaar te verdedigen
op vrijdag 19 oktober 2018 om 12.45 uur

door

Gerrit Cornelis Langhout
geboren op 28 maart 1986
te Bergambacht

Dit proefschrift is goedgekeurd door de promotores;
Prof. dr. T.J.M. Ruers en prof. dr. H.J.C.M Sterenborg

De promotiecommissie

Voorzitter en secretaris:
Prof.dr.ir. J.W.M. Hilgenkamp   Universiteit Twente, Enschede
Promotores
Prof. dr. T.J.M. Ruers   Universiteit Twente, Enschede
Prof. dr. H.J.C.M. Sterenborg   Antoni van Leeuwenhoek en Amsterdam
      Universitair Medisch Centrum /AMC

Co-promotor:
Dr. K.F.D. Kuhlmann   Antoni van Leeuwenhoek, Amsterdam
Referent:
Prof. dr. A.J.M. Balm   Antoni van Leeuwenhoek, Amsterdam
Leden:
Prof. dr. M.M.A.E. Claessens   Universiteit Twente, Enschede
Prof. dr. S. Manohar   Universiteit Twente, Enschede
Prof. dr. J.A. van der Hage   Leids Universitair Medisch Centrum, Leiden
Prof. dr. B.H.W. Hendriks   Philips Research, Eindhoven
      en Technische Universiteit Delft

Contents

Kleur is de verwondering van het licht

Marc van Halsendaele

Summary

Summary

This thesis describes the evaluation of optical tissue identification for surgical applications. Three promising techniques are examined. After exploration of near infra-red fluorescence imaging and photoacoustic imaging, the thesis will focus on diffuse reflectance spectroscopy (DRS) for surgical tissue identification.

Chapter two describes the use of an intraoperative fluorescence camera in breast cancer phantoms. The technique provides the surgeon with an image overlay of the fluorescent contrast agent in phantoms mimicking absorption and scattering properties of human breast tissue. Important benefits and drawbacks are described.

Chapter three covers the application of photoacoustic imaging in surgery. The research is focused on lymph nodes in melanoma patients. Melanin, a strong optical absorber is imaged photoacoustically. The spectral identification of both tumor and blood vessels is demonstrated in phantoms and human lymph nodes ex vivo. The photoacoustic imager used is a reflective type, with the light source incorporated in the ultrasound detector.

Diffuse reflection spectroscopy is presented as an optical technique able to identify both tumor and vital surrounding structures like blood vessels and nerves. Colorectal tumors are frequently in close relation with vital structures. In oncologic rectum surgery, bladder- and sexual dysfunctions are both feared and high in incidence. Chapter four describes the identification of colorectal tumor using DRS.

Chapter five and six describe the identification of peripheral nerves in human during surgery. Peripheral nerves are often part of the vital structures surrounding a tumor. Ideally, image guided surgery depicts both tumor and vital surrounding tissue. Chapter five describes the identification of larger nerves as proof of principle. Chapter six is committed to the detection of smaller peripheral nerves.

Optimization and validation is not necessarily executed in humans in vivo. Logistically, and patient friendly, more suited for extensive measurements are a post mortem- or animal studies. However, DRS is subject to the morphological composition and biochemical make-up of the tissue, and both will change post mortem and may differ between human and animal. Chapter seven describes the optical similarities and differences between in vivo versus post mortem and human versus swine, focused on nerve identification.

In chapter eight we explore to possibilities to incorporate the DRS technique into a clinical device. We choose a bronchoscopic tool to fully utilize the small size and flexibility of the DRS optical fibers.

This thesis concludes with a general discussion and outlook on a use of optical tissue identification.

Samenvatting

Dit proefschrift beschrijft een onderzoek naar weefselherkenning met behulp van licht voor chirurgische toepassing. Drie veelbelovende technieken worden beschreven. Na verkenning van fluorescentie beeldvorming en fotoakoestiek wordt dieper ingegaan op diffuse reflectie spectroscopie (DRS) in de operatiekamer.

Hoofdstuk twee beschrijft de intra-operatieve toepassing van een camera gevoelig voor fluorescentie in het nabij infrarood, in borstkanker fantomen. Het fluorescente signaal van het contrastmiddel in fantomen met de optische eigenschappen van borstweefsel wordt als overlay gepresenteerd. Belangrijke voor- en nadelen worden besproken.

Hoofdstuk drie beslaat de chirurgische toepassing van fotoakoestiek. De focus ligt op lymfklieren van melanoompatienten. Melanine, dat licht krachtig absorbeert, wordt afgebeeld. Spectrale selectie stelt ons in staat het signaal van melanine en bloed te onderscheiden in fantomen en menselijke lymfklieren buiten het lichaam. We gebruikten een hand-held apparaat met de lichtbron verwerkt in de echokop.

Diffuse reflectie spectroscopie is een optische techniek welke is staat is om zowel tumor als belangrijke gezonde structuren, zoals zenuwen en bloedvaten te herkennen. Darmtumoren zijn vaak nauw verbonden met dergelijke structuren waardoor mictie- en seksuele problemen frequent voorkomen na een oncologische darmoperatie. In hoofdstuk vier wordt DRS gebruikt om tumoren van het rectum en dikke darm te identificeren.

Hoofdstuk vijf en zes beschrijven het intra-operatief identificeren van perifere zenuwen in patiënten. Zenuwen zijn vaak onderdeel van de vitale structuren met een nauwe relatie tot de tumor. Intra-operatieve beeldvorming zou bij voorkeur zowel de tumor als belangrijke omliggende structuren kunnen herkennen. Hoofdstuk vijf beschrijft het herkennen van grote zenuwen als 'proof of principle', het volgende hoofdstuk richt zich op het herkennen van kleinere zenuwtakjes.

Het optimaliseren en valideren van optische technieken hoeft niet uitsluitend in patiënten uitgevoerd te worden. Metingen post mortem of in varkens zijn met het oog op patiëntveiligheid en logistiek een alternatief. Echter, DRS is gebaseerd op verschillen in weefselsamenstelling, welke mogelijk veranderen na de dood en wellicht verschillen tussen mens en varken. Hoofdstuk zeven beschrijft optische verschillen en overeenkomsten tussen het weefsel van mens en varken, in vivo en post mortem, in het kader van zenuwherkenning.

In hoofdstuk acht verkennen we de mogelijkheden om de DRS techniek te verwerken in een klinische tool. We kiezen voor toepassing binnen de bronchoscopie om de minimale afmetingen en de flexibiliteit van de DRS vezels volledig te benutten.

Dit proefschrift wordt afgesloten met een discussie en vooruitzichten over het gebruik van weefselherkenning met behulp van licht.

General introduction

Introduction

The general concept in surgical oncology has always been resection of the tumor while conserving healthy tissue. Surgeons focus on optimizing the balance between wide (safe) resection and maximum conservation of tissue and function. Tumor involved margins are associated with an increased risk of local recurrence for several malignancies[1-5]. Improving functional outcome while maintaining radical resections demands precise information on shape and position of the tumor and the relation to important surrounding structures including nerves and vessels. For this information the surgeon relies on pre-operative imaging and his own real-time observations (visual and tactile) during the procedure. Pre-operative imaging, such as computed tomography (CT) and magnetic resonance imaging (MRI) have made impressive progress over the past decades in terms of availability and image quality[6,7]. For the vast majority of cases, pre-operative imaging is able to visualize both tumor and vital surrounding structures as well as their anatomical relation. On the other hand, the rise of laparoscopic techniques in the same period led to loss of tactile feedback and shifted visible feedback from direct vision to indirect camera images.

Despite the progress in imaging, everyday surgery heavily relies on the visual and tactile ability of the surgeon. This is because during surgery, the changes in tissue shape compromise the relation between the preoperative images and the actual situation in the surgical field. These shape changes are caused by the tissue manipulation during surgery, requiring either continuous intraoperative imaging or adaptation of the pre-operative image to keep up with the evolving surgical procedure. Up to now, only ultrasound (US) imaging fulfills these criteria. The advantage of intra-operative ultrasound in breast cancer surgery has recently been emphasized[8], however US focuses mainly on the tumor itself rather than the relation of the tumor with important surrounding structures[7,9,10].

To maximize functional outcome while maintaining radical excision, accurate identification of both tumor and vital surrounding structures is crucial. When using technical assistance
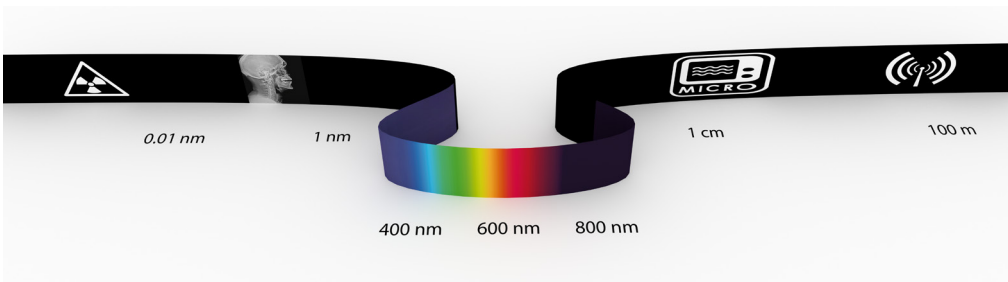
Figure 1.01. Light is electromagnetic radiation within a specific range of wavelengths. The human eye is sensitive to light with a wavelength of ~390 to ~740 nm. Presently, optical imaging is feasible using a spectral range from 300 nm to 2000 nm. Electromagnetic radiation with a wavelength shorter than visible light includes Röntgen and nuclear radiation. Microwaves and radio waves are electromagnetic radiation with a longer wavelength than visible light.

to facilitate identification, the information must be up to date or even real time to cope with the continuous tissue manipulation during surgery. Image guidance for surgical application should therefore effectuate a continuous insight/overview of the position of the tumor and its relation with surrounding healthy structures. To enhance acceptance, such a technique should have minimal influence on the existing workflow.

Optical imaging is considered safe, fast, inexpensive, makes use of non-ionizing radiation and enables real-time anatomical and functional imaging[11]. It has the potential to supply the surgeon with information about both the tumor and the surrounding structures. Therefore it promotes complete resection of otherwise challenging tumors while conserving the maximum function by meticulously avoiding damage to vital surrounding structures. The use of optical tissue identification in medical practice could include intra-operative guidance, image-guided biopsy and real time feedback in other minimal invasive procedures.

Basic principles of optical imaging

Registration of photons (light) is the essence of optical imaging. As the photons travel through the tissue, the light is influenced by absorption and scattering. Where absorption attenuates the light and scattering redirects it. Both absorption and scattering differ per tissue type and depend on the color (wavelength) of the light. The wavelengths (spectral range) used for optical imaging range from ultraviolet at ~ 300nm toward infrared at ~2 μm. Optical imaging outperforms the human eye by sensitivity, broader spectral range and higher spectral resolution (i.e. the ability to differentiate between light of different wavelengths). As a reference: in contrast to the wide spectral range of optical imaging, the human eye contains only 4 different photosensitive cells of which 3 are color specific, and is sensitive to light with a wavelength of 390 to 700 nm (Fig. 1.01).

Intra-operative optical techniques can be classified based on their spatial discrimination. Point measurements contain no spatial information and therefore supplies integrated values for the measured volume. Diffuse reflectance spectroscopy, as example of a point measurement, typically describes the measured volume as a whole, usually with detailed spectral information. Imaging techniques that produce an image contain spatial resolved information and therefore supply specific information for segments of the measured volume or area. A typical example for imaging is a camera, containing the relation in space to other pixels as well as (limited) information per pixel (grayscale intensity or red-green-blue values). A recent development is the hyperspectral camera that can acquire a full spectrum for each pixel. This recent technology was not introduced in the clinic at the time the research for this thesis was executed it will not be addressed here.

In this thesis, three optical imaging modalities will be discussed: near infra red fluorescence imaging (NIRF), photoacoustic imaging (PAI) and diffuse reflectance spectroscopy (DRS). These techniques were selected based on the stage of research: all three have been

used in surgery in a research setting but did not reach broad clinical acceptance, yet. Other imaging techniques were left out the scope of this thesis because either the imaged area is extremely small compared to the surgical field or the imaging takes more time than tolerable in surgical procedures. Examples are confocal microscopy[12], two-photon microscopy[12] and Optical Coherence Tomography (OCT)[13]. Raman spectroscopy[14], a technique based on the detection of an energy shift in photons due to inelastic scattering, is also left out of scope because at the start of this work it was not available as a modality for clinical research.

Near-infra red fluorescence optical imaging

An intra-operative optical imaging system produces an image of the surgical field and may add information by enhancing contrast or by visualizing characteristics invisible to the human eye. Cameras can be used in open surgery or during laparoscopy, but, in contrast to X-ray or MRI, require a clear view to the surface investigated. To enhance the optical contrast, optical contrast agents may be used, either conventional or targeted. Targeted contrast agents are engineered by molecular techniques to accumulate on a specific (target) tissue type. Other non-targeted contrast agents can visualize metabolism, like Fludeoxyglucose (FDG) in positron emission tomography (PET) imaging or anatomy, for example vascular contrast agents. In fluorescence imaging, the information is typically presented as an overlay image, ideally in real-time. In near-infrared fluorescence imaging (NIRF) the tissue is illuminated with (laser) light to excite a targeted fluorescent molecule (figure 1.02, adopted from chapter 2). After excitation, this molecule emits a photon with a longer wavelength; a different color. A highly sensitive optical system records only the fluorescent signal. Due to the relatively low absorption and scattering in the 650-900 nm 'diagnostic window', the system can (in optimal cases) identify fluorescence up to a centimeter deep. Auto-fluorescence (fluorescence by body molecules) in the near-infrared region is rare, enabling high sensitivity for NIRF imaging.
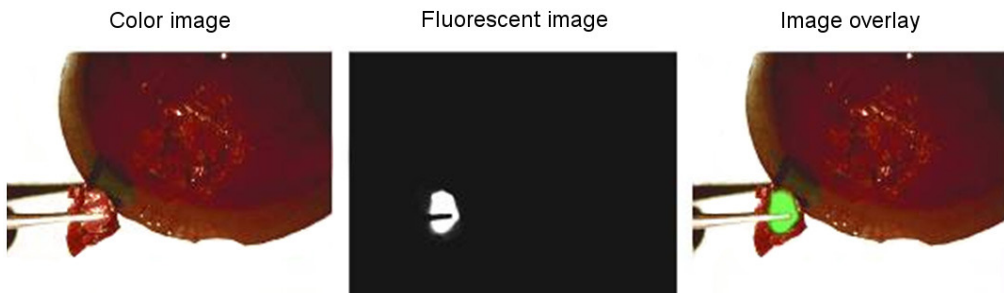
| Color image | Fluorescent image | Image overlay |

Figure 1.02. Overlay image from a breast phantom with a fluorescent inclusion, acquired with a multispectral camera (adopted from chapter 2).

Two mayor disadvantages accompany intra-operative fluorescence imaging. First, the technique is intended to visualize a specific fluorophore, all other structures, including vital ones, are regarded as background. Although simultaneous use of a combination of differently targeted probes is suggested[15] and has even performed preclinically[16], the number of distinct fluorescent probes is physically limited. This limitation is based on the spectral difference that two probes must exhibit to differ spectroscopically. Furthermore, the need to discriminate between fluorescent agents raises the technical requirements on the camera system. A second intrinsic drawback is lack of information about the depth of the origin of the signal in the tissue. In small animals this can be overcome, in some extent, by optical tomography. However, the glow effect caused by scattering of light remains a problem. This glow results in a similar image for either a weak but larger diffuse source at the surface or a strong focal source at depth (figure 1.03, adapted from chapter 2). The difference, however, is crucial in oncologic surgery as a larger superficial source requires a totally different approach than a focal source at depth. In addition to scattering, optical absorption limits the penetration depth. In fig 1.03, the hot spot of the inclusion not only blurs out, but weakens with increasing depth, due to scattering as well as absorption.
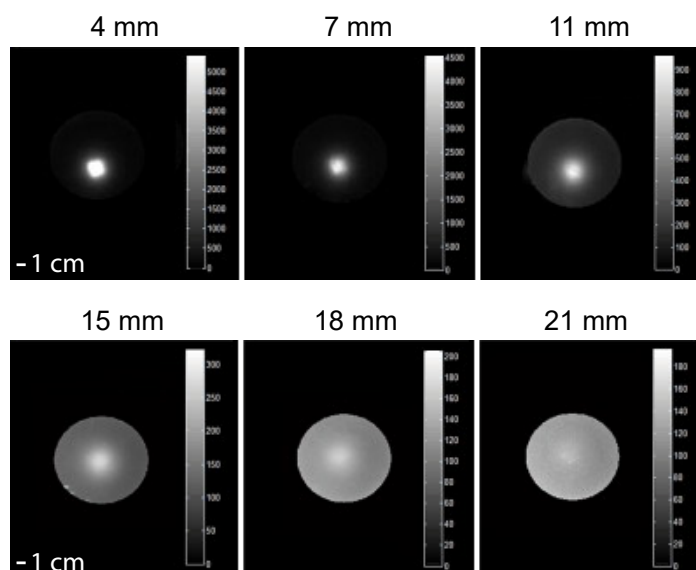
Figure 1.03. Phantoms with scattering and absorption coefficients matched to breast tissue, with a 5 mm cubic fluorescent inclusion at different depths. The phantom is cast in a round glass beaker, the edge of the phantom and surrounding is cropped (set to black). The image shows that most of the spatial information is lost when the fluorescent inclusion is positioned at some depth. As a consequence, scattering hampers the discrimination between a weak superficial source and a strong focal source at depth.

Sensing optical absorption in 3D

With photoacoustic imaging (PAI), two disadvantages of NIRF (no identification of the vital surrounding structures and the lack of information about the depth of the signal) can be overcome. PAI images optical absorption in 3 dimensions and can therefore discriminate

between superficial and deeper lying sources[17]. The technique uses pulsed light and is based on tissue specific absorption. The absorption of pulsed light results in a pulsed thermal expansion. In case of a very short pulse (~1 nsec), the rapid expansion causes a sound wave that can be detected using an ultrasound detector (Figure 1.04). The location of the absorbing structure can be determined analog to conventional sonography. As in fluorescent imaging, the result is an overview image with the contrast highlighted. However, there are two important differences. First, instead of a fluorescent emission, the tissue specific chromophores emit ultrasound waves. Sound waves are not influenced by optical scattering and can be traced to the source in 3D. As ultrasound waves are less affected by scattering compared to light, PAI localizes deeper lying sources more precise compared to NIRF imaging. Second, PAI can discriminate between different optical absorbers when sequentially illuminating the tissue with a variety of wavelengths (multispectral PAI). Doing so, simultaneous visualization of multiple body chromophores as well as optical contrast agents is possible. Multispectral PAI should be able to visualize and recognize both tumor and vital structures like blood vessels in 3D images, with minimal distortion due to optical scattering. Nevertheless, photoacoustic imaging is a complex technique investigated by few research groups. PAI is time-consuming especially in multispectral mode and requires acoustic tissue contact during imaging.

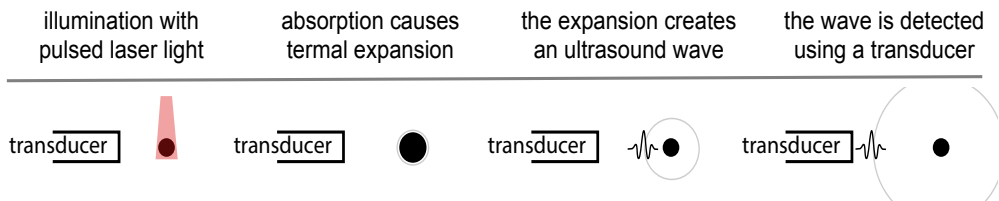| illumination with pulsed laser light | absorption causes termal expansion | the expansion creates an ultrasound wave | the wave is detected using a transducer |

Figure 1.04. Schematic representation of photoacoustic imaging; an ultrasound wave is elicited by thermal expansion after absorption of pulsed laser light. In the visualized setup, the laser light source is separated from the ultrasound array.

Optical spectroscopy

In optical spectroscopy, tissue discrimination is usually based on intrinsic spectral differences, without the use of contrast agents. In general, a continuous spectrum is recorded from which (multiple) discriminating parameters are derived. Within optical spectroscopy, several different techniques can be distinguished such as Diffuse Reflectance Spectroscopy (DRS) and Fluorescence Spectroscopy (FS). With DRS, tissue is illuminated with white light and the reflectance is collected, often using a fiber optic cable containing fibers of 50-200 µm in diameter. When the light travels from the emission fiber to the collection fiber, the photons interact with the tissue. The spectrum recorded from the collection fiber differs from the spectrum of the light source as the light is scattered and partially absorbed by the tissue.

Both scattering and absorption are tissue specific and depend on the wavelength of the

incident light[18]. In this way, different chromophores in the tissue such as hemoglobin (oxygenated and deoxygenated), b-carotene, water, lipids, and collagen can be recognized and quantified based on a characteristic spectrum. Fluorescence spectroscopy (FS) is the recording of the fluorescence signal after (laser) excitation. FS adds the possibility to determine intrinsic fluorophores in the measured tissue, such as collagen, elastin, FAD, NADH, and porphyrins[18]. Collagen and elastin are structural proteins and are associated with tissue structure, whereas NADH and FAD levels are indicative for cellular energy metabolism. DRS-FS has been shown to identify tumors of various origins[19-22]. DRS is a point measurement technique and therefore does not provide an (overview) image. Furthermore, it requires contact to the tissue of interest, which in some situations can be a limitation.

Surgical application

The optical techniques described have different technical requirements when applied in the clinic. NIRF imaging needs a clear, non scattering medium like air or water between the tissue and the camera whereas PAI and DRS require tissue contact. Also, the space required for the setup differs. PAI needs the most space with a laser source and ultrasound array. In theory the technology could be scaled down to integration into laparoscopic instruments, but a laparoscopic instrument capable of photoacoustic imaging has not been presented so far. Laparoscopic NIRF cameras are commercially available[23]. NIRF during surgery can therefore be done either in open surgery or during laparoscopic procedures. For application of DRS during surgery the small diameter of the optical fibers in DRS make incorporation into all kind of devices possible. Spliethoff et al. described a biopsy tool with optical fibers for DRS fully incorporated[24]. Rathmell et al. presented a needle for epidural anesthesia equipped with optical fibers[25]. Eventually, DRS could be used during the surgical procedure by incorporating optical fibers into a smart surgical instrument.

Clinical device

Intra-operative cameras in clinical research are often already used as intended for clinical application: Placed in the perspective of the surgeon and delivering an overview image. For photoacoustic imaging, the first clinical application will probably be integrated into a hand held ultrasound probe, as used in chapter 3. However, for DRS the clinical application is less clear. Although the technique is often presented as a needle or stylus, smart optical devices for specific clinical applications were presented. Spliethoff et al. used smart optical biopsy tool for transthoracal lung biopsies, with optical fibers fully incorporated into a functional biopsy tool[24]. Rathmell et al. presented a functional needle for epidural anesthesia equipped with optical fibers[25].

The small dimensions of the optical fibers in DRS make incorporation into existing clinical devices possible; as demonstrated by the two examples above. However, clinical

application of optical spectroscopy should not be limited to spicing up existing devices. In chapter eight, we explore the dimensional requirements of a bronchoscopic biopsy tool.

Goal of this thesis

For optimal results in surgical treatment, accurate localization and orientation of both tumor and vital surrounding tissue is crucial to achieve radical resection while conserving maximum function and physical appearance. The goal of this thesis is to evaluate three different techniques for intraoperative imaging on their ability to identify both tumor and surrounding vital structures, the dependency on other systems for overview and orientation, and the constraints for integration of these techniques in the clinical work-flow.

Outline of this thesis

Chapter two describes the use of an intraoperative fluorescence camera in breast cancer phantoms. The technique provides the surgeon with an image overlay of the fluorescent contrast agent in phantoms mimicking absorption and scattering properties of human breast tissue. In this chapter the penetration depth or depth of view of NIRF imaging is assessed by imaging a contrast rich inclusion in a tissue mimicking phantom at multiple depths. The relation between the depth of the signal and the recorded pattern at the surface is discussed. The integration into surgical practice is evaluated by performing lumpectomy in breast cancer phantoms containing fluorescence inclusions.

In chapter three the possibilities for photoacoustic imaging in surgery are investigated. In PAI, ultrasound waves are detected that were caused by optical absorption in the tissue. Therefore PAI does not suffer from optical scattering as in NIRF imaging. Furthermore, it provides 3D imaging and thus also providing information about the depth of the tissue of interest. The experimental work is focused on diagnosing positive lymph nodes in melanoma patients. Tumor positive lymph nodes contain both tumor deposits as well as blood vessel. This makes it a suitable test case to detect both tumor and vital surrounding structures. The spectral identification of both tumor and blood vessels is demonstrated in phantoms and human lymph nodes ex vivo. Furthermore, the penetration depth of the technique is assessed.

In oncologic colorectal surgery, tumor is often in close relation to vital structures. The close relation of peripheral nerves with the surgical field may result in nerve damage, leading to bladder- and sexual dysfunction. Image guidance in colorectal surgery should preferably identify malignancy and healthy surrounding tissue including peripheral nerves. Chapter four describes the identification of colorectal tumors using diffuse reflection spectroscopy, as optical technique able to identify both tumor and vital surrounding structures. In an ex vivo model (resection specimen), tissue from colorectal cancer is distinguished from multiple healthy surrounding tissues.

Chapter five and six describe the use of DRS for the identification of peripheral nerves

in human subjects during surgery. Peripheral nerves are often part of the vital structures surrounding a tumor. Chapter five describes the identification of larger nerves (femoral or sciatic nerve) as a proof of principle, chapter six is committed to the detection of smaller peripheral nerves (the greater auricular nerve, the accessory nerve or the facial nerve) by DRS. In chapter seven, optical differences between human in vivo and alternative models for optimization and validation of optical techniques are evaluated. To move the technique from a strictly controlled experimental setting into a mature clinically applied device is a long process that will require multiple optimization and validation cycles. Not all these cycles need necessarily to be executed in humans in vivo. For example, for extensive measurements either an ex vivo post mortem setup or an animal model may be more practical. However, DRS is subject to the morphological composition and biochemical make-up of tissue. Both these properties will change post mortem and may differ between human and animal. In chapter seven we compared macroscopy, histology and DRS spectra between human in vivo and alternative models for nerve and surrounding tissue. The results contribute to decision making in model selection for future optimization and validation cycles.

In chapter eight, a possible application of optical tissue identification is further elaborated. The small size of the optical fibers in DRS supports the development of innovative tools. The bronchial tree is an anatomical location where a smaller diagnostic device, such as a bronchoscopic biopsy tool, could reach more (peripheral) lesions. By the exchange of the conventional visual feedback in bronchoscopy for optical tissue identification, the size of intra-bronchiolar tools could be drastically decreased. Based on simulations of the bronchial three and analysis of patient CT scans, the relation between the size of a bronchoscopic tool and the percentage of reachable lesions is defined and we estimate the optimal size of bronchoscopic biopsy tools to reach also peripheral lung lesion for biopsy.

This thesis is concluded with a general discussion in chapter nine featuring an outlook on the use of optical tissue identification for surgical application.

References

1. Quirke P, Dixon M, Durdey P, Williams N. Local recurrence of rectal adenocarcinoma due to inadequate surgical resection: histopathological study of lateral tumor spread and surgical excision. The Lancet 1986; 328(8514):996-999.

2. Connolly JA, Shinohara K, Presti JC, Carroll PR. Local recurrence after radical prostatectomy: characteristics in size, location, and relationship to prostate-specific antigen and surgical margins. Urology 1996; 47(2):225-231.

3. Schnitt SJ, Abner A, Gelman R, Connolly JL, Recht A, Duda RB, Eberlein TJ, Mayzel K, Silver B, Harris JR. The relationship between microscopic margins of resection and the risk of local recurrence in patients with breast cancer treated with breastconserving surgery and radiation therapy. Cancer 1994; 74(6):1746-1751.

4. Thomas JM, Newton-Bishop J, A'hern R, Coombes G, Timmons M, Evans J, Cook M, Theaker J, Fallowfield M, O'neill T. Excision margins in high-risk malignant melanoma. New England Journal of Medicine 2004; 350(8):757-766.

5. Gerrand C, Wunder J, Kandel R, O'Sullivan B, Catton C, Bell R, Griffin A, Davis A. Classification of positive margins after resection of soft-tissue sarcoma of the limb predicts the risk of local recurrence. Bone & Joint Journal 2001; 83(8):1149-1155.

6. Rutt BK, Lee DH. The impact of field strength on image quality in MRI. Journal of Magnetic Resonance Imaging 1996; 6(1):57-62.

7. Becker CR, Ohnesorge BM, Schoepf UJ, Reiser MF. Current development of cardiac imaging with multidetector-row CT. European journal of radiology 2000; 36(2):97-103.

8. Haloua MH, Volders JH, Krekel NM, Cardozo AML, de Roos WK, de Widt-Levert LM, van der Veen H, Rijna H, Bergers E, Jóźwiak K. Intraoperative ultrasound guidance in breast-conserving surgery improves cosmetic outcomes and patient satisfaction: results of a multicenter randomized controlled trial (COBALT). Annals of surgical oncology 2016; 23(1):30-37.

9. Gray RJ, Pockaj BA, Garvey E, Blair S. Intraoperative Margin Management in Breast-Conserving Surgery: A Systematic Review of the Literature. Annals of surgical oncology 2017:1-10.

10. Hiramoto JS, Feldstein VA, LaBerge JM, Norton JA. Intraoperative ultrasound and preoperative localization detects all occult insulinomas. Archives of surgery 2001; 136(9):1020-1026.

11. Keereweer S, Kerrebijn JD, Van Driel PB, Xie B, Kaijzel EL, Snoeks TJ, Que I, Hutteman M, Van der Vorst JR, Mieog JSD. Optical image-guided surgery—where do we stand? Molecular Imaging and Biology 2011; 13(2):199-207.

12. Diaspro A. Confocal and two-photon microscopy: foundations, applications and advances. Confocal and Two-Photon Microscopy: Foundations, Applications and Advances, by Alberto Diaspro (Editor), pp 576 ISBN 0-471-40920-0 Wiley-VCH, November 2001 2001:576.

13. Huang D, Swanson EA, Lin CP, Schuman JS, Stinson WG, Chang W, Hee MR, Flotte T, Gregory K, Puliafito CA. Optical coherence tomography. Science (New York, NY) 1991; 254(5035):1178.

14. Colthup N. Introduction to infrared and Raman spectroscopy: Elsevier. 2012.

15. Nguyen QT, Tsien RY. Fluorescence-guided surgery with live molecular navigation [mdash] a new cutting edge. Nature reviews cancer 2013; 13(9):653-662.

16. Fernández A, Vendrell M. Smart fluorescent probes for imaging macrophage activity. Chemical Society Reviews 2016; 45(5):1182-1196.

17. Xu M, Wang LV. Photoacoustic imaging in biomedicine. Review of scientific instruments 2006; 77(4):041101.

18. Cheong W-F, Prahl SA, Welch AJ. A review of the optical properties of biological tissues. IEEE journal of quantum electronics 1990; 26(12):2166-2185.

19. Bard MP, Amelink A, Skurichina M, Noordhoek Hegt V, Duin RP, Sterenborg HJ, Hoogsteden HC, Aerts JG. Optical spectroscopy for the classification of malignant lesions of the bronchial tree. Chest 2006; 129(4):995-1001.

20. Zhou C, Choe R, Shah N, Durduran T, Yu G, Durkin A, Hsiang D, Mehta R, Butler J, Cerussi A. Diffuse optical monitoring of blood flow and oxygenation in human

breast cancer during early stages of neoadjuvant chemotherapy. J Biomed Opt 2007; 12(5):051903-051903-051911.

21. Wang H-W, Jiang J-K, Lin C-H, Lin J-K, Huang G-J, Yu J-S. Diffuse reflectance spectroscopy detects increased hemoglobin concentration and decreased oxygenation during colon carcinogenesis from normal to malignant tumors. Optics Express 2009; 17(4):2805-2817.

22. Brown JQ, Bydlon TM, Richards LM, Yu B, Kennedy SA, Geradts J, Wilke LG, Junker MK, Gallagher J, Barry WT. Optical assesssment of tumor resection margins in the breast. Selected Topics in Quantum Electronics, IEEE Journal of 2010; 16(3):530-544.

23. van den Bos J, Schols RM, Luyer MD, van Dam RM, Vahrmeijer AL, Meijerink WJ, Gobardhan PD, van Dam GM, Bouvy ND, Stassen LP. Near-infrared fluorescence cholangiography assisted laparoscopic cholecystectomy versus conventional laparoscopic cholecystectomy (FALCON trial): study protocol for a multicentre randomised controlled trial. BMJ open 2016; 6(8):e011668.

24. Spliethoff JW, Prevoo W, Meier MA, de Jong J, Klomp HM, Evers DJ, Sterenborg HJ, Lucassen GW, Hendriks BH, Ruers TJ. Real-time in vivo tissue characterization with diffuse reflectance spectroscopy during transthoracic lung biopsy: a clinical feasibility study. Clinical cancer research 2016; 22(2):357-365.

25. Rathmell JP, Desjardins AE, van der Voort M, Hendriks BH, Nachabe R, Roggeveen S, Babic D, Söderman M, Brynolf M, Holmström B. Identification of the Epidural Space with Optical SpectroscopyAnIn Vivo Swine Study. The Journal of the American Society of Anesthesiologists 2010; 113(6):1406-1418.
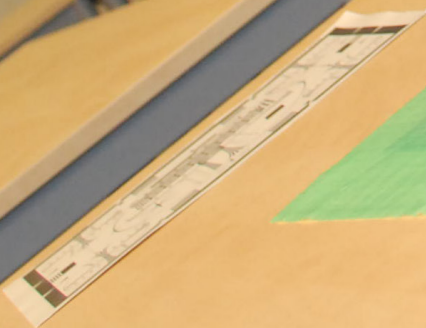
Near-infrared fluorescence (NIRF) imaging in breast-conserving surgery: Assessing intraoperative techniques in tissue-simulating breast phantoms

Breast-conserving surgery (BCS) results in tumor-positive surgical margins in up to 40% of the patients. Therefore, new imaging techniques are needed that support the surgeon with real-time feedback on tumor location and margin status. In this study, the potential of near-infrared fluorescence (NIRF) imaging in BCS for pre- and intraoperative tumor localization, margin status assessment and detection of residual disease was assessed in tissue-simulating breast phantoms.

Breast-shaped phantoms were produced with optical properties that closely match those of normal breast tissue. Fluorescent tumor-like inclusions containing indocyanine green (ICG) were positioned at predefined locations in the phantoms to allow for simulation of (i) preoperative tumor localization, (ii) real-time NIRF-guided tumor resection, and (iii) intraoperative margin assessment. Optical imaging was performed using a custom-made clinical prototype NIRF intraoperative camera.

Tumor-like inclusions in breast phantoms could be detected up to a depth of 21 mm using a NIRF intraoperative camera system. Real-time NIRF-guided resection of tumor-like inclusions proved feasible. Moreover, intraoperative NIRF imaging reliably detected residual disease in case of inadequate resection.

We evaluated the potential of NIRF imaging applications for BCS. The clinical setting was simulated by exploiting tissue-like breast phantoms with fluorescent tumor-like agarose inclusions. From this evaluation, we conclude that intraoperative NIRF imaging is feasible and may improve BCS by providing the surgeon with imaging information on tumor location, margin status, and presence of residual disease in real-time. Clinical studies are needed to further validate these results.

R.G. Pleijhuis, G.C. Langhout, W. Helfrich, G. Themelis, A. Sarantopoulos, L.M.A. Crane,
N.J. Harlaar, J.S. de Jong, V. Ntziachristos, G.M. van Dam

Introduction

Breast cancer is the most frequent malignancy in women worldwide with an estimated 1.4 million new cases in 2010[1]. Breast-conserving therapy (BCT), consisting of breast-conserving surgery (BCS) followed by radiation therapy, has become the standard treatment for T1–T2 breast tumors and is generally regarded as sufficient for this subset of patients[2]. Unfortunately, a majority of studies on the surgical margin status after BCS have shown that positive margins are detected in 20–40 % of patients, necessitating additional surgical intervention or radiotherapy[3]. Two major points for improving outcome after BCS involve (i) a more reliable intraoperative tumor localization and (ii) improved real-time feedback on the presence of possible residual disease during or after excision of the tumor[4]. Intraoperative application of an optical imaging technique known as near-infrared fluorescence (NIRF) imaging may improve the clinical outcome of BCS[3,5].

Near-infrared fluorescence imaging

In recent years, significant progress has been made in the development of optical imaging systems and fluorophores for clinical applications[6,7]. Several animal[5,8-10] and clinical[11-15] studies have shown the potential clinical use of NIRF imaging to improve the therapeutic outcome of surgery. Compared to light in the visible spectral range (400–650 nm), application of near-infrared (NIR) light minimizes absorption by physiologically abundant molecules such as hemoglobin and lipids, which increases penetration depth[16,17]. Additionally, autofluorescence (the intrinsic fluorescence signal present in all living cells due to various normal metabolites and tissue constituents) is strongly reduced in the NIR spectral range. Taken together, these aspects of NIR light make it particularly suitable for use in intraoperative optical imaging applications. However, clinical application of NIRF imaging in BCS is currently limited to the non-specific intraoperative detection of the sentinel lymph node[11,12,14,18-20].

Tumor-targeted near-infrared fluorophores

With the introduction of clinical grade tumor-targeted NIR fluorophores, NIRF imaging may be extended towards the intraoperative detection of the primary tumor[10]. Several target molecules have been identified for breast cancer that may be of value for such an approach, including Her2/neu receptor[9,21,22], vascular endothelial growth factor (VEGF) receptor[23,24], endothelial growth factor (EGF) receptor[25] and folate receptor-α[26].

In tumor-targeted NIRF imaging, a tumor-targeted NIR fluorophore is administered several hours or days prior to the imaging procedure. Subsequently, an external laser is used to irradiate the breast with light in the NIR spectral range (650–900 nm)[17]. Upon excitation, the fluorophore will release photons of a higher NIR wavelength. Because NIR light is invisible to the naked eye, a dedicated optical imaging system is necessary to capture the NIR signal from the surgical field and digitally convert it to a visible image. Recently, we

and our co-workers developed a multispectral NIRF intraoperative camera system that is suitable for intraoperative use with NIR fluorophores[27].

Simulation of NIRF-guided breast-conserving surgery

In the current preclinical study, we evaluated intraoperative NIRF imaging applications in a simulated clinical setting as a step-up toward NIRF-guided BCS. To this end, we used tissue-simulating gelatin-based breast phantoms that mimic the optical properties of normal breast tissue[28,29]. Tumor-like fluorescent inclusions of different size and shape were positioned at predefined sites in the phantoms, allowing for simulation of (i) preoperative tumor localization, (ii) real-time NIRF-guided tumor resection and (iii) intraoperative macroscopic margin assessment. The tumor-like inclusions contain the non-specific NIR fluorophore indocyanine green (ICG), to simulate for the use of tumor-targeted near-infrared fluorophores in BCS. Currently, ICG (absorption and emission maximum at ~780 nm and ~820 nm, respectively) is one of the few FDA-approved NIR fluorophores available for clinical use[9]. Sevick-Muraca et al. have previously shown the feasibility of NIRF imaging following microdose administration of ICG[12]. Although ICG in itself is non-specific, their findings suggest that comparable microdose concentrations can be used to label cancer cells with tumor-targeted NIR fluorophores for intraoperative NIRF imaging. Importantly, new fluorophores in the NIR spectral range are currently being developed, e.g. IRDye[®] 800CW, with properties more promising for intraoperative use compared to ICG[25].

Material and methods

Assessment of ICG fluorescence self-quenching in agarose

Because increasing concentrations of ICG may not correspond to an increased fluorescence signal due to self-quenching of ICG, different concentrations of ICG in agarose were evaluated for fluorescence activity[29,30]. Briefly, an ICG stock solution was serially diluted in 10 ml sterile water (ranging from 0.5 uM to 350 uM ICG), after which 2 % agarose was added. The mixture was then heated to 70 °C and stirred until the agarose was completely dissolved. After solidification of the agarose mixture for 15 min at 4 °C, NIRF epi-illumination imaging was performed to determine maximum photon counts/sec (settings: exposure time: 1000 ms, excitation: 780 nm, emission: 820 nm).

Assessment maximal penetration depth of ICG fluorescence

In order to determine the maximal penetration depth of the NIRF signal, a cubic fluorescent inclusion of 5 × 5 × 5 mm containing 14 µM ICG was positioned in phantom tissue at a depth of 30 mm. Subsequently, the surgeon excised 3–4 mm layers of phantom tissue towards

the inclusion (remaining depths were 27, 24, 21, 18, 15, 11, 7, and 4 mm, respectively). At all depths, NIRF epi-illumination imaging was performed with the intraoperative NIRF camera system (exposure time: 3000–60000 ms, excitation 780 nm, emission 820 nm, binning: small-medium). Maximum photon counts per second exposure time were calculated as well as the full width at half maximum (FWHM) of the fluorescence signal. The FWHM is a measure for scattering and indicates the diameter of the fluorescence signal when the intensity of the signal is reduced to half the maximum. Scattering both contributes to signal loss and loss in resolution. The FWHM indicates the minimal distance between two distinct sources to be recognized as separate.

Tissue-simulating breast phantoms

Composition of the tissue-simulating gelatin-based breast phantoms was aimed at obtaining uniform optical properties that closely match the optical characteristics of normal breast tissue, as described in detail before[29]. Additionally, the breast phantoms mimic the elastic properties of human tissue[31].

Briefly, 10 % gelatin 250 (Natural Spices, Watergang, the Netherlands) was dissolved in 1 l TBS (50 mmol Tris–HCl, 150 mmol NaCl, pH 7.4). To remove molecular oxygen and prevent microbial infection, 15 mmol NaN_3 (Merck, Darmstadt, Germany) was added. The gelatin slurry was completely dissolved by heating to 50 °C and subsequently cooled down to 35 °C and maintained at this temperature. Under constant stirring, 170 µmol hemoglobin (Sigma–Aldrich, Zwijndrecht, The Netherlands) and 1 % Intralipid® 20 % (Sigma–Aldrich) were added. Next, the gelatin mixture was poured in a custom-made pre-chilled breast-shaped mold (end volume: 500 ml) to a level that corresponded to the predefined depth of the agarose inclusion. After solidification for 30 min at 4 °C, a tumor-like NIR fluorescent agarose inclusion was positioned on the surface and temporarily fixed with a small needle. Next, the remaining of the warmed gelatin mixture was added to fill up the remaining mold volume, allowing for adherence of both layers. The phantom was then stored in the dark to solidify for another 30 min at 4 °C, after which it was gently removed from its mold.

In total, 4 breast phantoms were constructed with tumor-like NIR fluorescent agarose inclusions of different size and shape (Figure 2.01A) positioned at predefined depths. Imaging of the phantoms was performed directly after production of all 4 phantoms.

Breast phantom #1 contained 2 similar-sized (Ø1.0 cm) sphere-shaped agarose inclusions at different depths (2.0 and 4.0 cm). Phantom #2 contained 2 sphere-shaped inclusions at the same depth (1.5 cm), differing in size (Ø0.5 cm and Ø2.0 cm). Phantom #3 contained 1 sphere-shaped (Ø1.0 cm) and 1 prolate sphere-shaped (Ø1.0 cm) agarose inclusion at the same depth (1.5 cm). Finally, phantom #4 contained 2 irregular shaped agarose inclusions of similar size (Ø1.5 cm) at different depths (1.5 and 3.0 cm).

Tumor-like NIR fluorescent agarose inclusions

For tumor-like NIR fluorescent agarose inclusions, 2 % agarose (Hispanagar, Burgos, Spain) was used instead of 10 % gelatin. Agarose has a higher melting point which prevents the inclusions from dissolving and leaking ICG (see below) during and after the positioning procedure in the gelatin phantom. In short, a 2 % (W/V) agarose slurry was heated to 70 °C and stirred until the agarose was completely dissolved. Subsequently, ICG (ICG-PULSION®; Pulsion Medical Systems, Munich, Germany) was dissolved to a final concentration of 14 µM. Finally, in order to resemble the optical appearance of the surrounding breast phantom tissue, 170 µM hemoglobin, 15 mM NaN_3 and 1 % Intralipid® 20% were added to the tumor-like fluorescent inclusions.

Tumor-like fluorescent inclusions of different size (range: 0.5 cm–2.0 cm) and shape (prolate sphere, sphere and irregular shape, Fig. 2.01A) were produced. The inclusions were integrated in the breast phantoms as indicated and chilled in the dark for 30 min at 4 °C. Imaging of each individual breast phantom was performed within 6 h.

Near-infrared fluorescence imaging system

A custom-made NIRF camera system was developed in collaboration with SurgOptix Inc (SurgOptix Inc, Redwood Shores, CA, USA) for real-time intraoperative imaging. The system implements a correction scheme that improves the accuracy of epi-illumination fluorescence images for light intensity variations in tissue. Implementation is based on the use of three cameras operating in parallel. The camera is mounted on a five degrees of freedom bracket. Additionally, a sixth degree (rotation) can be performed digitally. The camera allows for simultaneous acquisition of color videos and normalized fluorescence images in real-time, yielding a lateral resolution up to 66.58 µm and a variable field of view (FOV) of 13.5 W × 11 H to 115 W × 95 H (mm). A description in full detail is provided by Themelis et al[27]. The invisible NIRF imaging signal was digitally converted into a pseudo-color and superposed on a color video image of the operating field, allowing for real-time, intraoperative anatomical positioning of the fluorescence signal.

Simulation of intraoperative NIRF imaging

Breast phantoms with tumor-like NIR fluorescent agarose inclusions were used to simulate and evaluate the potential of NIRF imaging applications in BCS (Fig. 2.01 and Fig. 2.03). In all phantoms, the location of the tumor-like fluorescent inclusions was assessed preoperatively with non-invasive NIRF imaging. In phantoms #1 and #2, the tumor-like fluorescent inclusions were subsequently excised using conventional surgical equipment, guided solely by visual inspection, tactile information, and preoperatively obtained NIRF imaging data. The surgeon was asked to indicate when he believed a complete excision of the tumor was reached. Subsequently, the NIRF camera system was applied to assess the feasibility of NIRF-guided macroscopic margin assessment of the surgical cavity and

A Inclusions

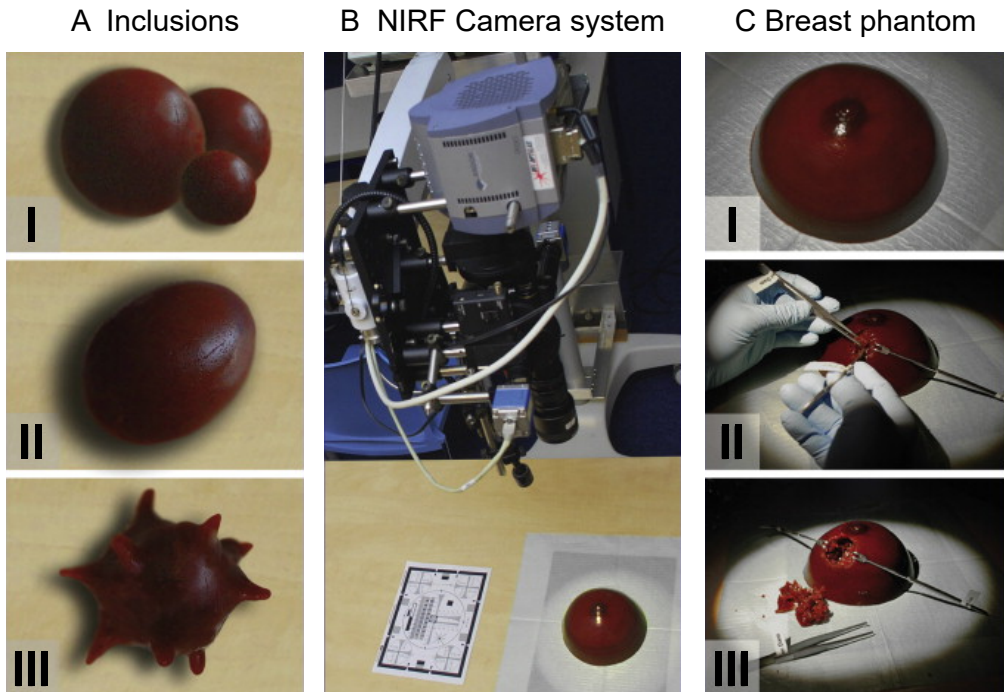## B NIRF Camera system

C Breast phantom

Figure 2.01. | Fluorescent tumor-like agarose inclusions differing in size and shape (AI–III) were integrated in breast-shaped phantoms (CI) prior to surgery. Preoperatively, the location of the tumor-like inclusion was assessed non-invasively using a NIRF camera system (B). Intraoperatively, the inclusion was excised under real-time NIRF guidance or guided solely by visual and tactile information (CII). At the end of the surgical procedure, the NIRF camera system was applied to inspect for residual disease and evaluate the extend of surgery (CIII).

excised tissue fragments. In case of an incomplete excision, the surgeon was asked to perform a re-excision under real-time NIRF guidance.

In phantoms #3 and #4, the tumor-like fluorescent inclusions were localized and excised under real-time NIRF guidance. While approaching the tumor-like fluorescent inclusions, the surgeon was supported with both visible and audible information. In short, the detected fluorescence signal was depicted on a TFT-screen and was made quantitatively audible using a digitally generated sound-pitch. In this approach, an increase in sound-pitch represents an increase in fluorescence signal indicating the approximation of a tumor-like fluorescent inclusion.

Results

ICG fluorescence self-quenching in agarose

To determine the optimal ICG concentration in agarose, a serial range of increasing ICG concentrations was analyzed for fluorescence characteristics. The optimal fluorescence signal was observed at a concentration of approximately 10 µM ICG (Fig. 2.04). These results are comparable to self-quenching characteristics of ICG as previously determined in gelatin[29].

Maximal penetration depth of ICG fluorescence

The maximal tissue penetration depth of a detectable fluorescent ICG inclusion was reached at a depth of 21 mm (Fig. 2.02C).
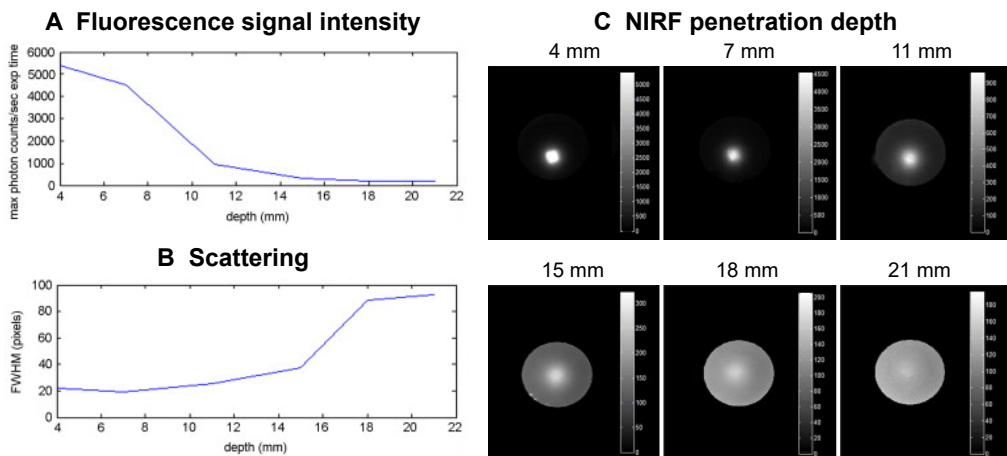

Figure 2.02. | Fluorescence signal intensity related to depth-location in tissue-like phantoms is shown for fluorescent agarose inclusions placed at varying depths in phantom tissue (A). Depth (mm) of the inclusion and maximum photon counts per second exposure time are depicted on the horizontal and vertical axis, respectively. Moreover, scattering of the fluorescence signal is shown (B), with depth (mm) and full width at half maximum (pixels) on the horizontal and vertical axis, respectively. For determination of the NIRF signal penetration depth with the NIRF intraoperative camera system (C), the surgeon repeatedly excised 3–4 mm tissue layers, working his way towards a fluorescent inclusion placed at 30 mm depth in breast phantom tissue. At 30, 27 and 24 mm inclusion depth, no NIRF signal could be detected (not shown). Images were corrected (normalized) for an exposure time of 1000 ms.time NIRF guidance or guided solely by visual and tactile information (CII). At the end of the surgical procedure, the NIRF camera system was applied to inspect for residual disease and evaluate the extend of surgery (CIII).

Simulation of intraoperative NIRF imaging

Preoperative NIRF-guided localization of tumor-like fluorescent agarose inclusions was performed in 4 different breast phantoms. The various tumor-like inclusions positioned at a depth of ≤2.0 cm were detectable with the NIRF camera system (Fig. 2.03A-I). Tumor-like inclusions positioned at depths of 3.0 and 4.0 cm could not be detected preoperatively.

Tumor-like inclusions in phantom #1 and #2 were excised using conventional techniques for tumor localization. In phantom #1, one out of two tumor-like inclusions proved to be only partially excised, as evidenced by a remnant strong fluorescence signal in the surgical cavity detected by the NIRF camera system (Fig. 2.03C-III). In phantom #2, the excision of one out of two inclusions was found to be incomplete. In case of residual fluorescence, the surgeon could detect and excise (theranostic procedure) the remnant inclusion under real-time NIRF guidance (Figure 3C-IV and supplemental video 1). In all cases, NIRF-guided re-excision resulted in a complete excision, without the need for additional excision of large breast phantom fragments (Fig. 2.03C-V).

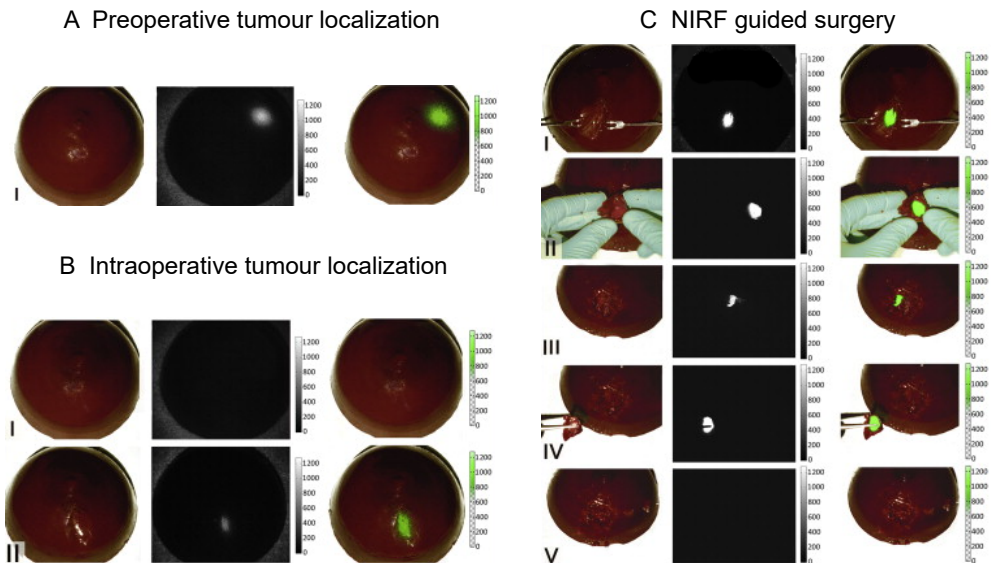# Near-Infrared Fluorescence (NIRF) imaging applications

Figure 2.03. | Overview of NIRF applications in breast-conserving surgery. In the case of relatively superficial lesions (≤2 cm), NIRF allows for preoperative localization of fluorescent tumor-like inclusions (A). Intraoperative NIRF imaging guides the surgeon towards the tumor-like agarose inclusions (B + C) and allows for intraoperative assessment of surgical margin status (CII–V) and detection of residual disease (CIII). Color bars next to the color overlay indicate a threshold at 800 counts. Pixels with values above the threshold were superposed on the color video (overlay). Exposure time was set to 150 ms for all images.

In phantoms #3 and #4, the tumor-like inclusions were located (Fig. 2.03B) and excised (Fig. 2.03C) under real-time NIRF guidance. Although the inclusion at 3.0 cm depth in phantom #4 could not be detected preoperatively (Fig 2.03B-I), it was detectable using the NIRF camera system after an incision of approximately 1 cm of superficial phantom tissue (Fig. 2.03B-II). In phantom #3, no residual tumor-like inclusion material could be detected after initial NIRF-guided excision, while the excision of one out of two irregular inclusions in phantom #4 was found to be incomplete. Again, subsequent NIRF-guided re-excision resulted in a complete excision.

During the surgical simulation procedure, the approximation of the surgeon towards tumor-like fluorescent agarose inclusions was guided by both visual information on a TFT-screen and audible sound-pitched information. The approach resulted in a clear change in the signal strength of the fluorescence image that was accompanied with an increase of the sound pitch at ~15 mm prior to excision of the tumor-like agarose inclusion. These signals assisted the surgeon in carefully advancing the margins.
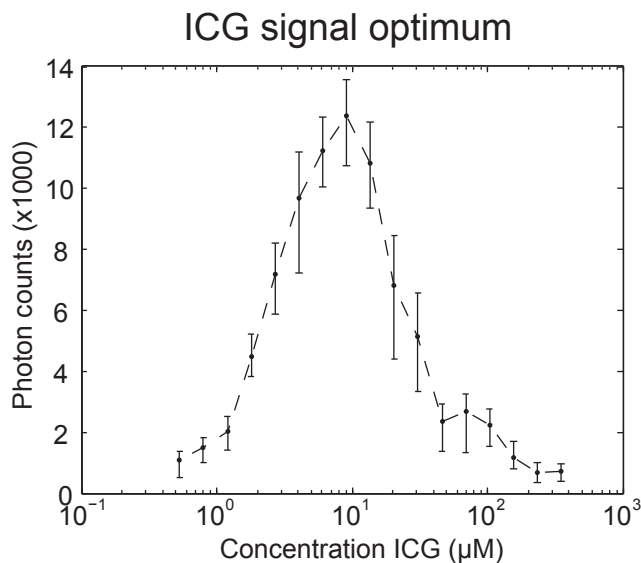
ICG signal optimum

Figure 2.04. | Optimal ICG concentration in 2% agarose was determined in breast phantom tissue. Seventeen different concentrations (each 10 ml, ranging from 0.5 µM to 350 µM) were imaged at once with the intraoperative NIRF camera system. Working distance 45 cm, field of view 160 W × 130 H (mm), exposure time: 1000 ms.

Discussion

Tissue-like phantoms and tumor-like inclusions

The composition of the breast phantoms was based on data published by De Grand et al., who developed and validated phantoms to mimic the basic optical characteristics (absorption and scattering coefficients) of breast tissue[29]. The absorption of photons by both cellular organelles and blood was simulated by hemoglobin, which gives the phantoms a deep red color[32,33]. Additionally, Intralipid® was added to mimic scattering properties of breast tissue[28].

In order to resemble the clinical situation as close as possible, tumor-like fluorescent agarose inclusions were incorporated in the breast phantoms. The agarose-based inclusions simulate the firm-elastic consistency of tumor tissue and allow for surgical margin status assessment, both intraoperatively (NIRF-guided surgery) and ex vivo (NIRF-guided macroscopic margin assessment). The relatively low concentration of ICG used in this study resembles the potential application of microdose tumor-targeted fluorophores (ranging from 1 µM to 100 µM) in BCS.

Although the phantoms used in this study are homogeneous, and therefore do not possess the complex structures that characterize mammary tissue, they do provide a tool for assessing the value of theoretical assumptions and indicate generally important features of future clinical NIRF imaging applications in BCS.

Near-infrared fluorescence imaging: strengths and drawbacks

NIRF imaging offers a promising technique for real-time NIRF-guided surgery in BCS with little interference in the standard surgical procedure or changes in the design of the operating theater. The technology is considered safe, fast, makes use of non-ionizing radiation, and has a high resolution[3,10]. However, NIRF imaging does have limitations originating from the intrinsic characteristics of light propagation through tissue, including scattering and absorbance[17].

Additionally, due to limited depth resolution and a non-linear dependence of the signal detected and the depth of the fluorescence activity, NIRF imaging by epi-illumination with our current camera system seems of limited value for preoperative localization of tumors. This applies in particular to situations where the tumor is located relatively deep (>2 cm) in fat and glandular tissue of the breast. However, since the surgeon, by definition, will bring the area of interest closer to the surface during surgery, our multispectral NIRF camera system is well-suited for intraoperative imaging applications.

NIRF imaging instruments designed for preoperative imaging, e.g. the SoftScan (ART, Advanced Research Technologies, Saint-Laurent (Quebec), Canada), show penetration depths far superior (up to 15 cm) to intraoperative imaging systems[34]. This difference in

penetration depth is due to the application of different imaging strategies which are largely incompatible with surgery, e.g. trans-illumination and the need for light-conducting liquid media.

Non-specific versus tumor-targeted fluorophores

Several possibilities exist for delivering fluorophores to the tumor. One possibility would be to inject a non-specific fluorophore (e.g. ICG) into the tumor under stereotactic or ultrasonographic guidance[35]. However, there are some significant drawbacks to this approach. First, the injection of the non-specific fluorophore into the tumor is a critical step in the procedure and has to be very accurate to minimize false-negative and false-positive results. Additionally, spillage/leakage of fluorophore within the mammary gland during the procedure will decrease accuracy of both localization of the tumor and macroscopic margin assessment. Therefore, we believe NIRF-guided surgery should ideally be combined with tumor-targeted fluorophores, which provide molecularly-specific detection of cancer cells. In these agents, the NIR fluorophore has been conjugated to a specific targeting ligand or monoclonal antibody. This allows for tumor-specific binding of the fluorophore, increasing signal-to-noise (SN) ratios and minimizing spillage of the fluorophore during the surgical procedure[3,10]. Several studies have shown the feasibility of using tumor-targeted fluorophores in vivo to image tumors intraoperatively, including the use of tumor-targeted ICG-conjugated agents[5,9,22,25,26,36,37]. However, there are some significant drawbacks, including the heterogeneity of (breast) tumors which should be solved before applying tumor-targeted NIRF imaging in the clinic. In BCS, the preoperative biopsy taken prior to surgery could provide important information on molecular targets for NIRF imaging. As this biopsy is considered standard practice, it will not require an additional invasive procedure, while offering the possibility to determine the expression of different kinds of molecular targets present on the breast cancer cells by immunohistochemical analysis. The surgeon could then look for NIRF agents suited for each individual tumor, offering a more patient-tailored approach.

Conclusion

We have preclinically assessed the applicability of NIRF imaging applications in BCS by exploiting tissue-simulating breast phantoms. NIRF-guided intraoperative tumor localization and detection of remnant disease showed feasible. Clinical studies are needed to further validate these results for use in BCS.

Conflict of interest statement

There are no potential or actual, personal, political, or financial interests by any of the authors in the material, information, or techniques described in the paper. All authors have seen and approved the manuscript and are fully conversant with its contents.

Acknowledgements

References

1. Parkin DM, Bray F, Ferlay J, Pisani P. Global cancer statistics, 2002. CA: a cancer journal for clinicians. 2005;55(2):74-108.

2. Schwartz GF, Veronesi U, Clough KB, et al. Proceedings of the consensus conference on breast conservation, April 28 to May 1, 2005, Milan, Italy. Cancer. 2006;107(2):242-250.

3. Pleijhuis RG, Graafland M, de Vries J, Bart J, de Jong JS, van Dam GM. Obtaining adequate surgical margins in breast-conserving therapy for patients with early-stage breast cancer: current modalities and future directions. Annals of surgical oncology. 2009;16(10):2717-2730.

4. Singletary S. Breast cancer surgery for the 21st century: the continuing evolution of minimally invasive treatments. Minerva chirurgica. 2006;61(4):333-352.

5. Kirsch DG, Dinulescu DM, Miller JB, et al. A spatially and temporally restricted mouse model of soft tissue sarcoma. Nature medicine. 2007;13(8):992-997.

6. Luker GD, Luker KE. Optical imaging: current applications and future directions. Journal of Nuclear Medicine. 2008;49(1):1-4.

7. Tromberg BJ, Pogue BW, Paulsen KD, Yodh AG, Boas DA, Cerussi AE. Assessing the future of diffuse optical imaging technologies for breast cancer management. Medical physics. 2008;35(6):2443-2451.

8. von Burstin J, Eser S, Seidler B, et al. Highly sensitive detection of early-stage pancreatic cancer by multimodal near-infrared molecular imaging in living mice. International journal of cancer. 2008;123(9):2138-2147.

9. Trastuzumab complexed to near-infrared fluorophore indocyanine green. Molecular Imaging and Contrast Agent Database (MICAD); 2009. https://www.ncbi.nlm.nih.gov/books/NBK23414/.

10. Keereweer S, Kerrebijn JD, Van Driel PB, et al. Optical image-guided surgery—where do we stand? Molecular Imaging and Biology. 2011;13(2):199-207.

11. Tagaya N, Yamazaki R, Nakagawa A, et al. Intraoperative identification of sentinel lymph nodes by near-infrared fluorescence imaging in patients with breast cancer. The American Journal of Surgery. 2008;195(6):850-853.

12. Sevick-Muraca EM, Sharma R, Rasmussen JC, et al. Imaging of lymph flow in breast cancer patients after microdose administration of a near-infrared fluorophore: feasibility study 1. Radiology. 2008;246(3):734-741.

13. Brandt MG, Moore CC, Jordan K. Randomized control trial of fluorescence-guided surgical excision of nonmelanotic cutaneous malignancies. Journal of Otolaryngology. 2007;36(3).

14. Ogasawara Y, Ikeda H, Takahashi M, Kawasaki K, Doihara H. Evaluation of breast lymphatic pathways with indocyanine green fluorescence imaging in patients with breast cancer. World journal of surgery. 2008;32(9):1924-1929.

15. Stummer W, Pichlmeier U, Meinel T, et al. Fluorescence-guided surgery with 5-aminolevulinic acid for resection of malignant glioma: a randomised controlled multicentre phase III trial. The lancet oncology. 2006;7(5):392-401.

16. Bremer C, Ntziachristos V, Weissleder R. Optical-based molecular imaging: contrast agents and potential medical applications. European radiology. 2003;13(2):231-243.

17. Ntziachristos V. Fluorescence molecular imaging. Annu. Rev. Biomed. Eng. 2006;8:1-33.

18. Troyan SL, Kianzad V, Gibbs-Strauss SL, et al. The FLARE™ intraoperative near-infrared fluorescence imaging system: a first-in-human clinical trial in breast cancer sentinel lymph node mapping. Annals of surgical oncology. 2009;16(10):2943-2952.

19. Kitai T, Inomoto T, Miwa M, Shikayama T. Fluorescence navigation with indocyanine green for detecting sentinel lymph nodes in breast cancer. Breast cancer. 2005;12(3):211-215.

20. Murawa D, Hirche C, Dresel S, Hünerbein M. Sentinel lymph node biopsy in breast cancer guided by indocyanine green fluorescence. British Journal of Surgery. 2009;96(11):1289-1294.

21. Gee MS, Upadhyay R, Bergquist H, et al. Human Breast Cancer Tumor Models: Molecular Imaging of Drug Susceptibility and Dosing during HER2/neu-targeted Therapy 1. Radiology. 2008;248(3):925-935.

22. Lee SB, Hassan M, Fisher R, et al. Affibody molecules for in vivo characterization of HER2-positive tumors by near-infrared imaging. Clinical Cancer Research. 2008;14(12):3840-3849.

23. Backer MV, Levashova Z, Patel V, et al. Molecular imaging of VEGF receptors in angiogenic vasculature with single-chain VEGF-based probes. Nature medicine. 2007;13(4):504-509.

24. Chen K, Li Z-B, Wang H, Cai W, Chen X. Dual-modality optical and positron emission tomography imaging of vascular endothelial growth factor receptor on tumor vasculature using quantum dots. European journal of nuclear medicine and molecular imaging. 2008;35(12):2235-2244.

25. Sampath L, Kwon S, Ke S, et al. Dual-labeled trastuzumab-based imaging agent for the detection of human epidermal growth factor receptor 2 overexpression in breast cancer. Journal of Nuclear Medicine. 2007;48(9):1501-1510.

26. Sega EI, Low PS. Tumor detection using folate receptor-targeted imaging agents. Cancer and Metastasis Reviews. 2008;27(4):655-664.

27. Themelis G, Yoo JS, Soh K-S, Schulz R, Ntziachristos V. Real-time intraoperative fluorescence imaging system using light-absorption correction. Journal of biomedical optics. 2009;14(6):064012-064012-064019.

28. Pogue BW, Patterson MS. Review of tissue simulating phantoms for optical spectroscopy, imaging and dosimetry. Journal of biomedical optics. 2006;11(4):041102-041102-041116.

29. Alec M, Lomnes SJ, Lee DS, et al. Tissue-like phantoms for near-infrared fluorescence imaging system assessment and the training of surgeons. Journal of biomedical optics. 2006;11(1):014007-014007-014010.

30. Yuan B, Chen N, Zhu Q. Emission and absorption properties of indocyanine green in Intralipid solution. Journal of biomedical optics. 2004;9(3):497-503.

31. Iizuka MN, Sherar MD, Vitkin IA. Optical phantom materials for near infrared laser photocoagulation studies. Lasers in surgery and medicine. 1999;25(2):159-169.

32. Durkin A, Jaikumar S, Richards-Kortum R. Optically dilute, absorbing, and turbid phantoms for fluorescence spectroscopy of homogeneous and inhomogeneous samples. Applied Spectroscopy. 1993;47(12):2114-2121.

33. Wagnières G, Cheng S, Zellweger M, et al. An optical phantom with tissue-like properties in the visible for use in PDT and fluorescence spectroscopy. Physics in medicine and biology. 1997;42(7):1415.

34. Intes X. Time-domain optical mammography SoftScan: Initial Results1. Academic radiology. 2005;12(8):934-947.

35. Berridge D, Mastey L, Eckstrom P, Czarnecki D. Indocyanine green dye as a tissue marker for localization of nonpalpable breast lesions. AJR. American journal of roentgenology. 1995;164(5):1299.

36. Ke S, Wen X, Gurfinkel M, et al. Near-infrared optical imaging of epidermal growth factor receptor in breast cancer xenografts. Cancer research. 2003;63(22):7870-7875.

37. Mieog JSD, Hutteman M, van der Vorst JR, et al. Image-guided tumor resection using real-time near-infrared fluorescence in a syngeneic rat model of primary breast cancer. Breast cancer research and treatment. 2011;128(3):679-689.
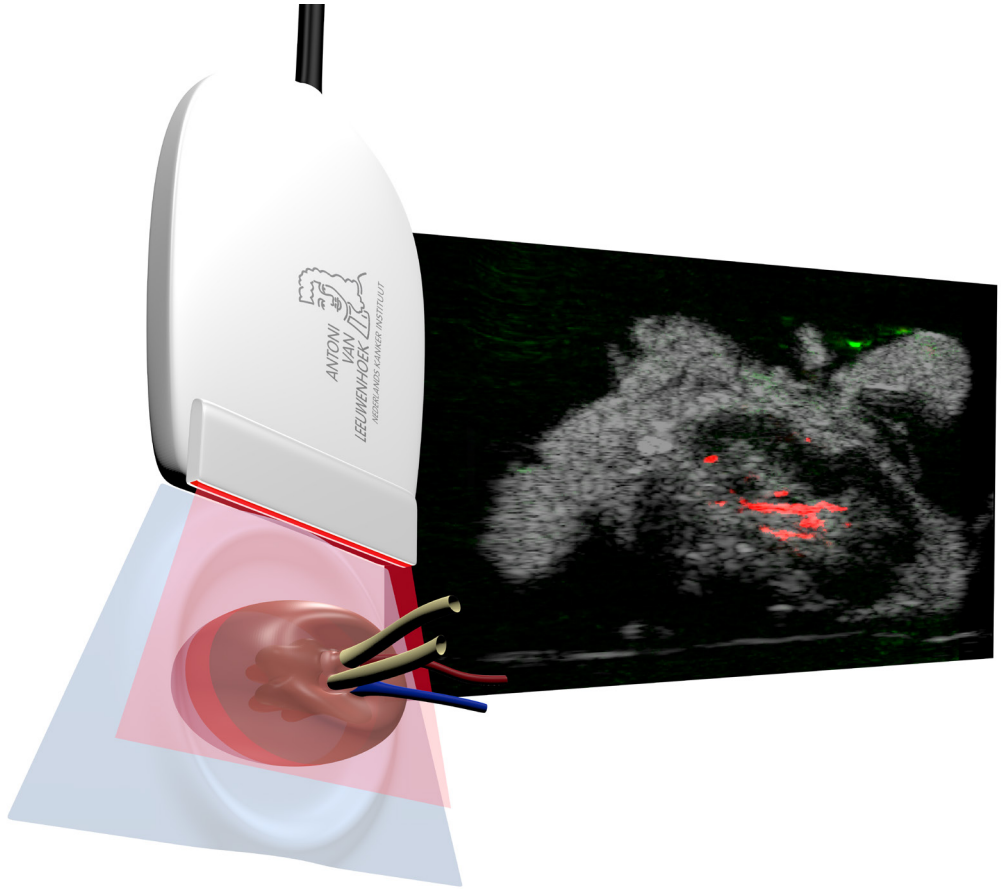
2

Detection of melanoma metastases in resected human lymph nodes by noninvasive multispectral photoacoustic imaging

Sentinel node biopsy in patients with cutaneous melanoma improves staging, provides prognostic information, and leads to an increased survival in node-positive patients. However, frozen section analysis of the sentinel node is not reliable and definitive histopathology evaluation requires days, preventing intraoperative decision-making and immediate therapy. Photoacoustic imaging can evaluate intact lymph nodes, but specificity can be hampered by other absorbers such as hemoglobin. Near infrared multispectral photoacoustic imaging is a new approach that has the potential to selectively detect melanin. The purpose of the present study is to examine the potential of multispectral photoacoustic imaging to identify melanoma metastasis in human lymph nodes.

Three metastatic and nine benign lymph nodes from eight melanoma patients were scanned ex vivo using a Vevo LAZR$^{©}$ multispectral photoacoustic imager and were spectrally analyzed per pixel. The results were compared to histopathology as gold standard.

The nodal volume could be scanned within 20 minutes. An unmixing procedure was proposed to identify melanoma metastases with multispectral photoacoustic imaging. Ultrasound overlay enabled anatomical correlation. The penetration depth of the photoacoustic signal was up to 2 cm.

Multispectral three-dimensional photoacoustic imaging allowed for selective identification of melanoma metastases in human lymph nodes.

G.C. Langhout, D.J. Grootendorst, O.E. Nieweg, M.W.M. Wouters, J.A. van der Hage, J. Jose, H. van Boven, W. Steenbergen, S. Manohar, T.J.M. Ruers

Introduction

Sentinel node biopsy in patients with melanoma improves staging and guides the subsequent management of the nodal basin. The tumor status of the sentinel node is the most important prognostic factor. Sentinel node biopsy plus complete node dissection improves ten-year survival in node-positive patients[1]. Routine histopathology evaluation requires several days, preventing intraoperative decision making and immediate lymph node dissection. Less time consuming procedures like imprint cytology and frozen section analysis are characterized by a low sensitivity. Intraoperative imprint cytology and frozen section show a sensitivity of approximately 30 % and 50 %, respectively[2,3]. Also noninvasive imaging techniques like ultrasound, computed tomography (CT), magnetic resonance imaging (MRI), and positron emission tomography (PET) lack the sensitivity to reliably detect micrometastases[4].

Photoacoustic imaging is a hybrid imaging technique, combining high-resolution ultrasound with molecular specific optical excitation. The method is based on optical absorption of pulsed light by specific tissue. The absorbed optical energy is converted to heat, which generates ultrasound waves by thermal expansion. Detection of these light induced ultrasound waves allows recovering of the location of the ultrasound sources, which are the tissue structures that absorb the light. In general, structures that absorb more light will cause a stronger ultrasound signal. The absorption of light will differ at various wavelengths, as a molecular property. A multispectral approach makes use of this property to selectively visualize metastases.

Melanin is a light absorbing substance and photoacoustic imaging has been shown to detect melanin in lymph node metastases from melanoma using a single wavelength[5,6]. Differentiation between blood and melanoma proved to be difficult because both are strong optical absorbers and therefore create a clear photoacoustic signal.

Wang used two-wavelength photoacoustic imaging to visualize thin superficial melanomas in mice using both red and infrared light[7]. Although the differentiation between melanin and blood was possible, the use of red light limits the penetration depth of this approach. For example, in this study the visualized melanoma was 0.3 mm thick and located at 0.32 mm under the skin of a nude mouse. Human lymph nodes are located at a depth of several centimeters in the human body. Near infrared light penetrates deeper into the tissue. Near infrared multispectral photoacoustic imaging may be able to selectively visualize melanin and blood at centimeters depth in intact human lymph nodes.

This study explores the potential of this new approach to identify melanoma metastasis ex vivo in human lymph nodes. A specific purpose was to correlate spectral images with known reference spectra to differentiate melanoma metastases from blood related artifacts in intact human lymph nodes. The other purpose was to investigate the value of a hand-held photoacoustic-ultrasound system capable of 3D imaging.

Materials and methods

Photoacoustic setup

The data was acquired using the Vevo LAZR© Photoacoustic Imaging System (FUJIFILM VisualSonics Inc., Toronto), a hybrid photoacousticultrasound reflection mode imager with a 21 MHz (13–24 MHz) linear array transducer. Fiber optic bundles near the surface of the transducer coupled to a 20 Hz tunable laser are able to deliver 20 mJ/cm^2 in the wavelength range of 680–970 nm. For three-dimensional image acquisition, the transducer was automatically moved over the lymph node by a stepping motor with a step size of 0.2 mm. Both ultrasound and photoacoustic images were exported as 16 bit greyscale images to MATLAB (version 7.14; Mathworks, Natick, MA,USA) for image processing.

Phantom

In order to verify whether multispectral photoacoustic imaging is able to differentiate the chromophores blood from melanin, a phantom was developed. This was made of absorbing and scattering agar gel (2 % in water) mimicking the optical properties of soft tissue. Embedded inside the phantom at 4±1 mm depth were two 2 % agar cylinders (diameter 2 mm, height 6 mm). One cylinder contained bovine hemoglobin (Hb) (Sigma-Aldrich, Zwijndrecht, the Netherlands) in a concentration of 15 g/L.The second cylinder contained B-16 melanin producing melanoma cells (2×10^6 cells/mm^3). The background consisted of 2 % agar completely covering the 6 mm high cylinders with a cover on the top of 4±1 mm. Multispectral volume scanning was performed using five distinct illumination wavelengths between 680 and 840 nm with 40 nm intervals. After image acquisition, the photoacoustic spectrum was obtained by selecting a 3D region of interest in each inclusion and calculating the mean values with standard deviations.

Human lymph nodes

Twelve human lymph nodes from eight melanoma patients undergoing lymphadenectomy were obtained from the surgical specimen. The experimental protocol was performed according to the Dutch guidelines for clinical research and patient's informed consent was acquired prior to surgery. The lymph nodes were stored in phosphate buffered saline before and during imaging. Subsequently, histopathology examination was performed using two or more slides stained with hematoxylin and eosin and biomarkers (S100, HMB-45, Melan-A) when needed. In order to obtain accurate reference spectra for both blood and melanin, multispectral images were acquired for each node. Five wavelengths were selected: 3 wavelengths (700 nm, 800 nm, and 820 nm) covered the near infrared range. Two additional near infrared wavelengths (732 nm and 757 nm) were selected based on the absorption spectrum of oxy- and deoxyhemoglobin; both show an increase between 732 nm and 757 nm, whereas the absorption spectrum of melanin shows a slight

decrease. In addition, at least one hyperspectral slice was acquired of every node using 101 colors of light, ranging from 700 to 900 nm with intervals of 2 nm. The photoacoustic reference spectrum of blood was obtained by selecting the vessels on the images of benign lymph nodes. The selected regions were also examined with high-resolution ultrasound and histology. In the metastatic nodes, ultrasound and histological slides were used to select an area in the photoacoustic dataset with a high melanin concentration as reference for melanin. Calculation of both a mean and a standard deviation for every measured wavelength resulted in reference spectra for both chromophores.

Unmixing algorithm

The raw photoacoustic data were first filtered with a median filter. A two-dimensional median filter (block size 5×5 pixels in the image plane: approximately 110 × 110 μm) was chosen because of the noncubical voxel dimensions: 22 × 22 × 200 μm (depth × width × slice thickness). Variations in local fluence are expected, as light is absorbed and scattered while travelling through the heterogeneous tissue. Variations in light distribution were corrected by area under the curve normalization, that is, divided by the integral over the wavelength range. This correction aims to preserve the spectral characteristics, while the influence of absolute light intensity is reduced. The normalized measured signal was then compared to the normalized reference spectra of both blood and melanoma per image voxel. The reference spectra were based on 1168 voxels for blood and 1349 for melanin, selected per wavelength from a 3D region of interest.

In order to calculate the resemblance of the measured spectrum and the reference spectra, a statistical *t*-test was performed. The *P* value (ranging 0-1) was displayed in a resulting image. The *P* value was calculated for both blood and melanin for each of the five measured wavelengths. A value close to 1 indicates high resemblance; a value closer to 0 implies an increasing discrepancy with the reference. The five *P* values are combined by multiplication, resulting in a single matching score of the voxel per reference. Voxels exactly matching the reference at all five wavelengths received an intensity of $1^5 = 1$, while voxels with two standard deviations scored $0.05^5 = 3 \times 10^{-7}$. Matching pixels light up on the resulting image, while nonmatching pixels remain dark. These grayscale images are ultimately fused with the US images, with red representing blood and green representing melanin.

Results

Phantom

Figure 3.01 shows the photoacoustic intensity maps of the phantom at 680 nm (Fig. 3.01A) and 840 nm (Fig. 3.01B). The position of the reference inclusions is schematically visualized in Figure 3.01C. Both inclusions have a signal above background, especially at the superficial part. The signal intensity inside the inclusions decreases with depth as light fluence decreases deeper inside the phantom. Examination of the photoacoustic images alone does not allow for discrimination between blood and melanin. The information for discrimination lies in combination of multiple images, acquired at different wavelengths of light. The spectra derived from the multispectral images show different patterns for blood and melanin (Figures 3.01D and 3.01E). The effect of area under the curve (AUC) normalization is characterized in the difference between the two curves. The result of the recognition algorithm shows that the two inclusions can be distinguished (Fig. 3.01F). Some matching pixels were found outside the inclusions, indicating some margin of error that could result in false positive or false negative pixel classifications.

Human lymph nodes

An overview of the measured nodes is provided in Table 1. Three of the twelve lymph
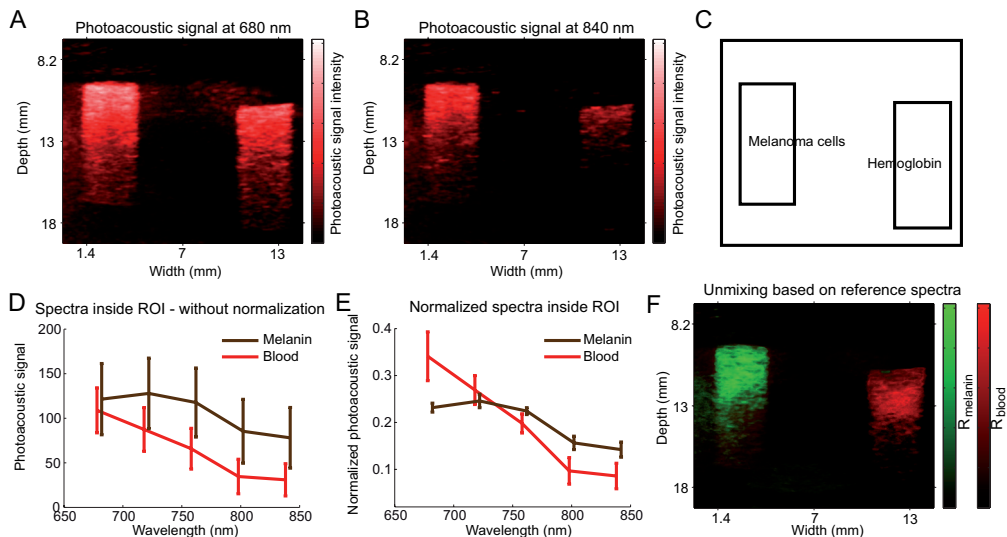

Figure 3.01. | A: Photoacoustic image of phantom after illumination with 680 nm light. B: Photoacoustic image of phantom after illumination with 840 nm light. C: Relative position of the inclusions in A, B, and F. D: Measured spectra for the two regions indicated in C for five wavelengths before normalization. The curves represent average and error bars indicate standard deviation. E: Reference spectra after per-pixel normalization. The curves represent average and the error bars indicate standard deviation. F: Resemblance score for blood (R_{blood}) and melanin ($R_{melanin}$) expressed as pseudocolors, hemoglobin in red and melanin in green.

Patient	Age	Gender	Node	Histology	Node longest diameter (cm)	Used as reference
1	37	Male	1	benign	0.5	
2	65	Female	2	malignant	1.4	yes
3	24	Female	3	benign	1.0	yes
4	62	Male	4	benign	0.9	
			5	benign	1.1	yes
5	79	Female	6	Malignant*	1.2	
6	62	Female	7	benign	0.6	
			8	benign	1.5	yes
7	38	Male	9	benign	1.2	
			10	benign	0.8	
8	25	Female	11	malignant	1.2	yes
			12	benign	1.8	yes

* Amelanotic melanoma

nodes contained melanoma metastases according to histopathological examination, one of which was amelanotic. The reference spectrum of blood was based on over 8000 pixels of blood vessels in four tumor-negative lymph nodes from

four different patients (Fig. 3.02). The reference spectrum of melanin was based on over 2200 pixels of two tumor-positive lymph nodes from two patients. The spectral differences between blood and melanoma are best reflected in the gradual slope of the photoacoustic signal from melanoma compared to the increase in photoacoustic signal from blood in
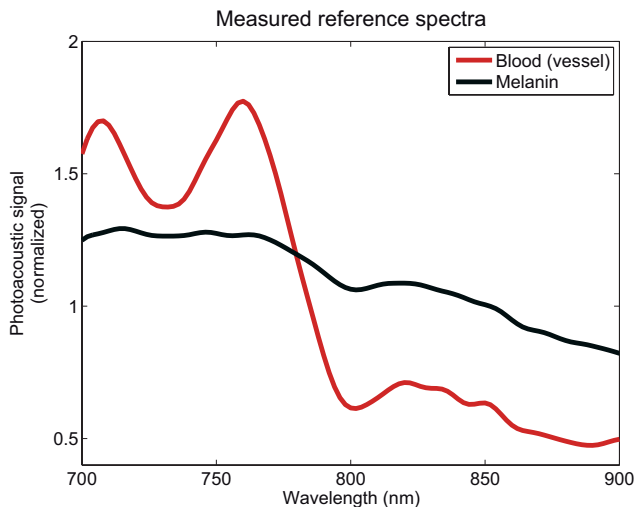

Figure 3.02. | Normalized measured reference spectra for blood and melanin. The spectral differences between blood and melanoma are best reflected in the gradual slope of melanoma compared to the increase of blood in the wavelength range between 732 and 756 nm.

the wavelength range between 732 and 0756 nm in Figure 3.02. The ultrasound image of a tumor positive lymph node, node number 2 in Table 1, (Fig. 3.03A) visualizes the node as a round structure, surrounded by hyperechogenic fatty tissue. The corresponding photoacoustic image shows strong signal at the surface of the node, nearby the detector, while lack of signal can be noticed at a larger distance from the surface. The strong optical absorption of the melanin deposits limited the light penetration to 2-3 mm. The result of the spectral unmixing procedure (Fig. 3.03C) shows a green strip overlaying the ultrasound image. The green represents image elements spectrally according to melanin. In this figure, almost no elements were found with a spectral response corresponding to
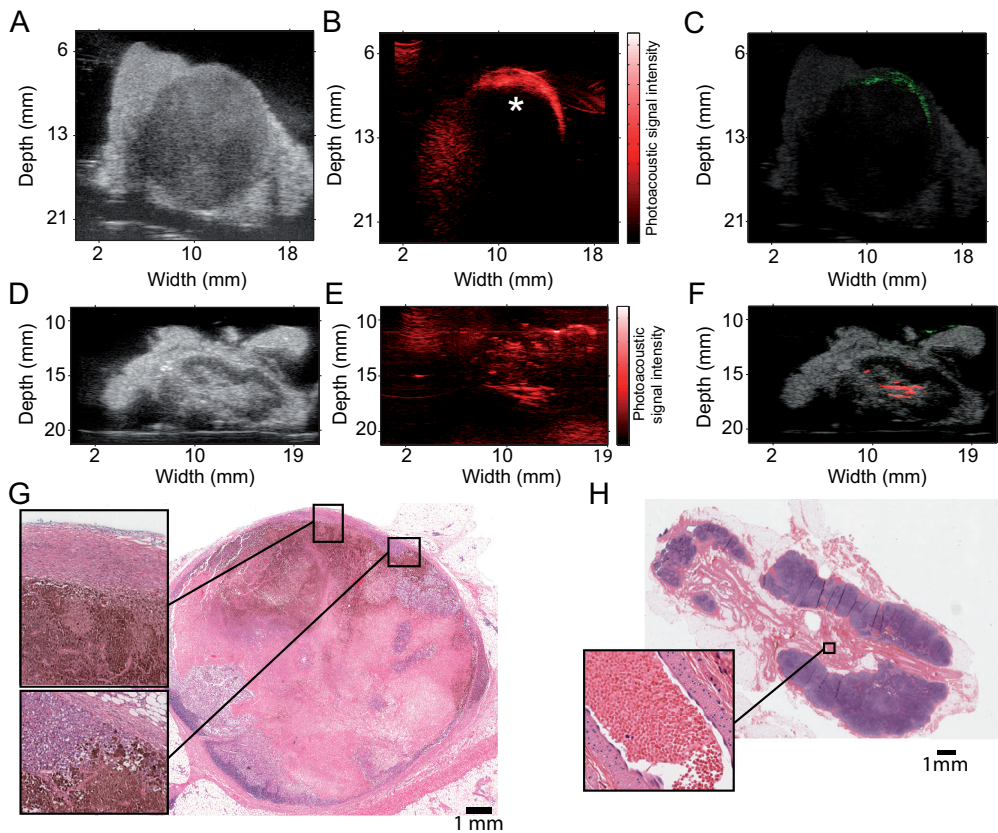
Figure 3.03. | Images of two human nodes. The first row shows images of a metastatic node (node number 2 from Table 1); the second row shows images of a benign node (node number 3 from Table 1). Three columns represent, respectively, high-resolution ultrasound, photoacoustic signal, and the calculated resemblance. The third row shows the pathology slides of the metastatic node (G) and the normal node (H). Absence of photoacoustic signal deeper in the malignant node (as indicated by * in B) seems to be caused by the strong absorption by the melanin in the superficial area of the node. The green area in (c) corresponds to the superficial layer of the dark area in G. The red structure in F corresponds to the vessels in the hilum of the benign lymph node (H).

blood. This is in accordance with the histological slide (Figure 3.03G) in which melanin is found in the upper part of the node (dark brown) and no larger vessels are seen inside the nodal capsule.

A representative benign node, node number 3 in Table 1, shows larger vessels entering the hilum of the node (Figures 3.03D–3.03F and 3.03H). The ultrasound (Fig. 3.03D) visualizes a bean shaped node with a brighter hilum surrounded by bright fatty tissue. The photoacoustic image (Fig. 3.03E) shows vessel shaped structures at 16 mm depth and signal at the surface of the fatty tissue. The vessel shaped structures are recognized as blood in the algorithm-result imaging; the signal at the surface of the fatty tissue does not resemble the reference of blood nor melanin. Histopathology slides (Fig. 3.03H) confirm the location of the blood vessels within the hilum of the node. Within 20 minutes, total volume imaging proved possible for the benign lymph nodes, where penetration was sufficient to examine the entire nodes, which were up to 2 cm in diameter (Fig. 3.03).

Tumor-positive nodes have different melanin distribution, which may result in different photoacoustic signal distribution. In Figure 3.04, the photoacoustic signal of node number 11 from Table 1, containing tumor metastasis, is compared with its corresponding histopathology slide. Compared to the first tumor-positive lymph node (Fig. 3.03), the melanin distribution is more scattered throughout the node (Fig. 3.04A) resulting in a more diffuse distribution of green photoacoustic pixels (Fig. 3.04B). Also the number of blood

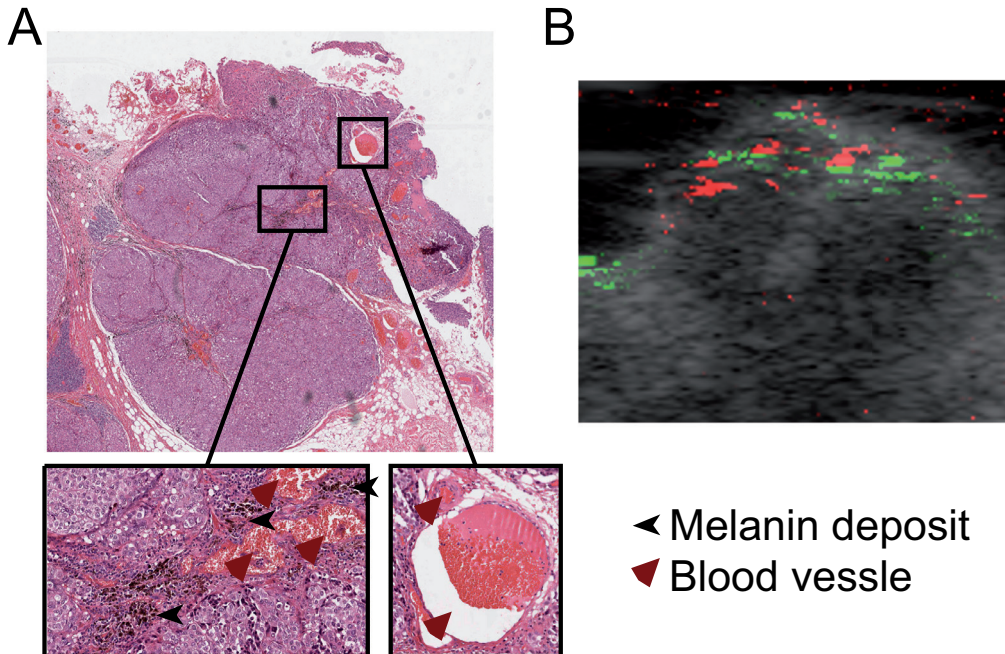◄ Melanin deposit
▼ Blood vessle

Figure 3.04. | Pathology slide (A) and photoacoustic image (B) image of a second tumor-positive lymph node (node 11 from Table 1). This node has more blood vessels and less melanin deposits compared to the node in Figure 3.03. Blood vessels and melanin in the upper part of the node are more intertwined.

vessels seems higher in this node which is reflected in the corresponding photoacoustic images (Figures 3.04B and 3.03C). Direct comparison of the photoacoustic images and the pathology slides is, however, hampered by the handling of the nodes in between.

Discussion

Earlier studies showed that photoacoustic imaging can detect melanin in lymph nodes, but the specificity was low as the signal from melanin could not be differentiated from blood. The results of this feasibility study show that it is possible to distinguish the photoacoustic signals of blood and melanin both in phantoms and in resected human lymph nodes. The implemented unmixing procedure allows discrimination between melanin and blood. Because the technique is based on spectral comparison, one should keep in mind that the accuracy of unmixing is strongly tied to the reference spectra. The presented reference spectra show similarity with known optical absorption spectra for hemoglobin (oxyhemoglobin + deoxyhemoglobin) and eumelanin[8,9]. The gradual slope in the spectrum of melanin and the increase between 732 nm and 756 nm for hemoglobin is characteristic in both optical absorption and the reference spectra. However, the reference spectra should encompass the response in a variety of situations, which requires a multitude of human samples to be scanned in further studies.

Specific detection of melanin can be useful in intraoperative photoacoustic imaging of an excised sentinel node. This would permit an immediate node dissection if metastatic foci are demonstrated and would obviate the need for a second operation. Perhaps the sentinel node could even be analyzed in vivo. A penetration depth of 2 cm in the absence of melanin deposits enables the analysis of the entire nodal volume. This is in contrast with the conventional pathology evaluation that samples less than 0.1 % of a node.

When present, melanin absorbs most of the light and limits the depth of photoacoustics imaging under these circumstances. For clinical application this may be of limited importance, since the extent of tumor involvement per node is presently of less relevance. Also the presence of a blue dye, generally used for sentinel node detection, may alter the penetration depth of optical imaging. However, the impact on melanoma detection will be limited since the optical absorption of blue dye in the infrared region is limited and the optical absorption spectrum of the dye is clearly distinctive from both blood and melanin.

A false positive test result may be realistic because normal naevus cells are present in one-third of the skin draining lymph nodes. Additional research should reveal whether adequate reference spectra for these kinds of conditions can still be defined.

As photoacoustic imaging relies on optical absorption, the 1.8 % to 8.1 % amelanotic melanomas may challenge the sensitivity of the procedure[10]. An occasional false negative procedure will not have major detrimental consequences, because a strong point of photoacoustic scanning is that histological and immunohistochemical analysis afterwards remains possible. Therefore, a false negative procedure does permit a node dissection,

albeit at a somewhat later date. Recent reports describing molecular based staging methods do not allow for this option, because these techniques destroy the tissue during the procedure[11,12].

Conclusion

A method is proposed to detect melanoma metastases in human lymph nodes using multispectral photoacoustic imaging. The method was conducted on a set of lymph nodes containing tumor positive and tumor negative nodes. Separation of important optical absorbers like blood and melanin proved possible based on the spectral information. Lymph nodes could be analyzed in image planes and also as entire nodal volumes (3D).

In hybrid photoacoustic imaging, the high resolution ultrasound imaging can be used for orientation, as well as for diagnosis, as in conventional ultrasound. The two techniques are synergetic as they are based on different imaging contrasts; ultrasound is based on acoustic impedance which is sensitive to anatomy and photoacoustics on light absorption which is sensitive to molecular properties. The reflective mode hand-held system proved capable of 3D imaging of the entire lymph node. Further research should be directed towards the robustness of this technology for the detection of small melanoma lesions within human lymph nodes and its specificity.

References

1. Morton, D.L., et al., Sentinel-node biopsy or nodal observation in melanoma. N Engl J Med, 2006. 355(13): p. 1307-17.

2. Creager, A.J., et al., Intraoperative evaluation of sentinel lymph nodes for metastatic melanoma by imprint cytology. Cancer, 2002. 94(11): p. 3016-3022.

3. Tanis, P.J., et al., Frozen section investigation of the sentinel node in malignant melanoma and breast cancer. Annals of surgical oncology, 2001. 8(3): p. 222-226.

4. Wong, S.L., et al., Sentinel lymph node biopsy for melanoma: American Society of Clinical Oncology and Society of Surgical Oncology joint clinical practice guideline. Journal of Clinical Oncology, 2012. 30(23): p. 2912-2918

5. Grootendorst, D.J., et al., First experiences of photoacoustic imaging for detection of melanoma metastases in resected human lymph nodes. Lasers Surg Med, 2012. 44(7): p. 541-9

6. Jose, J., et al., Initial results of imaging melanoma metastasis in resected human lymph nodes using photoacoustic computed tomography. Journal of biomedical optics, 2011. 16(9): p. 096021-096021-5

7. Wang, L.V., Prospects of photoacoustic tomography. Med Phys, 2008. 35(12): p. 5758-67

8. Molar extinction coefficient for hemoglobin in water. 1999, Oregon Medical Laser Center

9. Molar extinctioncoefficient for melanin. 1999, Oregon Medical Laser Center

10. Koch, S.E. and J.R. Lange, Amelanotic melanoma: the great masquerader. J Am Acad Dermatol, 2000. 42(5 Pt 1): p. 731-4

11. Iinuma, H., et al., Accurate and rapid novel genetic diagnosis for detection of sentinel lymph node metastasis in breast cancer patients. Br J Cancer, 2012. 107(4): p. 724-31

12. Godey, F., et al., Sentinel lymph node analysis in breast cancer: contribution of one-step nucleic acid amplification (OSNA). Breast Cancer Res Treat, 2012. 131(2): p. 509-16
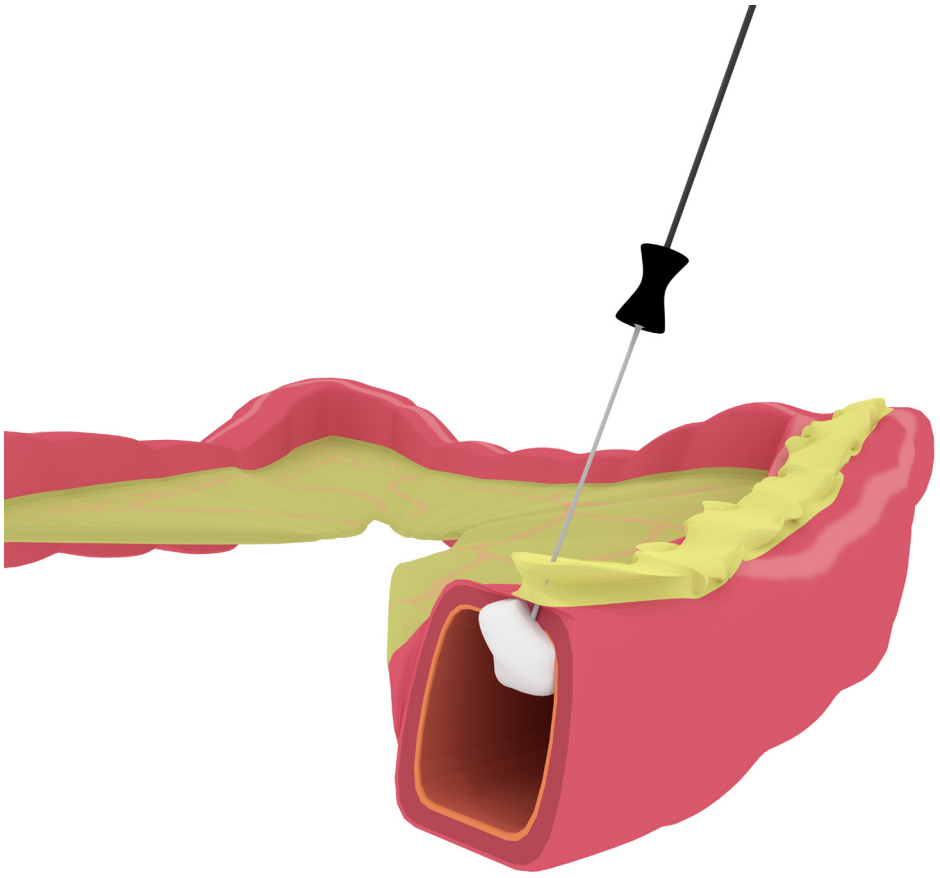
3

Differentiation of healthy and malignant tissue in colon cancer patients using optical spectroscopy: a tool for image guided surgery

Surgery for colorectal cancer aims for complete tumor resection. Optical based techniques can identify tumor and surrounding tissue through the tissue specific optical properties, absorption and scattering, which are both influenced by the biochemical and morphological composition of the tissue.

To evaluate the feasibility of dual-modality Diffuse Reflectance Spectroscopy – Fluorescence Spectroscopy (DRS-FS) for discrimination between healthy and malignant tissue in colorectal surgery.

Surgical specimens from colorectal cancer patients were measured immediately after resection using a fiber-optic needle capable of dual-modality DRS-FS. Model-based analyses were used to derive scattering and absorption coefficients and intrinsic fluorescence. Volume fractions of chromophores were estimated. Furthermore, optical data were recorded along a trajectory from healthy tissue towards tumor.

Results: Spectral characteristics were identified in 1273 measured spectra from 21 specimens. Combined DRS and FS discriminated tumor from surrounding tissue with a sensitivity of 95 % and a specificity of 88 %. Significant spectral changes were seen along the trajectory from healthy tissue to tumor.

This study demonstrates that dual-modality DRS-FS can identify colorectal cancer from surrounding healthy tissue. The quantification of comprehensible parameters allows robust classification and facilitates extrapolation towards the clinical setting. The technique, here demonstrated in a needle like probe, can be incorporated into surgical tools for optically guided surgery in the near future.

G.C. Langhout, J.W. Spliethoff, S.J. Schmitz, A.G.J. Aalbers, M-L.F. van Velthuysen,

B.H.W. Hendriks, T.J.M. Ruers, K.F.D. Kuhlmann

Introduction

The outcome and quality of life after surgery for colorectal cancer is influenced by multiple factors. The surgical success relies to a great extent on the complete removal of the primary tumor. According to the Dutch surgical colorectal audit of 2012, resection was incomplete in 8.5-30 % of the patients operated for rectal cancer. An incomplete surgical resection not only increases the risk for local recurrence but also affects overall survival. For rectal cancer, an incomplete resection is associated with a hazard ratio of approximately 3 for developing local recurrence and distant metastasis[1]. Pursuing wide margins can cause damage to the presacral plexus increasing the risk of urinary incontinence and erectile impotence. Therefore, timely recognition of an inadequate resection plane is of utmost importance for surgical outcome.

Optical spectroscopy has been shown to improve the identification of tumors of various origin[2-5]. The technique enables tissue characterization by measuring the spectral response after the tissue is illuminated with a selected spectral band of light. Depending on the morphological composition and biochemical make-up of the tissue, a specific "optical fingerprint" is acquired. Within optical spectroscopy, several techniques can be distinguished such as Diffuse Reflectance Spectroscopy (DRS) and Fluorescence Spectroscopy (FS). With DRS, tissue is illuminated with white light. The reflected light, influenced by tissue interactions, is analyzed for spectral changes. In this way different chromophores in the tissue such as hemoglobin (oxygenated and deoxygenated), β-carotene, water, lipids, and collagen can be recognized and quantified. In addition, the scattering coefficient which contains information about the underlying cellular structures is derived. FS adds the possibility to detect intrinsic fluorophores in the measured tissue, such as collagen, elastin, FAD, NADH and porphyrins. Collagen and elastin are structural proteins and are associated with tissue structure, whereas NADH and FAD levels are indicative for cellular energy metabolism.

For both techniques reliable identification of tumor tissue and surrounding normal tissue has been reported for breast, lung and liver tumors[6-8]. For primary colorectal cancer, optical spectroscopy has mainly been used during colonoscopy procedures[4,9-11], hence approaching the tumor from the luminal side. In these studies, tumor could be differentiated from healthy tissue with a sensitivity and specificity up to 90%. The types of tissue encountered in colonoscopy are limited to (pre-)malignant tissue and healthy mucosa: the inner lining of the colon. During colorectal surgery, tumor demarcation is less clear and tumor tissue must be differentiated from several other surrounding tissue types in order to find an adequate surgical plane. Optical tissue identification either using a probe or incorporated into dissection instruments could prevent dissection through tumor and help in maintaining an adequate dissection plane. DRS analysis of tissue types during colorectal surgery are scarce. Basic anatomy of the colon includes the inner layer (mucosa) which is rich on water, a middle layer rich on muscle and collagen and the

outer layer (serosa). Furthermore, the colon is covered by lipid rich structures such as appendices epiploica and mesocolon (Fig 4.01). During colorectal surgery these tissue structures should be recognized.

The aim of this study is to investigate the potential of DRS and FS for real time tissue sensing during surgery for colorectal cancer. To this end spectroscopic measurements were acquired from freshly excised specimens of patients undergoing surgery for colorectal cancer.
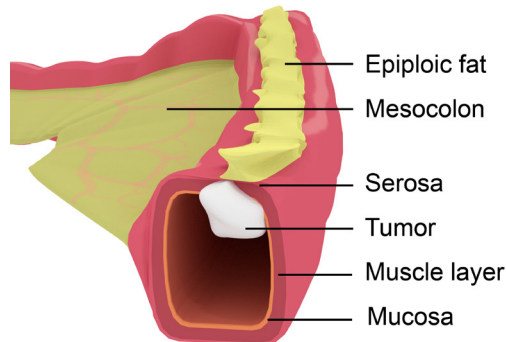

Figure 4.01. | *Basic anatomy of the colon. From the inside of the colon (lumen): mucosa, muscle, and a thin outer layer called serosa. Vessels within fatty mesocolon supply the colon with blood.*

Materials and Methods

Study design

This study was performed at The Netherlands Cancer Institute – Antoni van Leeuwenhoek hospital under approval of the ethics review board. Twenty-one patients with a colorectal primary tumor were randomly selected. Immediately after removal of the resection specimen, spectroscopic measurements were performed on macroscopically defined tumor tissue and normal surrounding tissue types (epiploic fat, mesocolon and colon wall) within the resected specimen. Tumor tissue was sampled for histological analysis.

Spectroscopy system and optical probe

DRS and FS spectra were acquired using a portable spectroscopy system that has been described earlier[6,8]. The system consists of two light sources and two spectrometers (Fig. 4.02). For the DRS measurements, a Tungsten halogen broadband light source (360-2500 nm) was used, with 1.5 mW fiber output. For FS, the system was equipped with a semiconductor laser (377 nm, 0.4 mW) to induce autofluorescence. Two spectrometers resolve the light from the visible wavelength range (400 up to 1100 nm: DU420A-BRDD;

Andor Technology, Belfast, Northern Ireland), and the near infra-red light (900 up to 1700 nm: DU492A-1.7 Andor Technology, Belfast, Northern Ireland). A custom made 13 G (1.5 mm) optical probe was used containing four identical fibers with a core diameter of 200 µm. The tip of the probe was beveled to an angle of 30 degrees. Two fibers were connected to the broadband light source and laser, while two other fibers were connected to the spectrometers to capture light from the tissue. Two different source-detector distances (SDDs) were used (1.8 and 0.32 mm). The spectra acquired with the 1.8 mm SDD were used for the DRS data analyses, whereas the DRS spectra measured with the 0.32 mm SDD were used to correct for absorption and scattering in the fluorescence spectra.
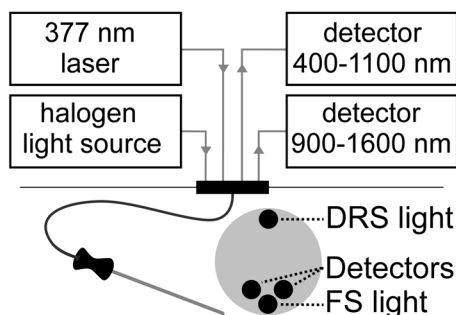

Figure 4.02. | Schematic of the measurement setup. The setup contains two light sources, two detectors, and a fiber optic probe. The configuration of the fibers in the tip is represented in the lower right.

DRS data acquisition

Tissue measurements were performed immediately after resection of the specimen. DRS and FS measurements were done consecutively using the same probe, thus creating the aspect of a single measurement. Tumor spectra were acquired after positioning the needle directly onto the macroscopically recognized tumor tissue. Thereafter, a biopsy was taken from this area. The presence of malignancy was confirmed by histopathological examination. Tissue measurements were performed on multiple locations in healthy and malignant tissue. Healthy colon structures (epiploic fat, mesocolon and colon wall) were measured after placing the probe on the selected tissue at least 5 cm from macroscopically visible tumor tissue.

In 10 specimens, trajectory measurements were performed during line insertions. During these measurements, the probe was introduced from macroscopically normal healthy tissue towards the tumor, with measurements taken consecutively in the epiploical fat, colon wall and colon tumor. For correlation with histology, a cylindrical core biopsy was obtained from the measurement trajectory. Samples were stained with standard hematoxylin/eosin (H&E) staining and examined by a pathologist who was blinded to the spectroscopy results.

Spectral analysis

DRS analytical model. To interpret the acquired DRS spectra a widely accepted analytical model, introduced by Farrell et al.[12], was used to estimate the various DRS chromophore volume fractions and scattering parameters. The main absorbing constituent (chromophore) in normal tissue dominating the absorption in the visible range is hemoglobin (oxygenated and deoxygenated), whereas water, fat and collagen are the main absorbers in the near infra-red range. The main scattering parameters are the reduced scattering at 800 nm and the Mie-to-total scattering fraction, in which the total scattering of tissue is assumed to be defined by Mie and Rayleigh scattering. The validation of the DRS analytic method has been described previously[13,14]. The input arguments for the model are the absorption coefficient μa (λ), the reduced scattering coefficient $\mu s'$ (λ) and the center-to-center distance between the emitting and collecting fibers at the tip of the probe. The implementation of this model to analyze diffuse reflectance spectra over a wavelength of 400-1600 nm is described by Nachabé[13].

FS analytical model. Autofluorescence was calculated by correcting the collected fluorescence spectra for absorption and scattering using a method described earlier[15,16]. The model was implemented according to Müller[15], based on a modified photomigrations model described by Müller[16]. The corrected spectra were fitted using the intrinsic fluorescence spectra (excitation at 377 nm) of collagen, elastin, NADH and FAD as a priori knowledge.

Within colorectal tumors specific fluorescence peaks may occur related to the accumulation of porphyrins, such as protoporphyrin IX (PpIX)[17-19]. Quantification of porphyrins using the standard fit routine is not feasible since the exact wavelength of their fluorescence bands are dependent on the environment where it is measured[20]. The porphyrin specific fluorescence was quantified by the subtraction of two curves: The area underneath the recorded spectrum was subtracted from an interpolation (p-chip method) between the measured values at 615, 650 and 730 nm. At these wavelengths the intensity of the porhyrin fluorescence is at a minimum (Fig. 4.03).

Classification and statistics

To evaluate the performance of discriminating the different tissue types, a Classification And Regression Tree (CART) algorithm was used. The CART algorithm is a recursive partitioning method that creates a classification tree based on the estimated parameters from the fit model[21]. A leave-one-out (LOO) cross validation scheme was used[6]. Each measurement location was separately classified as healthy or tumor tissue using the classification tree. Measurements from a single measurement position were combined after estimation of the parameters, prior to classification. Three parameters (hemoglobin concentration, hemoglobin saturation, and optical redox) may be strongly influenced by the surgical procedure, either because of hemorrhage or devascularisation during surgery.
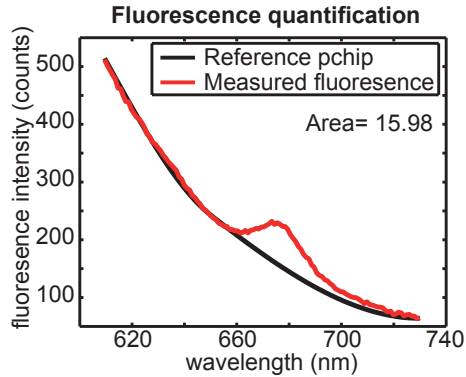
Figure 4.03. | Quantification of fluorescence peaks around 630 and 680nm by p-chip interpolation between point 610, 660, and 730 nm. The fluorescence is quantified as difference in area under the curve between measured fluorescence and interpolation.

These parameters may differ considerably between ex vivo measurements (as performed in the present study) and the planned in vivo application of the technology in the near future. Therefore these parameters were excluded from the CART classification. The outcome of the classification was compared to the tissue type to calculate the sensitivity, specificity, and overall accuracy. Statistical significance of the differences in estimated DRS and FS parameters were calculated using the non-parametrical Mann Whitney U test. P values smaller than 0.01 were considered significant.
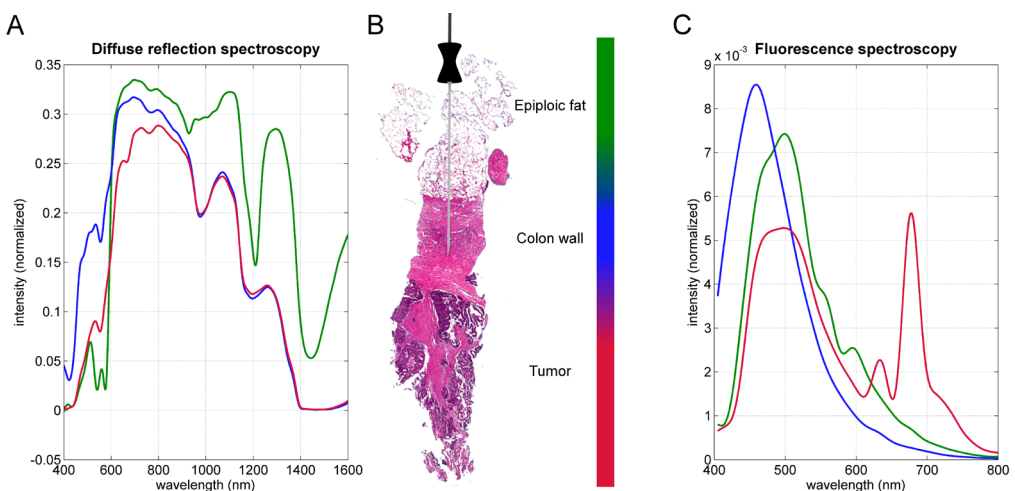

Figure 4.04. | DRS (A) and FS (C) spectra with corresponding histology (B). The color of the spectral lines refers to the measurement position, indicated by the color bar at the center (B).

Results

Patients

A total number of 21 patients was included, 10 males and 11 females. Mean age was 64 years (± 8.8). Three patients received Capecitabine plus Oxaliplatin as neo-adjuvant therapy, with at least 28 days (range 28-120 days) between last treatment and surgery. None of the patients received neo-adjuvant radiation therapy. Three tumors were located in the right colon, 1 in the transverse colon and 17 in the left colon including (recto)sigmoid. Tumor size varied from 1.6 to 9.1 cm (mean: 4.7 ± 2.0 cm). All tumors were histologically proven adenocarcinomas.

Tissue spectra

A total of 1273 optical measurements were performed; 603 as separate tissue measurements on the different tissues (276 on tumor, 122 on colon wall, 130 on epiploic fat and 75 on mesocolon) and 670 measurements as part of line measurements. 17 Measurements (1.3 %) were removed due to errors in the measurement (e.g. influenced by photo camera flashlight or a lack of tissue contact).

Examples of varying DRS and FS spectra between tissues are shown in Figure 4.04. The measurements in the epiploic fat show a sharp dip in the DRS spectrum around 1200 nm which is not present in the measurements of the normal colon wall and the tumor tissue. This dip is a result of lipid absorption. Histology confirms the high fat content in the epiploic fat when compared to normal colon wall and tumor tissue. The spectrum of normal colon wall and tumor tissue mainly differs in the visible part of the spectrum (400 - 750 nm). Figure 4.04C shows the fluorescence spectrum with typical fluorescence peaks measured in tumor tissue in the wavelength range between 600 and 700 nm.

Tissue parameter quantification

Quantification of absorption- and scattering parameters was performed for each measurement location. Box plots of the most significant parameters are shown in Figure 4.05. Tissue containing considerable amounts of fat, i.e. epiploic fat and mesocolon, were best distinguished from colon wall and tumor by fat, water and β-carotene contents. Compared to epiploic fat, the mesocolon tissue showed a higher percentage of blood. When comparing tumor tissue with all three healthy tissue types, considerable differences were found for hemoglobin content ($P<0.001$) and the Mie-to-total scattering fraction ($P<0.001$).

For FS measurements, significant differences between tumor and normal tissue were observed for the optical redox ratio and the fluorescence peaks at 630 and 680 nm. Fluorescence peaks around 630 and 680 nm were seen in 64 % of the tumor locations.

These peaks were highly predictive for tumor tissue with a positive predictive value of 97 %. No considerable trends were seen for the total fluorescence intensity, NADH, FAD, collagen, and elastin.

Classification accuracy

The DRS and FS parameters were used by the CART algorithm to create a classification tree and calculate overall diagnostic accuracy when compared to histopathology. The main parameters used in the CART algorithm were mie scattering and water content, with fat
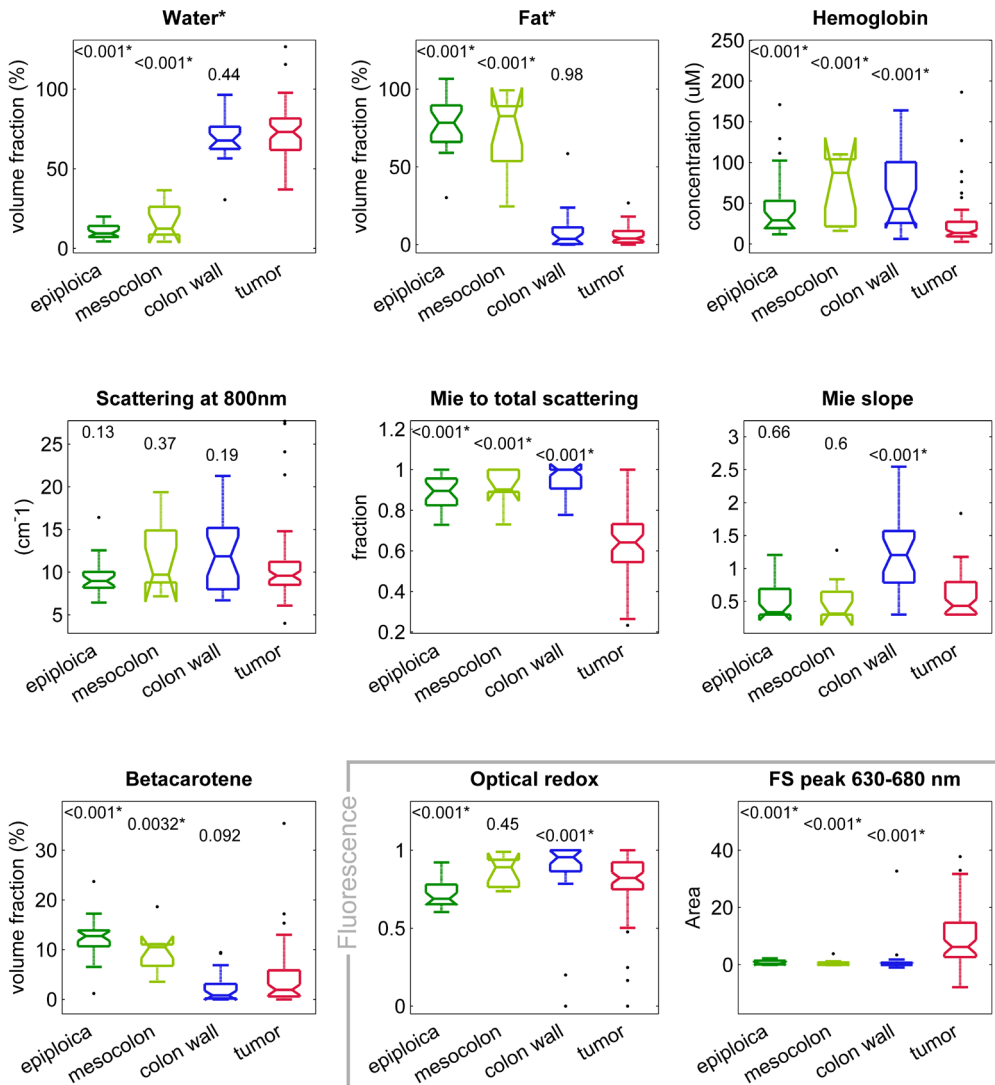

Figure 4.05. | Box plots of the relevant tissue parameters. The significance levels (p-value) depicted above each bar indicates the significance of the difference between the tissue in that column and tumor tissue, based on a Mann–Whitney U test. Asterisks indicate significance levels <0.01.

content and FS peaks as secondary parameters. The overall accuracy for discriminating between tumor and all healthy tissue using these DRS and FS parameters was 91 % with a sensitivity of 95 % and a specificity of 88 %.

Line measurements

Line measurements were performed by introducing the needle shaped probe slowly towards the tumor, passing through (if present) epiploic fat, colon wall, and tumor (Fig. 4.04B). During the line measurements, changes in tissue composition could clearly be recognized. A typical example of the development in tissue composition during the trajectory measurements is shown in Figure 4.06. During the propagation from surface to tumor tissue, the water content increases, while the concentration of fat and mie-scattering decreases. Fluorescence peaks (630 and 680 nm) are clearly noticed when the probe reaches the tumor tissue.
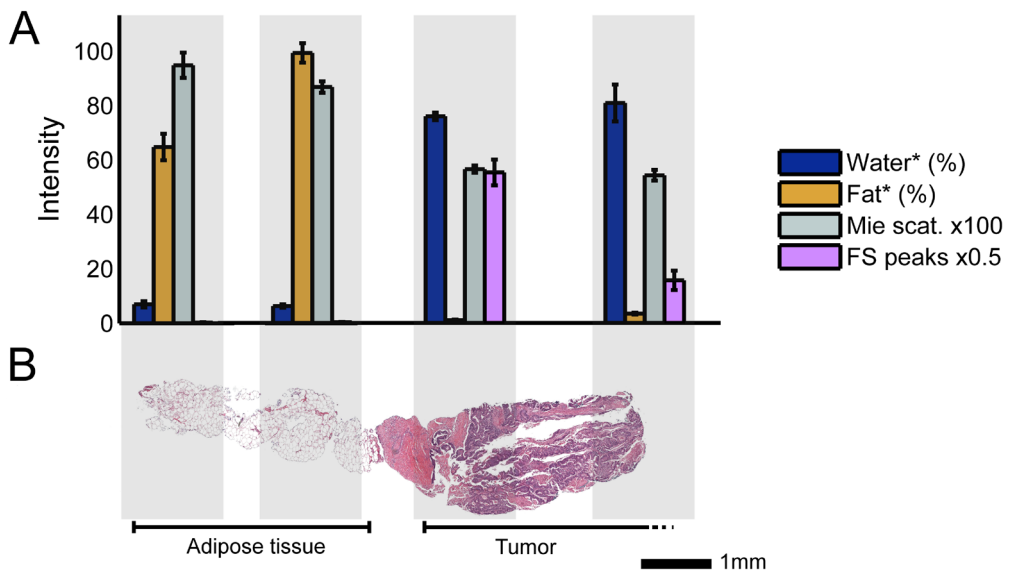
Figure 4.06. | *Visualization of a line measurement. The optical probe was introduces in the epiploic fat and slowly commenced towards the tumor tissue. Parameter values are grouped per measurement location in a line measurement (A). The error bars represent the standard deviation of the repeated measurements at this location. The positions are correlated to the histological image (H&E stain) from a core biopsy taken just adjacent the optical probe (B).*

Discussion

In the present study, a combination of DRS and FS was used to measure differences in tissue physiology and morphology in fresh resection specimens from 21 patients with histologically proven colorectal adenocarcinoma. Automated analysis of the measured spectra revealed qualitative and quantitative parameters that differentiate tumor from healthy surrounding tissue. Water content, fat content, the scatter parameter mie-to-total and the additional FS peaks at 630 and 680 nm were most discriminating parameters.

Classification of epiploic fat and mesocolon versus colon wall and tumor was strongly based on water and fat content. General differences between tumor and colon wall were related to differences in scattering parameters, the redox ratio and the presence of additional intrinsic fluorescence peaks. These differences may directly reflect differences in morphology and metabolism between normal colon wall and tumor tissue.

The measured fluorescent spectra in colon tumor closely resemble the spectra of protoporphyrin IX, as described earlier[17,18]. Several other studies also showed the accumulation of PpIX in colon malignancies and their metastases[17,19,22]. Moesta et al. determined the fluorescence spectra of colon tissue using a pulsed solid-state laser together with a CCD-camera. PpIX was biochemically identified in the primary colon tumor as well as in the lymphatic and liver metastases using reversed phase liquid chromatography. The reason for selective accumulation of PpIX is still not fully understood. Porphyrin was also reported as decay product of chlorophyll, present in the diet of both human and laboratory animal[23]. This may complicate selective PpIX recognition.

Multiple authors have investigated the use of optical spectroscopy in the diagnosis of colon cancer. Elastic scattering spectroscopy in colonoscopy has shown discrimination between malignant and benign tissue with a sensitivity and specificity ranging from 75-90 %[4,9,10]. The surgical relevance of these studies is, however, limited since only tissue in direct contact with the lumen was investigated. Schols et al. investigated DRS as single technique on surgical specimens[24]. The fiber optic probe contained seven fibers for tissue illumination, placed around a central collecting fiber with an inter-fiber distance <0.5 mm. Principal component regression (PCR) was used for automated tissue classification. A cumulative distribution function (CDF, maximum score 1.0) rather than sensitivity and specificity was used to qualify tissue recognition. Cancer versus all other tissue yielded a high CDF score of 0.99.

The innovation of the current, here presented, study lies in the use of clinically comprehensible parameters for tissue identification. Tissue differentiation by quantitative parameters may give a better insight in the technology and its potential use during surgery.

Translating DRS-FS technology from ex vivo to in vivo measurements is complex. Quantitative analysis, as performed in the present study, provides knowledge on the contribution of specific optical parameters. In vivo and ex vivo measurements may differ

significantly with regard to specific parameters. For example, hemoglobin concentration, oxygen saturation and the optical redox ratio may change during and after resection due to a decreased cellular metabolism and cut-off blood supply. These differences will influence the measured spectrum indisputably. With an in vivo application in mind, ex vivo classification of the tissue should therefore preferably not be based on spectral characteristics or parameters prone to differ between in vivo and ex vivo. The quantification of individual parameters, as presented in our study, allows for specific parameters to be selected for classification eliminating possible shortcomings of the ex vivo measurements. Although, hemoglobin concentration, oxygen saturation and the optical redox ratio were not used for classification, parameter quantification was includes in the results (Fig. 4.05.). To extend the possibility of independent parameter quantification, the spectrum was measured over a broad spectral range (400-1600 nm). The influence of hemoglobin in the near-infrared and short wavelength infrared is minimal. In this way, parameters with spectral characteristics in the infrared, like water and fat, can be quantified without the interference of blood. Another benefit of parameter quantification is the ability to constrain the influence of ink after tattooing of colon wall during colonoscopy. The ink is quantified as independent parameter and could either be left out or included in the classification algorithm.

Clinical application of the technique could be targeted to situations with a high risk of incomplete resection or with a high risk of damaging vital surrounding structures. Large T4 and low rectal tumors are prone to these risks. When the colorectal tumor is grows into the fat of the mesorectum, a close relation with nerves of the presacral plexus often challenges the resection. In this case, the differentiation between tumor and meso is most important. In the optimal case, tumor is resected enclosed with a layer of healthy tissue. The DRS technique could be used to further investigate regions at risk or suspected for incomplete tumor resection. The depth profile of DRS depends on both tissue properties and parameters of the probe setup. The penetration depth of an optical probe can be tailored by choosing different distances between the emitting and collecting fibers[25]. When the distance between the emitting fiber and the collecting fiber increases, the penetration depth of the signal will increase, while resolution decreases. Currently, we are developing optical probes that incorporates multiple optical fibers with various inter fiber distances. These probes allow tissue measurements at a depth of several millimeters. In addition, they allow measurements at different fiber distances and in this way may supply information about the distance of the identified tissue to the optical probe. Recommendations for further research would include optical observational optical measurements in vivo in human. Eventually research could also be aimed at detecting small amount of tumor deposits.

In summary, dual-modality DRS-FS is feasible for detecting colorectal cancer. During line measurements, optical spectra and derived parameters could be correlated to the simultaneously acquired core biopsy. Group differences in parameter values are

significant and assignable. In addition, classification between different healthy tissue types is possible. These findings indicate that optical spectroscopy may be a valuable technology for image guided surgery in colorectal cancer. Especially when the small fibers are integrated into surgical tools for direct and real time tissue feedback.

Conflicts of Interest and Source of Funding:

References

1. Nagtegaal ID, Quirke P. What is the role for the circumferential margin in the modern treatment of rectal cancer? Journal of Clinical Oncology 2008; 26(2):303-312.

2. Bard MP, Amelink A, Skurichina M, Hegt VN, Duin RP, Sterenborg HJ, Hoogsteden HC, Aerts JG. Optical spectroscopy for the classification of malignant lesions of the bronchial tree. CHEST Journal 2006; 129(4):995-1001.

3. Zhou C, Choe R, Shah N, Durduran T, Yu G, Durkin A, Hsiang D, Mehta R, Butler J, Cerussi A. Diffuse optical monitoring of blood flow and oxygenation in human breast cancer during early stages of neoadjuvant chemotherapy. Journal of Biomedical Optics 2007; 12(5):051903-051903-051911.

4. Wang H-W, Jiang J-K, Lin C-H, Lin J-K, Huang G-J, Yu J-S. Diffuse reflectance spectroscopy detects increased hemoglobin concentration and decreased oxygenation during colon carcinogenesis from normal to malignant tumors. Optics Express 2009; 17(4):2805-2817.

5. Brown JQ, Bydlon TM, Richards LM, Yu B, Kennedy SA, Geradts J, Wilke LG, Junker MK, Gallagher J, Barry WT. Optical assessment of tumor resection margins in the breast. Selected Topics in Quantum Electronics, IEEE Journal of 2010; 16(3):530-544.

6. Nachabé R, Evers DJ, Hendriks BH, Lucassen GW, van der Voort M, Rutgers EJ, Peeters M-JV, Van der Hage JA, Oldenburg HS, Wesseling J. Diagnosis of breast cancer using diffuse optical spectroscopy from 500 to 1600 nm: comparison of classification methods. Journal of Biomedical Optics 2011; 16(8):087010-087010-087012.

7. Evers D, Nachabé R, Hompes D, van Coevorden F, Lucassen G, Hendriks B, van Velthuysen M-L, Wesseling J, Ruers T. Optical sensing for tumor detection in the liver. European Journal of Surgical Oncology (EJSO) 2012.

8. Spliethoff JW, Evers DJ, Klomp HM, van Sandick JW, Wouters MW, Nachabe R, Lucassen GW, Hendriks BH, Wesseling J, Ruers TJ. Improved identification of peripheral lung tumors by using diffuse reflectance and fluorescence spectroscopy. Lung cancer 2013.

9. Dhar A, Johnson KS, Novelli MR, Bown SG, Bigio IJ, Lovat LB, Bloom SL. Elastic scattering spectroscopy for the diagnosis of colonic lesions: initial results of a novel optical biopsy technique. Gastrointestinal Endoscopy 2006; 63(2):257-261.

10. Shao X, Zheng W, Huang Z. In vivo diagnosis of colonic precancer and cancer using near-infrared autofluorescence spectroscopy and biochemical modeling. Journal of Biomedical Optics 2011; 16(6):067005-067005-067008.

11. Nallala J, Gobinet C, Diebold M-D, Untereiner V, Bouché O, Manfait M, Sockalingum GD, Piot O. Infrared spectral imaging as a novel approach for histopatho-logical recognition in colon cancer diagnosis. Journal of Biomedical Optics 2012; 17(11):116013-116013.

12. Farrell TJ, Patterson MS, Wilson B. A diffusion theory model of spatially resolved, steady-state diffuse reflectance for the noninvasive determination of tissue optical properties invivo. Medical physics 1992; 19(4):879-888.

13. Nachabé R, Hendriks BH, van der Voort M, Desjardins AE, Sterenborg HJ. Estimation of biological chromophores using diffuse optical spectroscopy: benefit of extending the UV-VIS wavelength range to include 1000 to 1600 nm. Biomedical optics express 2010; 1(5):1432-1442.

14. Nachabé R, Sterenborg HJ, Hendriks BH, Desjardins AE, van der Voort M, van der Mark MB. Estimation of lipid and water concentrations in scattering media with diffuse optical spectroscopy from 900to1600nm. Journal of Biomedical Optics 2010; 15(3):037015-037015-037010.

15. Müller M, Hendriks BH. Recovering intrinsic fluorescence by Monte Carlo modeling. Journal of Biomedical Optics 2013; 18(2):027009-027009.

16. Müller MG, Georgakoudi I, Zhang Q, Wu J, Feld MS. Intrinsic fluorescence spectroscopy in turbid media: disentangling effects of scattering and absorption. Applied Optics 2001; 40(25):4633-4646.

17. Moesta KT, Ebert B, Handke T, Nolte D, Nowak C, Haensch WE, Pandey RK, Dougherty TJ, Rinneberg H, Schlag PM. Protoporphyrin IX occurs naturally in colorectal cancers and their metastases. Cancer research 2001; 61(3):991-999.

18. Kemmner W, Wan K, Rüttinger S, Ebert B, Macdonald R, Klamm U, Moesta KT. Silencing of human ferrochelatase causes abundant protoporphyrin-IX accumulation in colon cancer. The FASEB Journal 2008; 22(2):500-509.

19. Li B-H, Xie S-S. Autofluorescence excitation-emission matrices for diagnosis of colonic cancer. World journal of gastroenterology 2005; 11(25):3931.

20. Polo C, Frisardi A, Resnik E, Schoua A, Batlle A. Factors influencing fluorescence spectra of free porphyrins. Clinical chemistry 1988; 34(4):757-760.

21. Breiman L. Classification and regression trees: CRC press. 1993.

22. Croce AC, Santamaria G, De Simone U, Lucchini F, Freitas I, Bottiroli G. Naturally-occurring porphyrins in a spontaneous-tumor bearing mouse model. Photochemical & Photobiological Sciences 2011; 10(7):1189-1195.

23. Ma L, Dolphin D. The metabolites of dietary chlorophylls. Phytochemistry 1999; 50(2):195-202.

24. Schols RM, Dunias P, Wieringa FP, Stassen LP. Multispectral characterization of tissues encountered during laparoscopic colorectal surgery. Medical engineering & physics 2013; 35(7):1044-1050.

25. Arimoto H, Egawa M, Yamada Y. Depth profile of diffuse reflectance near-infrared spectroscopy for measurement of water content in skin. Skin Research and Technology 2005; 11(1):27-35.
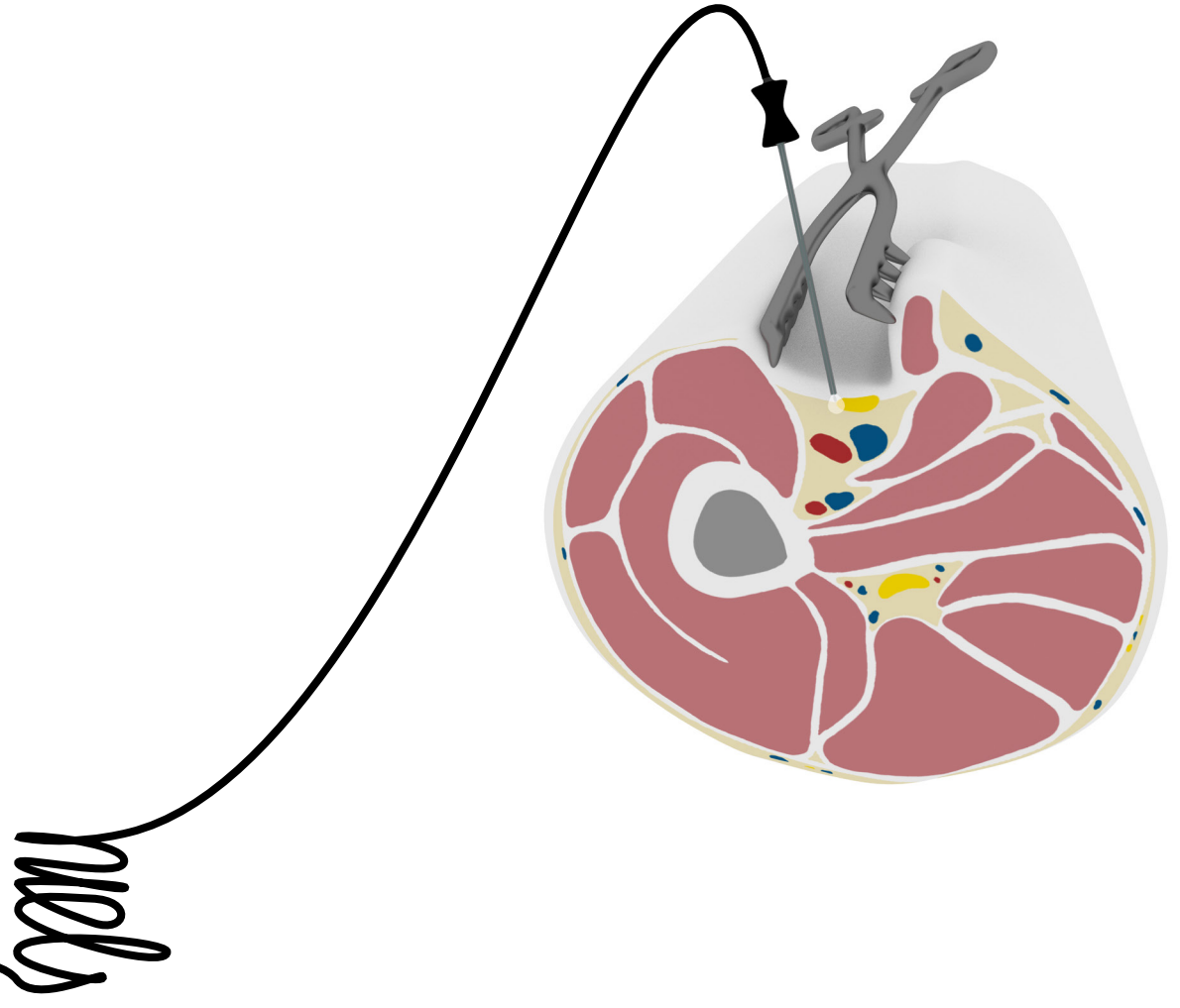
4

Nerve detection during surgery: Optical spectroscopy for peripheral nerve localization

Precise nerve localization is of major importance in both surgery and regional anesthesia. Optically based techniques can identify tissue through differences in optical properties, like absorption and scattering. The aim of this study was to evaluate the potential of optical spectroscopy (diffuse reflectance spectroscopy) for clinical nerve identification in vivo.

Eighteen patients (8 male, 10 female, age 53 ± 13 years) undergoing inguinal lymph node resection or resection or a soft tissue tumor in the groin were included to measure the femoral or sciatic nerve and the surrounding tissues. In vivo optical measurements were performed using Diffuse Reflectance Spectroscopy (400–1600 nm) on nerve, near nerve adipose tissue, muscle, and subcutaneous fat using a needleshaped probe. Model-based analyses were used to derive verified quantitative parameters as concentrations of optical absorbers and several parameters describing scattering.

A total of 628 optical spectra were recorded. Measured spectra reveal noticeable tissue specific characteristics. Optical absorption of water, fat, and oxy- and deoxyhemoglobin was manifested in the measured spectra. The parameters water and fat content showed significant differences ($P < 0.005$) between nerve and all surrounding tissues. Classification using k-Nearest Neighbor based on the derived parameters revealed a sensitivity of 85 % and a specificity of 79 %, for identifying nerve from surrounding tissues.

Diffuse Reflectance Spectroscopy identifies peripheral nerve bundles. The differences found between tissue groups are assignable to the tissue composition and structure.

G.C. Langhout, K.F.D. Kuhlmann, M.W.J.M. Wouters, J.A. van der Hage, F. van Coevorden, M. Müller, T.M. Bydlon, H.J.C.M. Sterenborg, B.H.W. Hendriks, T.J.M. Ruers

Introduction

Precise nerve localization is of major importance in both surgery and regional anesthesia. Although postoperative neural injury to large nerves is not extremely common, injury to smaller nerves like the parasympathetic nerve fibers in pelvic surgery can lead to disturbances in bladder function and sexual function in up to 30 % of the patients[1,2]. In regional anesthesia, the onset and quality of peripheral nerve blocks rely on the adequate placement of the anesthetics around the nerve. Several techniques have been investigated to facilitate nerve localization, including electrical and mechanical stimulation as well as ultrasound. Still, the success rate of regional anesthesia (complete sensory loss) using these guiding tools is limited to 63 %-81 %[3-6]. Nerve stimulation is often not reliable, even when handled perfectly, as it requires neural conduction and a corresponding muscle response.

Diffuse Reflectance spectroscopy (DRS) is a technique capable of tissue identification, based on differences in optical tissue properties. When the tissue is illuminated through optical fibers in direct contact with the tissue, interaction of the light with tissue results in either absorption or scattering/reflection of the light. As absorption and scattering are tissue specific, illuminating tissue with a selected spectral band of light and subsequent analysis of the characteristic scattering and absorption patterns will result in an ´optical fingerprint´ of the tissue[7]. Analytical models are able to extract biochemical, morphological, and physiological parameters from the measured spectra. In this way, DRS was able to identify nerve tissue in swine[7-9]. In contrast to nerve stimulation, optical spectroscopy does not rely on the effect on innervated muscle fibers and is therefore not hampered when the patient's muscle function is reduced by anesthesia or when targeting sensory nerves or the autonomic nervous system.

The use of optical techniques for the detection of nerve tissue has recently been assessed in humans[10-12]. Post-mortem, in fresh frozen human bodies, nerves were detected with a sensitivity and specificity of around 90 %[12]. The in vivo human study by Balthasar et al[10]. targeted six different nerves and distinguished three types of tissue (subcutaneous fat, muscle, and a combined group of near nerve adipose tissue and nerve) based on two parameters related to lipids and hemoglobin. Balthasar performed transcutaneous measurements using a needle shaped optical stylus. Ultrasound was used as gold standard to determined needle position. Significant differences in parameter values were found between subcutaneous fat, muscle and a region denominated as target region for regional anesthesia[10]. Because no classification was performed, no sensitivity and specificity was presented. Schols et al. used optical spectroscopy in the context of the development of a multispectral camera system. The study compared two types of detectors using optical spectroscopy in vivo in human. Nerve and adipose tissue could be differentiated with accuracies between 67 % and 100 % depending on classification method and sensor type[11]. The aim of the present study was to further investigate the potential of DRS to

discriminate nerve tissue from multiple surrounding tissues in vivo. To test the hypothesis that nerve tissue could be discriminated from multiple surrounding tissue in vivo, we present differences in optical parameter values and perform a formal classification.

Materials and methods

This study was performed at The Netherlands Cancer Institute – Antoni van Leeuwenhoek hospital under approval of the protocol and ethics review board (NL40893.031.12). Written informed consent was obtained from all subjects. Patients undergoing inguinal lymph node dissection or resection of a soft tissue tumor located in the groin were included. Patients were selected based on the likelihood of exposure of the femoral or sciatic nerve. The exclusion of patients is visualized in Figure 5.01.

Instrumentation

Inclusions

21 patients

Exclusions

Logistical restrictions: 1

Limited surgery: 1

Technical failure: 1

Inguinal lymph node dissection 13 patients

Soft tissue tumor resection 5 patients
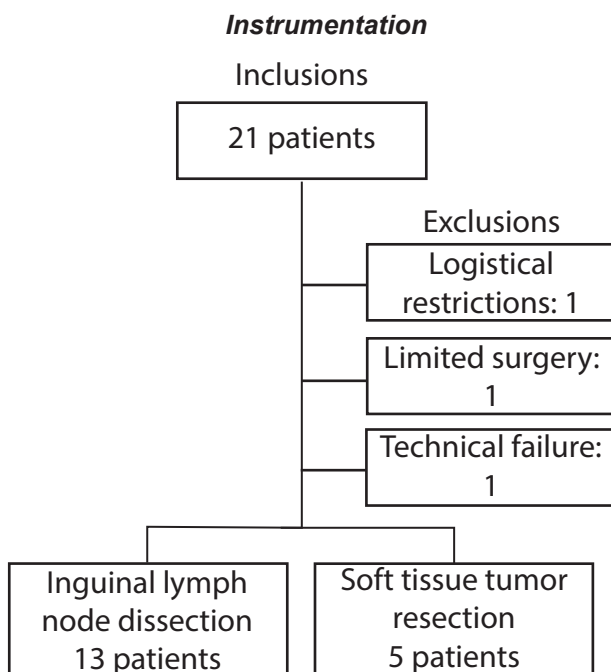
Figure 5.01. | *Three patients were excluded. In two cases no measurements were performed due to logistical problems and unexpected extensive disease leading to conversion to restricted surgery. In one patient, the measurement results were strongly influenced by a separate light source. 18 patients remained, 15 on the femoral nerve, 3 on the sciatic nerve.*

The instrumentation and calibration procedure of our optical spectroscopy system and validation of the quantifications of chromophores has been described elsewhere[13,14]. A sterile probe containing two optical fibers (one illumination fiber and one collecting fiber, type N6, Invivo Germany, Schwerin, Germany) was used to deliver broad spectrum light from a tungsten-halogen source with integrated shutter (AvaLight HAL-S-IND 20W, Avantes, Apeldoorn, The Netherlands). The diffusely reflected light, measured via the

collecting fiber, was analyzed in the range of 400-1600 nm by two spectrometers (400 up to 1100 nm: DU420A-BRDD, 900 up to 1700 nm: DU492A-1.7 Andor Technology, Belfast, Northern Ireland) covering the visible and near-infrared ranges. In the present study, the distance between the illumination and collection fibers was 0.8 mm, the probe diameter at the tip was 1.9 mm. The setup is schematically represented in Figure 5.02. The measurement setup is controlled by a custom-made LabView software interface (LabView, National Instruments, Austin, TX, USA).
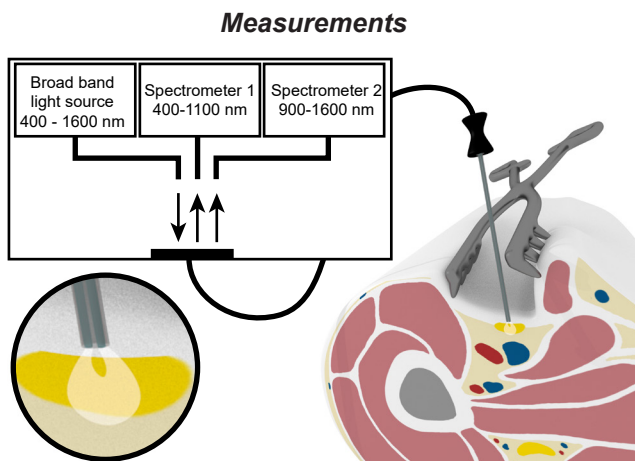
Measurements

Figure 5.02. | Scheme of measurement setup. The leg is visualized as cross-section with the optical probe placed on the femoral nerve. The round inlay shows a close-up of the tip of the probe.

Optical measurements were performed on nerve tissue, near-nerve adipose tissue, skeletal muscle, and subcutaneous fat. To guarantee the correct measurement location and close contact with the tissue of interest, optical measurements were performed under direct vision during open surgery. After exposure of the nerve, the blunt tip of the probe was placed on the nerve tissue by the surgeon. Blood collections were wiped away before the measurements. At each measurement location (on-nerve, near-nerve adipose tissue, skeletal muscle, and subcutaneous fat), repeated measurements were processed and averaged to one measurement per location. During the recording, the surgical lights were dimmed to minimize the influence of environmental light.

Spectral analysis

Tissue interactions with light are categorized as either optical absorption by chromophores or scattering, where scattering is the redirection of light by the particles in tissue. Each biological tissue has intrinsic absorption and scattering properties depending on the wavelength of light. Therefore, a tissue specific spectrum is measured during DRS. A widely accepted model, first described by Farrell et al., was used to quantify parameters related to the physiological, morphological, and metabolic characteristics of the measured

tissue[15]. These parameters include volume fractions or concentrations of the different tissue chromophores and scattering parameters. The implementation of this model in Matlab (Matworks Inc., Natrick, MA, USA) to analyze the diffuse reflectance spectra over a wavelength of 400-1600 nm is described by Nachabé et al[16]. As the model was originally based on large fiber distances (>1.5 mm), overestimation of specific parameters, such as water, fat, β-carotene, and hemoglobin, is inevitable[16]. A correction was applied by dividing these values by the mean of water plus fat content as measured in muscle and subcutaneous fat. Spectra highly contaminated by blood (hemoglobin concentration >20 %) were excluded from the analyses.

Tissue classification and statistics

Tissue was classified according to the k-Nearest Neighbor (knn) principle with k=3. In this test the data is distributed between two sets (training and validation), a measurement is classified as the most common class of 3 measurements with the best comparable values from the training set. Input for the algorithm were parameters derived from the DRS spectra: water content, fat content, β-carotene content, Mie scatter slope, scattering at 800 nm, hemoglobin concentration, and oxygen saturation. Parameters were normalized to a mean value of zero with a standard deviation of one, to give parameters an equal weight. A basic classification was done using a cross-validation method, i.e. subsequently taking out the spectra of one patient as the validation set and using the remaining spectra for training. The result of this classification is an estimation of the sensitivity, specificity, and Matthews correlation coefficient (MCC). This coefficient is used in machine learning as a measure of quality of classifications[17]. A MCC of +1 represents a perfect prediction, −1 indicates total disagreement between prediction and observation.

Results

Eighteen patients (8 male, 10 female) were included, 13 patients were scheduled for inguinal lymph node dissection, and 5 for resection of a soft tissue tumor. Mean age of the patients was 53±13 years. A total of 628 measurements was performed, 295 on nerve, 101 on near- nerve adipose tissue, 124 on muscle, and 108 on subcutaneous fat. Nerve branches were measured ranging from 1 to 13 mm in diameter (5.7±3 mm, mean ± standard deviation). No extensive preparation of the nerves was performed, other than necessary for adequate surgery. All measured nerves were macroscopically identified by the surgeon.

Spectra

An example of an optical measurement is seen in Figure 5.03. The photograph shows the surgical area with the probe positioned on the femoral nerve. Measured spectra (Fig. 5.04) reveal optical characteristics of the investigated tissues. Typical examples of optical

characteristics are the decrease in signal intensity (sharp dip) around 1200 nm due to lipid absorption (recognized in the spectra of subcutaneous fat and near-nerve adipose tissue). Optical absorption by water is recognized by multiple absorption peaks in the (near) infrared range, recognized in the graphs as sharp dips in measured light intensity. The water related absorption peak at 1455 nm is most prominent in the spectra measured on muscle and nerve where the measured intensity is almost zero at 1400-1500 nm. Both oxygenated and deoxygenated hemoglobin were observed in all spectra, seen as a decrease in the signal intensity in the range of 400-600 nm.

Subcutaneous fat
Near nerve

■ Muscle (sartorius)   ■ Femoral artery
■ Femoral nerve   ■ Femoral vein
■ Tissue retractor   □ Optical probe
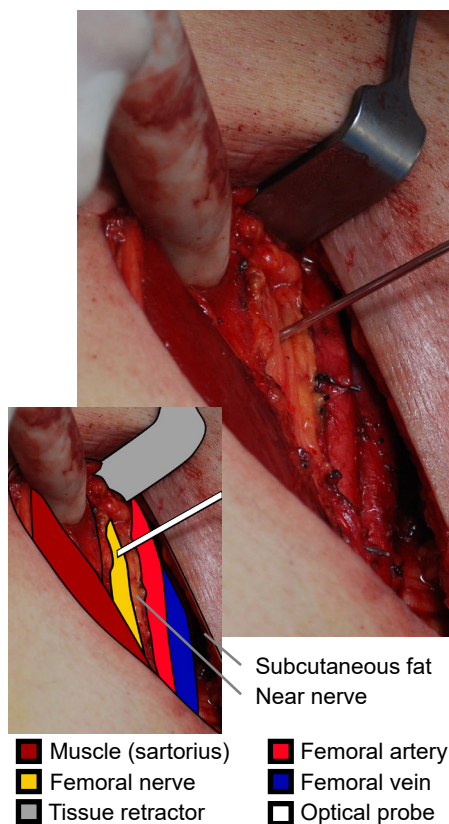
Figure 5.03. | Photograph during a measurement; tissue types are indicated in the photo inlay. The optical probe is positioned on the femoral nerve.

Tissue parameters

Boxplots were generated based on all of the analyzed data (Fig. 5.05). Parameters strongly influenced by the visible part of the spectrum are grouped separately from the parameters derived from the infra-red part of the spectrum. The concentration of water is highest in muscle and low in adipose tissue. The estimated concentration of fat is highest for measurements on subcutaneous fat, followed by near-nerve adipose tissue. Nerve measurements show high fat levels compared to muscle but lower compared to
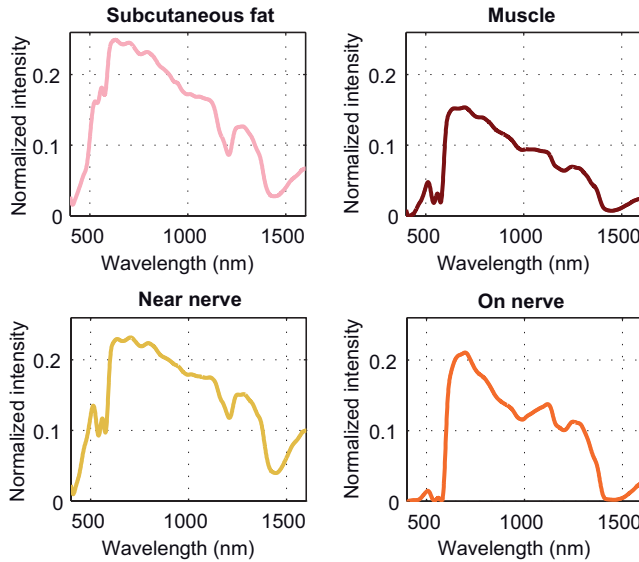
Figure 5.04. | Typical examples of the measured spectra per tissue class, depicted as the normalized intensity of the reflected light as a function of the wavelength.

subcutaneous fat. Fat and water parameters can be combined into the fat fraction (fat/ (fat + water)). The average level of scattering in muscle is significantly lower compared to nerve. Blood levels are highest on muscle and comparable between subcutaneous fat, near-nerve adipose tissue and nerve. The blood saturation and beta-carotene levels are lower in muscle compared to on-nerve measurements.
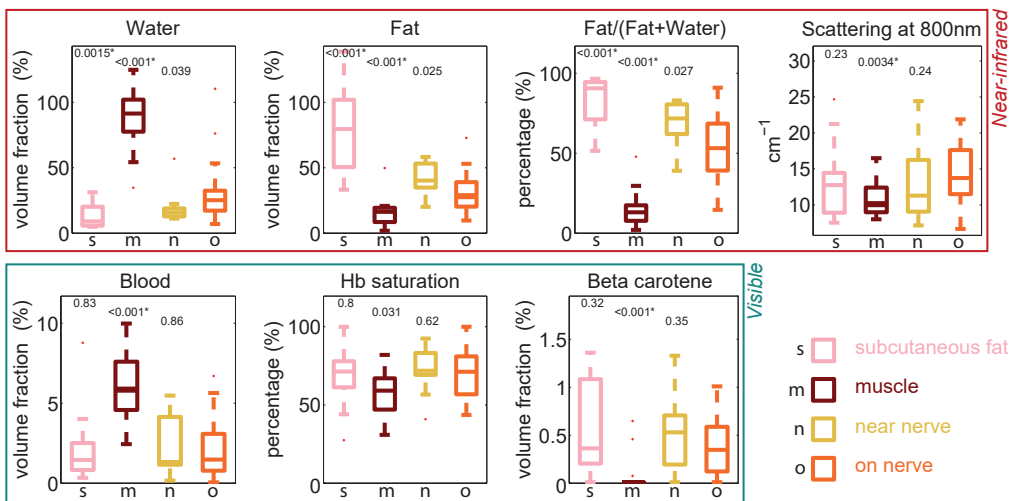
Figure 5.05. | Boxplots of relevant tissue parameters. The significance levels depicted above the bars indicates the difference (p-value) between the tissue and the nerve tissue based on a Mann-Whitney-U test.

Although several parameters show significant differences between tissue groups, optimal tissue identification was based upon the interrelationship of multiple parameters using a classification algorithm. 3-Nearest-neighbourgh classification using a subset of parameters revealed an MCC of 0.64 (values above zero indicate a positive correlation) with a sensitivity of 85 % and a specificity of 79 %. Parameters selected for the subset were the concentrations of hemoglobin and fat, oxygen saturation, fat fraction (fat/ (fat + water)), and two scattering parameters: scattering at 800 nm and the scatter slope. Selection of these parameters was based on the impact on the MCC of all measurements when systematically excluding parameters used in the classification tree.

Discussion

This in vivo human study shows the potential of DRS to identify nerve tissue. Remarkable differences in optical spectra exist between nerve and various surrounding tissues. Within a classification algorithm, the most valuable parameters for nerve tissue discrimination were hemoglobin and fat concentration, fat fraction, oxygen saturation and scattering parameters. Nerve tissue could be detected with a sensitivity and specificity of 85 % and 79 %, respectively. Compared to the results of previous studies, the changes in fat concentration from subcutaneous fat to muscle and nerve is remarkably similar compared to Balthasar[10]. In contrast to Balthasar, we found larger concentrations hemoglobin in nerve compared to subcutaneous fat. Bathasar used a sharp needle with a transcutaneous approach; piercing of the skin might result in bleeding as cause of a higher hemoglobin concentration in subcutaneous fat.

Heterogeneity of nerves and their composition may challenge automatic identification. The morphology and chemical composition differs per nerve (e.g. femoral nerve or sciatic nerve) and even depends on the position on the nerve[18]. An example of the heterogeneity of composition of nerves is the amount of intraneural adipose tissue. This amount varies between nerves and the position on the nerve (proximal or distal)[18]. In small nerve branches, the epineurium is fused with the perineurium, eliminating the space for intraneural adipocytes[19]. In this study, a variety of nerve branches was included. Measurements were performed on nerve branches with diameters ranging from 1 to 13 mm, from two different nerve types. In a specific clinical setting, the target nerve location will be more specified which will limit the variation in nerve diameter, composition and morphology, and hence lower the variability in the optical properties. It is expected that this will enhance the performance of optical nerve identification.

For clinical applications in a defined anatomical region, the probed volume of DRS can be tailored to a specific application. The probed volume is influenced by the distance between the illuminating- and the collecting fiber. When the inter-fiber distance is increased light travels a longer path through the tissue. This leads to an increased probed volume as well

as an increased penetration depth[20]. In a defined anatomical region or a specific clinical application, less variation in the nerve diameter will be encountered thereby allowing a device with the most optimal inter-fiber distance to be selected.

Open surgery was used as gold standard for anatomical identification. After a process with careful preparation and exposure, using the surgeons experience, anatomical knowledge and sight the nerve could be identified with maximum certainty, this applies in particular for the larger nerves selected in this study. The maximum advantage of a nerve identification technique during surgery would be during, or prior to extensive preparation; especially in situations where anatomical relations are distorted, or when visible of tactile feedback is limited. In addition, in the current setting the surface was wiped before the measurements to remove blood collections. However, due to small bleedings, some variability in the blood content may still have been present due to these bleedings. A potential advantage of our method of analyzing the spectra is that the individual chromophores can be quantified separately which increases the robustness of the technique while improving clinical comprehension. For example, in regional anesthesia the nerve is approached with a needle meaning that the tissue is not exposed to air. Our approach may take into account such differences in application by prioritizing the individual parameters. In this case, the oxygen saturation could be left out of the classification algorithm.

The DRS technology, here assembled in a measurement probe, could also be incorporated into needles for regional anesthesia, or surgical instruments. DRS stylets, compatible with a 20-gauge needle cannula were already used in swine and human[8,10]. The diameter of the optical fibers (200 μm) used in the probes for this study could also easily be fitted into surgical dissection tools or needles used for regional anesthesia application.

Conclusion

Optical spectroscopy with the use of DRS allows for identification of nerve tissue based on both differences in clinical comprehensive parameters as well as on formal automated classification. The differences found between tissue groups are assignable to the tissue composition and structure and may be valuable in nerve detection or localization in regional anesthesia or surgical procedures.

Compliance with Ethical Standards

Acknowledgements

References

1. Lange MM, van de Velde CJ Long-term anorectal and urogenital dysfunction after rectal cancer treatment. In: Sem Col Rec Surg, 2010. Elsevier, pp 87-94

2. Celentano V, Fabbrocile G, Luglio G, Antonelli G, Tarquini R, Bucci L (2010) Prospective study of sexual dysfunction in men with rectal cancer: feasibility and results of nerve sparing surgery. Int J Colorectal Dis 25 (12):1441-1445.

3. Urmey WF, Stanton J (2002) Inability to consistently elicit a motor response following sensory paresthesia during interscalene block administration. Anesthesiology 96 (3):552-554.

4. Perlas A, Niazi A, McCartney C, Chan V, Xu D, Abbas S (2006) The sensitivity of motor response to nerve stimulation and paresthesia for nerve localization as evaluated by ultrasound. Region Anesth Pain M 31 (5):445-450.

5. Walker KJ, McGrattan K, Aas-Eng K, Smith AF (2009) Ultrasound guidance for peripheral nerve blockade. Cochrane Db Syst Rev (4):CD006459.

6. Chan VW, Perlas A, McCartney CJ, Brull R, Xu D, Abbas S (2007) Ultrasound guidance improves success rate of axillary brachial plexus block. Can J Anaesth 54 (3):176-182.

7. Brynolf M, Sommer M, Desjardins AE, ..., Söderman M (2011) Optical detection of the brachial plexus for peripheral nerve blocks: An in vivo swine study. Reg Anesth Pain Med 36 (4):350-357.

8. Desjardins AE, Van der Voort M, Roggeveen S, Lucassen G, Bierhoff W, Hendriks BH, Brynolf M, Holmström B (2011) Needle stylet with integrated optical fibers for spectroscopic contrast during peripheral nerve blocks. J Biomed Opt 16 (7):077004.

9. Stelzle F, Knipfer C, Bergauer B, Rohde M, Adler W, Tangermann-Gerk K, Nkenke E, Schmidt M (2014) Optical nerve identification in head and neck surgery after Er: YAG laser ablation. Lasers Med Sci 29 (5):1641-1648.

10. Balthasar A, Desjardins AE, van der Voort M, Lucassen GW, Roggeveen S, Wang K, Bierhoff W, Kessels AG, van Kleef M, Sommer M (2012) Optical detection of peripheral nerves: an in vivo human study. Reg Anesth Pain Med 37 (3):277-282.

11. Schols RM, ter Laan M, Stassen LP, Bouvy ND, Amelink A, Wieringa FP, Alic L (2014) Differentiation between nerve and adipose tissue using wide-band (350–1,830 nm) in vivo diffuse reflectance spectroscopy. Laser Surg Med.

12. Hendriks BH, Balthasar AJ, Lucassen GW, van der Voort M, Mueller M, Pully VV, Bydlon TM, Reich C, van Keersop AT, Kortsmit J (2015) Nerve detection with optical spectroscopy for regional anesthesia procedures. J Trans Med 13 (1):380.

13. Nachabé R, Evers DJ, Hendriks BH, ..., Wesseling J (2011) Diagnosis of breast cancer using diffuse optical spectroscopy from 500 to 1600 nm: comparison of classification methods. J Biomed Opt 16 (8):087010-087012.

14. Nachabé R, Sterenborg HJ, Hendriks BH, Desjardins AE, van der Voort M, van der Mark MB (2010) Estimation of lipid and water concentrations in scattering media with diffuse optical spectroscopy from 900to1600nm. J Biomed Opt 15 (3):037015.

15. Farrell TJ, Patterson MS, Wilson B (1992) A diffusion theory model of spatially resolved, steady-state diffuse reflectance for the noninvasive determination of tissue optical properties in vivo. Med Phys 19 (4):879-888.

16. Nachabé R, Hendriks BH, van der Voort M, Desjardins AE, Sterenborg HJ (2010) Estimation of biological chromophores using diffuse optical spectroscopy: benefit of extending the UV-VIS wavelength range to include 1000 to 1600 nm. Biomed Opt Express 1 (5):1432-1442.

17. Getoor L, Taskar B (2007) Introduction to statistical relational learning. MIT press, London, UK

18. Maravilla KR, Bowen BC (1998) Imaging of the peripheral nervous system: evaluation of peripheral neuropathy and plexopathy. Am J Neuroradiol 19 (6):1011-1023.

19. Brady S, Siegel G, Albers RW, Price D (2007) Basic neurochemistry: molecular, cellular and medical aspects. 7th edn. Elsevier Academic Press, Burlington, USA

20. Arifler D, MacAulay C, Follen M, Richards-Kortum R (2006) Spatially resolved reflectance spectroscopy for diagnosis of cervical precancer: Monte Carlo modeling and comparison to clinical measurements. J Biomed Opt 11 (6):064027.
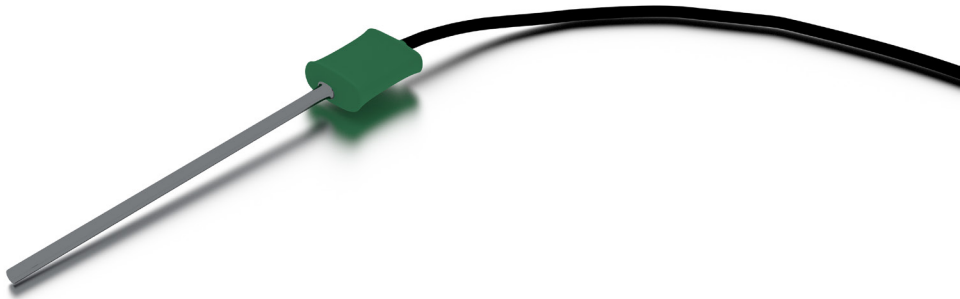
In vivo nerve identification in head and neck surgery using diffuse reflectance spectroscopy

Careful identification of nerves during head and neck surgery is essential to prevent nerve damage. Currently, nerves are identified based on anatomy and appearance, optionally combined with electromyography (EMG). In challenging cases, nerve damage is reported in up to 50 %. Recently, optical techniques, like diffuse reflectance spectroscopy (DRS) and fluorescence spectroscopy (FS) show potential to improve nerve identification.

212 intra-operative DRS/FS measurements were performed. Small nerve branches (1–3 mm), on near-nerve adipose tissue, muscle and subcutaneous fat were measured during 11 surgical procedures. Tissue identification was based on quantified concentrations of optical absorbers and scattering parameters.

Clinically comprehensive parameters showed significant differences (<0.05) between the tissues. Classification using k-Nearest Neighbor resulted in 100 % sensitivity and a specificity of 83 % (accuracy 91 %), for the identification of nerve against surrounding tissues.

DRS/FS is a potentially useful intraoperative tool for identification of nerves from adjacent tissues.

G.C. Langhout, K.F.D. Kuhlmann, P. Schreuder, T. Bydlon, L.E. Smeele,

M.W.M. van den Brekel, J.C.M. Sterenborg, B.H.W. Hendriks, T.J.M. Ruers

Introduction

The identification and preservation of peripheral nerves is essential during head and neck surgery as well as other surgery. Accidental transection or injury can cause severe morbidity including pain, numbness, weakness or paralysis. The incidence of damage to peripheral nerve branches varies. Nerve damage (including temporary neuropraxia) may be up to 50 % for peripheral branches of the facial nerve during parotid surgery[1].

Conventionally, nerves are identified based on their anatomical position and visual appearance. In addition, electromyography (EMG) combined with local stimulation may be used to identify nerve tissue. This technique, however, requires an intact nerve pathway and functioning muscle. Furthermore, EMG identifies only motor pathways, not sensory fibers such as the first two divisions of the trigeminal nerve or the cochleovestibular nerve[2]. In addition, neuromuscular transmissions, and therefore muscle activity, may be hampered by nerve compression, tumor invasion, trauma, or medication. A systematical

review indicates a successful localization of peripheral nerves using nerve stimulation in 80 % (failure in 20 %) of the cases. The review includes 32 RTCs concerning ultrasound and peripheral nerve stimulation guidance for nerve blocks in both upper and lower limbs[3]. In the present paper we describe the use of diffuse reflectance spectroscopy (DRS) combined with fluorescence spectroscopy (FS) for the identification of small peripheral nerves. This optical technique was earlier used to identify various malignancies in breast[4-6], liver[7,8], colon[9,10], cervix[11], and lung[12,13]. In DRS, the tissue is illuminated with broadband white light. Within the tissue the light will be partly absorbed and will undergo scattering, depending on the specific tissue properties of the tissue. These interactions result in a tissue-specific "optical fingerprint" as measured by diffuse reflectance spectroscopy. Additionally, DRS measurements may be accompanied by fluorescence spectroscopy which is able to detect specific intrinsic fluorophores within the tissue such as collagen and elastin as well as tissue metabolism by parameters such as NADH and FAD.

Several studies have demonstrated the potential of optical spectroscopy for identification of peripheral nerves. These studies, however, are often targeting large nerves, as relevant for regional anesthesia[14-17]. Results obtained in swine and humans showed an excellent differentiation (area under the ROC curve, receiver operating characteristic curve, of 0.98) between muscle, fascia, and the targeted region for regional anesthesia. In another study by Schols et al., DRS was used to differentiate between nerve and adipose tissue, showing an accuracy between 67 % and 100 % depending on the validation method and sensor type[16]. Comparable results were described by Hendriks et al., who was able to identify nerve tissue using DRS with a sensitivity and specificity of around 90 % in a post-mortem study in humans[17].

The aim of the current in vivo study is to evaluate whether a combination of diffuse reflectance spectroscopy and fluorescence spectroscopy is able to identify small

nerve branches during operative procedures in head and neck surgery. To this end we compared both the measured spectra as well as the derived optical properties from these spectra to differentiate between nerve tissue, subcutaneous fat, skeletal muscle, and nervesurrounding adipose tissue during head and neck surgery.

The novelty of this study lies in the combination of in vivo human measurements under surgical conditions, the usage of clinical comprehensive parameters for both DRS and FS, and the inclusion of different types of surrounding tissues for the identification of small peripheral nerves.

Material and methods

This study was performed at The Netherlands Cancer Institute–Antoni van Leeuwenhoek under approval of the protocol and ethics review board (NL40893.031.12). Written informed consent was obtained from all subjects. Patients undergoing total parotidectomy, mandibulectomy and partial glossectomy combined with block dissection of cervical lymph nodes and cervical lymph node dissection alone were randomly selected. The surgeries were performed using standard surgical instruments (sharp dissection by scalpel, blunt dissection by scissors/forceps, and coagulation by electrocoagulation). In all patients, the indication for surgery was a malignant tumor in the head and neck region.

Instrumentation

DRS and FS spectra were acquired using a spectroscopy system, described earlier.6 For this study, a measurement probe containing four optical fibers with 200 mm core diameter (Invivo Germany, Schwerin, Germany) was used that delivered broad spectrum light from a tungsten-halogen source (AvaLight HAL-S-IND 20W, Avantes, Apeldoorn, the Netherlands) to the tissue. Two spectrometers (DU420A-BRDD and DU492A-1.7, Andor Technology, Belfast, Northern Ireland) covering the visible- and near-infrared range measured the diffusely reflected light from 400 to 1600 nm. Both sensors are cooled to -40 degrees Celsius during operation. A long-pass filter (BLP01-405R, Semrock, Rochester, New York, USA) prevented the recording of scattered laser (excitation) light during fluorescence excitation. Separate fibers with an intermediate distance of 0.8mm were used as emitting and collecting fibers. A fiber splitter was used to distribute the collected light to the two spectrometers. FS measurements were performed milliseconds after the DRS acquisition, creating the aspect of a single measurement. For FS, the system was equipped with a semiconductor laser (377 nm, 0.4 mW, NDU113E, Nichia, Tokyo, Japan) to induce auto fluorescence. A schematic representation of the setup is shown in Figure 6.01. The details of the setup and the corresponding calibration procedures are extensively discussed by Nachabe et al[18]. The measurement setup is controlled by custom made LabView software (National Instruments, Austin, Texas, USA).

Broadband Halogen source
Semiconductor laser (377 nm) ▶

Spectrometer (400-1100 nm) ◀
Spectrometer (900-1600 nm)

Fiber connected to
halogen light source

Fiber connected to
semiconductor laser

Fiber connected to
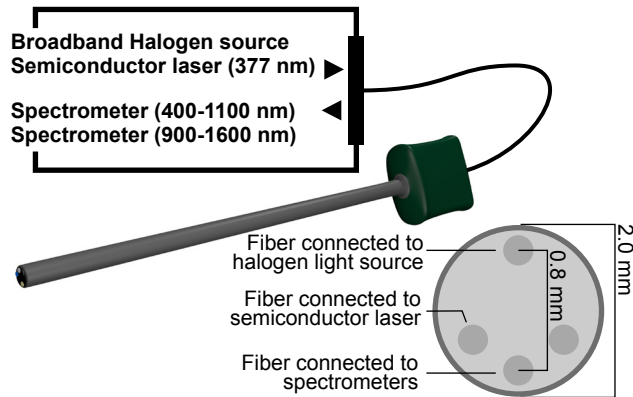spectrometers

2.0 mm
0.8 mm

Figure 6.01. | Representation of the setup. The tissue is illuminated with broadband white light and laser light through separate optical fibers. A fiber splitter connected to the collecting fiber distributes the reflected light over the spectrometers. One fiber is not used and covered at the connector.

Optical measurements

Optical measurements were performed after surgical exposure of the nerve. Routine hemostasis was pursued and optical measurements were performed by placing the probe directly on the tissue of interest. During the measurement, the surgical lights were dimmed to minimize the influence of environmental light. A combined measurement (DRS and FS) was recorded within one second.

Four tissue groups were measured including subcutaneous fat, skeletal muscle, near-nerve adipose tissue, and nerve. Near-nerve adipose tissue is the adipose tissue surrounding several nerve branches. The nerve branch itself is not part of the tissue type. Depending on the availability of exposed nerves, measurements were performed on the greater auricular nerve (branch of the cervical plexus composed of branches of spinal nerves C2 and C3), the spinal accessory nerve (CN XI), or the facial nerve (CN VII). The diameter of the nerve branches varied from 1 to 3 mm. All optical measurements were acquired on unique locations.

Spectral analysis

A widely accepted mathematical model first described by Farrell et al. was used to translate the measured spectra into absorption and scattering coefficients[19]. The absorption coefficients represent the concentration of physiologically relevant absorbers in the tissue, such as hemoglobin, water and fat (lipids), as well as functional parameters like oxygen saturation[20]. The main scattering parameters are the reduced scattering coefficient (at 800 nm), the reduced scattering slope of the Mie scattering (Mie-scattering slope), and the Mie-to-total scattering fraction[21]. The Mie-scattering slope is related to the average particle size[22]. The implementation of this model to analyze diffuse reflectance spectra over a wavelength of 400 to 1600 nm measured with the current setup is described by Nachabe[23]. Application of this model is described in various preclinical and clinical

models[7,9,24–26]. Spectra highly contaminated by blood (>25 %) were excluded from analysis. For FS, autofluorescence was calculated by correcting the measured fluorescence spectra for absorption and scattering using a method described earlier[27,28]. The model was implemented according to Müller[27] based on a modified photomigration model[28]. The corrected spectra were fitted using the intrinsic fluorescence spectra (excitation at 377 nm) of collagen, elastin, NADH, and FAD as a priori knowledge. A Mann–Whitney U test was used to compare the measurements of surrounding tissue with on-nerve. A P value <0.05 indicates a significant difference between the two groups.

Tissue classification and statistics

The classification algorithm and statistics were conducted in Matlab (Matworks Inc., Natrick, Massachusetts, USA). Tissue was classified according to the k-Nearest Neighbors (knn) principle with k=3. In this test, tissue was assigned to the class of the majority of the three nearest measurements from a training set. The training and validation sets were composed using leave-one-out cross-validation, ie, subsequently taking out the spectra of one patient as the validation set and using the remaining spectra for training. Input for the algorithm were the parameters derived from the DRS and FS spectra: water, fat, blood, b-carotene, methemoglobin and collagen concentration, fat fraction (fat/(water+fat)), hemoglobin oxygen saturation, mie scatter slope, scattering at 800 nm, total fluorescence signal, and FAD concentration. Parameters were normalized to a mean value of 0 with a standard deviation of 1, to give parameters an equal weight. This classification was repeated after omitting the parameters derived from fluorescence to determine the contribution of fluorescence to the classification.

The estimation of clinical comprehensive parameters from the spectra is a form of feature reduction. This approach gives insight in the composition of the tissue and helps to understand the measurement analysis, since results can be directly linked to well-known clinical tissue characteristics. However spectral information might be lost during the feature reduction. For this reason we also used principal component analysis (PCA) with 20 components as an alternative method of feature reduction.

The result of these classifications is an estimation of the sensitivity, specificity and Matthews correlation coefficient (MCC). This coefficient is used in machine learning as a measure of quality of classifications[29]. A MCC of 11 represents a perfect prediction; -1 indicates total disagreement between prediction and observation.

Results

Patient characteristics

Eleven patients were included (age 63±9 years): six males and five females. None of the patients had received neoadjuvant radio/chemo therapy. Five of the surgical procedures were mandibulectomy and partial glossectomy including block dissection of cervical lymph nodes, four patients underwent a cervical lymph node dissection alone, and in two patients a parotidectomy.

Tissue spectra

Two hundred twelve optical measurements were performed: 42 on subcutaneous fat, 47 on muscle, 22 on near-nerve adipose tissue, and 101 on the nerve directly. An example of measured DRS and FS spectra is visualized in Figure 6.02. In the DRS spectra, the first segment (400-650 nm) is dominated by optical absorption of hemoglobin, myoglobin, and, to a lesser extent, beta-carotene. In this spectral region, muscle shows little intensity, indicating relatively high amounts of hemoglobin and myoglobin. Subcutaneous fat, near-nerve adipose tissue, and nerve measurements show a clear double dip between 500 and 600 nm, indicating the presence of oxyhemoglobin. The resemblance of nerve and subcutaneous fat in the spectral range of 400 to 650 nm is in accordance with the comparable levels of hemoglobin/myoglobin and betacarotene in Figure 6.03. After 600 nm, the signal generally increases due to the so called "optical window": a wavelength region in which optical absorption in most tissue is relatively low. The near infrared part of the spectrum is dominated by optical absorption of water and fat. Water shows a characteristic local reduction in optical absorption at 1000 to 1160 nm, recognized as an intensity peak in the spectra measured on muscle and nerve indicated by a gray ellipse in Figure 6.02. A characteristicly sharp intensity dip around 1200 nm due to high lipid concentration is appreciable in the spectra measured on subcutaneous fat and near-nerve tissue. The difference between near-nerve and on-nerve tissue is far more distinct in the infrared part of the spectrum, a wavelength region invisible for the human eye. Examples of these differences are the sharp dip at ~1200 nm and the increase in intensity after 1450 nm in the near-nerve spectrum compared to the on-nerve spectrum. In the fluorescence spectra, the difference in area under the curve between the tissue groups is most notable. Muscle measured a remarkably low fluorescence signal. Fluorescence intensity is influenced by the presence of fluorescent molecules as well as the absorption of the excitation/emission photons; the low fluorescence signal in muscle may be explained by strong optical absorption of the excitation or emission photons due to the large amount of myoglobin. Furthermore, the typical absorption of hemoglobin between 500 to 650 nm is also noticeable in the fluorescence spectra of the other tissue types.
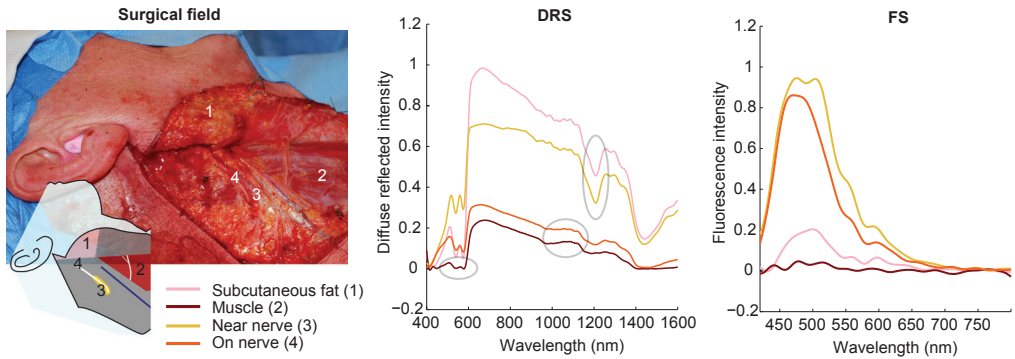
Figure 6.02. | DRS and FS measured spectra with the corresponding measurement locations. The schematic inlay indicates the locations marked by numbers related to the legend of the spectra. In the DRS spectrum, spectral characteristics of hemoglobin (left), water (middle) and fat (right) are depicted with a gray ellipse. The fluorescence spectra are not normalized nor corrected for absorption, to display the differences in fluorescence intensity.

Tissue parameter quantification

Clinically comprehensive parameters, derived from the measured spectra are visualized in boxplots (Fig. 6.03). Parameters related to blood: hemoglobin/myoglobin concentration and the oxygen saturation are grouped in the first column. The optical absorbers fat fraction and betacarotene are shown in the second column. Scattering parameters are grouped in the third column, two parameters derived from the fluorescence spectra (collagen and
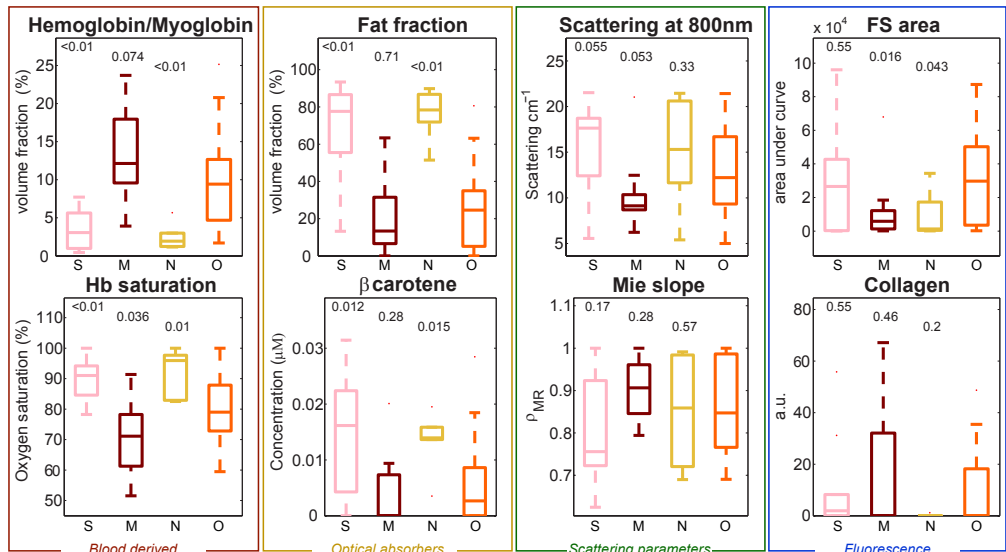
Figure 6.03. | Boxplots of relevant parameters. Above the bars, the significance levels (p-values) are mentioned for the difference between the average values for the nerve and the specific tissue group, based on a Mann-Whitney-U test.

FS area, the latter being the total fluorescence intensity over the measured wavelengths) form the last column. Adipose tissue (subcutaneous fat and near-nerve) is characterized by high measured lipid and beta-carotene concentrations, but are also high in oxygen saturation and low in hemoglobin. Differences in nerve and muscle ($P<0.05$) could be found in oxygen saturation and fluorescence area. When comparing nerve with adipose tissue (subcutaneous fat and near-nerve), significant differences were found in blood content and fat fraction with nerve containing more blood compared to adipose tissue and less fat. Both near-nerve and subcutaneous fat contain significantly more beta-carotene compared to nerve. Although not significant, reasonable amounts of collagen were only found in muscle and nerve.

Tissue classification.

Automated tissue identification using knn classification revealed a MCC of 0.83; positive values (0-1) indicate a positive correlation. Classification showed a sensitivity for nerve identification of 100 %, a specificity of 83 %, and accuracy 91 %. Parameters used in the classification were the amounts of fat and water, fat fraction, hemoglobin, oxygen saturation, Mie scattering and scattering at 800 nm, and total fluorescence intensity. These parameters were selected based on the impact on the MCC by systematically excluding specific parameters from the classification.

All parameters selected were derived from the DRS measurements, except fluorescence intensity. Because of measuring time and the technical requirements for fluorescence measurements, it could be beneficial to discard the fluorescence approach. Classification without the fluorescence parameters resulted in a lower MCC of 0.74 with a sensitivity of 88 %, specificity of 86 %, and an accuracy of 87 %. When using PCA on the DRS spectrum only, the 3-knn classification resulted in a MCC of 0.71 with sensitivity 88 % and specificity 83 %. With the total fluorescence added as extra component, the MCC climbed to 0.78 with a sensitivity of 92 % and a specificity of 86 %.

Discussion

This human in vivo study shows the potential of DRS/FS to identify nerve branches and to differentiate them from various surrounding tissue based on tissue specific optical properties. Nerve branches could be detected with a sensitivity of 100 % and specificity of 83 % (accuracy 91 %). For a reliable estimation of the potential of the technique, it is important to include all tissue classes in the classification analysis that may cover nerve tissue. Four tissue types were included in this study, subcutaneous fat, muscle, near-nerve adipose tissue and nerve. In some cases, nerves are surrounded by bone. As bone could be identified based on visual appearance and consistency, bone was not included in this study. Tissue specific to a unique anatomical location, like parotid glandular tissue could be evaluated in future research.

Our results are in agreement with other studies that focus on peripheral nerve identification using DRS. Schols et al. targeted the recurrent laryngeal nerve to select spectral features of nerve tissue[16]. In the study, 36 parameters based directly on the measured spectrum (eg, gradients) were selected. The number of measurements was limited to 10 unique locations on-nerve and 5 unique locations on adipose tissue. They reported an accuracy of 67 % to 100 % depending on the sensor type and classification method. In a human post-mortem study by Hendriks, the cervical nerves with a circular shaped cross section and a diameter ca. 3 mm were targeted[30]. Multiple classification methods were used to distinguish nerve from surrounding tissue. A MCC ranging from 0.62 to 0.83 was achieved using a Classification and Regression Tree (CART) and Support Vector Machine (SVM) method, respectively. The SVM results showed a sensitivity of 91 %, a specificity of 91 % and accuracy 91 %.

In the present study, physiological fit parameters were used, which translate the measured spectrum into comprehensive clinical parameters. Examples are concentrations of water, fat, beta-carotene and hemoglobin, oxygen saturation, and scattering. An advantage of this approach is that in the clinical setting, the value of each independent comprehensive parameter can be interpreted by the user, before or after the classification. For example, in a particular clinical context where the amount of blood shows significant variation between measurements, independently from tissue type, the blood parameter can be discarded from the classification algorithm. A potential drawback of our approach is that the information of the spectra that contain hundreds of data points per measurement is reduced to a limited number of parameters, and therefore information may be lost. Clinically comprehensive parameters were used to achieve maximum insight, although this method may not deliver optimal accuracies. Feature reduction using PCA, as an alternative for parameter fitting, was performed to estimate a possible negative effect on the classification outcome. Comparable classification results were obtained from the fit parameter analysis and the PCA analysis (MCC 0.83 vs. 0.78). These results are in line with a comparison between various methods for feature reduction as described earlier[31]. In this study, no prior database of tissue measurements was used; classification was done after collecting the entire dataset. Duration of the classification during this study is not an indication for the intended intra-operative use. Although a tissue classification within seconds is expected, future research should demonstrate the total duration from acquisition to classification. We observed that with small nerves, the probing volume of the light may include some underlying tissue which could impact the ability to differentiate nerves from surrounding tissues. The nerves measured in this study included the greater auricular nerve, the spinal accessory nerve, and the facial nerve, all measuring 1 to 3mm and often located in close relation with muscle. Inclusion of some muscle tissue in the probing volume of the nerve measurements explains the similarities in the box plots (Fig. 6.03) between nerve and muscle tissue which were more distinct in earlier post-mortem nerve and muscle measurements[30]. It should be noted that the measurement volume in DRS is influenced by the distance between the illuminating and the collecting fibers.

When the inter-fiber distance is increased light travels a longer path through the tissue.This leads to an increased probed volume as well as an increased penetration depth meaning that for small nerves underlying tissue may be measured as well[31]. For small nerves, like in the present study, the probe volume should be small to prevent such influence from underlying tissues. The penetration depth and therefore the probed volume depends on the optical absorption and scattering of the tissue of interest. As both absorption and scattering vary with the wavelength of the incident light, the penetration depth theoretically depends on the wavelength. This means that optical parameters derived from wavelength regions with high tissue absorption (eg, 400–600 nm and 1200–1700 nm) hold more information about the superficial layers (<2 mm) compared to wavelength regions with less absorption and scattering (eg, 650–1200 nm). The addition of fluorescence spectroscopy requires an alternative light source, typically a semiconductor laser and an extra set of filters, as well as extra measurement time. Our results show, however, that omitting fluorescence may impact accuracy. Classification accuracy dropped from 91 % to 87 % when discarding the fluorescence parameter.

For this study, we selected nerves that are commonly exposed in head and neck surgery and are at risk of iatrogenic nerve damage. The extensive and careful preparation of the nerves makes this environment preeminently suited for both validation and application of advanced intra-operative nerve identifying techniques. Translation of the results found in open surgery to other applications such as percutaneous nerve identification for anesthetic purposes must be done with caution. Important parameters like oxygen saturation or the presence of blood are probably influenced by tissue preparation during surgery, as may be the exposure to air during the procedure. In this study, optical measurements highly contaminated with blood were excluded. Hemoglobin, and therefore blood, is a strong optical absorber especially in the lower part of the spectrum (400–650 nm). The influence of high amounts of blood could overshadow spectral characteristics of the tissue types. In future research, after identification of distinctive spectral characteristics, the classification method should be tested in various situations. Nevertheless, the influence of hemoglobin on the larger wavelength part of the spectrum (>900 nm) is a lot less significant; spectral characteristics in this part of the spectrum are very likely to resist the influence of contamination by hemoglobin. The optical technique in the present study was incorporated into a measurement probe, which allows variation in operator use like applied pressure and measurement angle, which may lead to extra variability in the measurements[32]. When incorporated into a surgical tool, variations in angle and pressure could be minimized to improve the robustness of the technique. Measurements were performed in a controlled environment with measurement locations on carefully identified tissue. Larger clinical studies are necessary to develop a robust algorithm for nerve classification. Furthermore technical development should be initiated to make the technology applicable for routine clinical use. DRS/FS as presented here can be incorporated into smart optical devices with embedded fiber optics allowing real-time identification of tissue during surgery. Examples are presented for regional anesthesia and percutaneous tumor biopsy[15,33]. The exact

nature of such a device for surgical guidance needs, however, further consideration.

Conclusion

In this in vivo pilot study, small peripheral nerves and surrounding tissue were identified, based on clinically comprehensive parameters derived from the measured spectra. This study clearly shows the potential of DRS/FS for tissue identification with regard to periph eral nerves.

6

References

1.   Stelzle F, Zam A, Adler W, et al. Optical nerve detection by diffuse reflectance spectroscopy for feedback controlled oral and maxillofacial laser surgery. Journal of translational medicine 2011;9(1):20.

2.   Whitney MA, Crisp JL, Nguyen LT, et al. Fluorescent peptides highlight peripheral nerves during surgery in mice. Nature biotechnology 2011;29(4):352-356.

3.   Lewis SR, Price A, Walker KJ, McGrattan K, Smith AF. Ultrasound guidance for upper and lower limb blocks. The Cochrane Library.

4.   Brown JQ, Bydlon TM, Richards LM, et al. Optical assesssment of tumor resection margins in the breast. Selected Topics in Quantum Electronics, IEEE Journal of 2010;16(3):530-544.

5.   de Boer L, Molenkamp B, Bydlon T, et al. Fat/water ratios measured with diffuse reflectance spectroscopy to detect breast tumor boundaries. Breast cancer research and treatment 2015;152(3):509-518.

6.   Nachabé R, Evers DJ, Hendriks BH, et al. Diagnosis of breast cancer using diffuse optical spectroscopy from 500 to 1600 nm: comparison of classification methods. J Biomed Opt 2011;16(8):087010-087012.

7.   Evers D, Nachabe R, Hompes D, et al. Optical sensing for tumor detection in the liver. European Journal of Surgical Oncology (EJSO) 2013;39(1):68-75.

8.   Tanis E, Spliethoff J, Evers D, et al. Real-time in vivo assessment of radiofrequency ablation of human colorectal liver metastases using diffuse reflectance spectroscopy. European Journal of Surgical Oncology (EJSO) 2016;42(2):251-259.

9.   Langhout GC, Spliethoff JW, Schmitz SJ, et al. Differentiation of healthy and malignant tissue in colon cancer patients using optical spectroscopy: A tool for image-guided surgery. Laser Surg Med 2015;47(7):559-565.

10.   Schols RM, Dunias P, Wieringa FP, Stassen LP. Multispectral characterization of tissues encountered during laparoscopic colorectal surgery. Med Eng Phys 2013;35(7):1044-50.

11.   Chang VT-C, Bean SM, Cartwright PS, Ramanujam N. Visible light optical spectroscopy is sensitive to neovascularization in the dysplastic cervix. Journal of Biomedical Optics 2010;15(5):057006-057006-9.

12.   Bard MP, Amelink A, Skurichina M, et al. Optical spectroscopy for the classification of malignant lesions of the bronchial tree. Chest 2006;129(4):995-1001.

13.   Evers DJ, Nachabé R, Klomp HM, et al. Diffuse reflectance spectroscopy: a new guidance tool for improvement of biopsy procedures in lung malignancies. Clinical lung cancer 2012;13(6):424-431.

14.   Brynolf M, Sommer M, Desjardins AE, et al. Optical detection of the brachial plexus for peripheral nerve blocks: An in vivo swine study. Reg Anesth Pain Med 2011;36(4):350-357.

15.   Balthasar A, Desjardins AE, van der Voort M, et al. Optical detection of peripheral nerves: an in vivo human study. Region Anesth Pain M 2012;37(3):277-82.

16.   Schols RM, ter Laan M, Stassen LP, et al. Differentiation between nerve and adipose tissue using wide□band (350–1,830 nm) in vivo diffuse reflectance spectroscopy. Lasers in surgery and medicine 2014;46(7):538-545.

17.   Hendriks BH, Balthasar AJ, Lucassen GW, et al. Nerve detection with optical spectroscopy for regional anesthesia procedures. Journal of translational medicine 2015;13(1):380.

18.   Nachabé R, Sterenborg HJ, Hendriks BH, Desjardins AE, van der Voort M, van der Mark MB. Estimation of lipid and water concentrations in scattering media with diffuse optical spectroscopy from 900to1600nm. J Biomed Opt 2010;15(3):037015.

19.   Farrell TJ, Patterson MS, Wilson B. A diffusion theory model of spatially resolved, steady-state diffuse reflectance for the noninvasive determination of tissue optical properties in vivo. Medical physics 1992;19:879.

20.   Doornbos R, Lang R, Aalders M, Cross F, Sterenborg H. The determination of in vivo human tissue optical properties and absolute chromophore concentrations using spatially resolved steady-state diffuse reflectance spectroscopy. Physics in medicine and

biology 1999;44(4):967.

21.   Spliethoff JW, Evers DJ, Jaspers JE, Hendriks BH, Rottenberg S, Ruers TJ. Monitoring of tumor response to Cisplatin using optical spectroscopy. Translational oncology 2014;7(2):230-239.

22.   Zonios G, Dimou A. Light scattering spectroscopy of human skin in vivo. Optics Express 2009;17(3):1256-1267.

23.   Nachabé R, Hendriks BH, van der Voort M, Desjardins AE, Sterenborg HJ. Estimation of biological chromophores using diffuse optical spectroscopy: benefit of extending the UV-VIS wavelength range to include 1000 to 1600 nm. Biomedical optics express 2010;1(5):1432-1442.

24.   Nachabé R, Hendriks BH, Desjardins AE, van der Voort M, van der Mark MB, Sterenborg HJ. Estimation of lipid and water concentrations in scattering media with diffuse optical spectroscopy from 900to1600nm. J Biomed Opt 2010;15(3):037015-037015-10.

25.   Spliethoff JW, Evers DJ, Klomp HM, et al. Improved identification of peripheral lung tumors by using diffuse reflectance and fluorescence spectroscopy. Lung cancer 2013;80(2):165-171.

26.   de Boer LL, Hendriks BH, van Duijnhoven F, et al. Using DRS during breast conserving surgery: identifying robust optical parameters and influence of inter-patient variation. Biomedical optics express 2016;7(12):5188-5200.

27.   Müller M, Hendriks BH. Recovering intrinsic fluorescence by Monte Carlo modeling. J Biomed Opt 2013;18(2):027009-027009.

28.   Müller MG, Georgakoudi I, Zhang Q, Wu J, Feld MS. Intrinsic fluorescence spectroscopy in turbid media: disentangling effects of scattering and absorption. Applied Optics 2001;40(25):4633-4646.

29.   Powers DM. Evaluation: from precision, recall and F-measure to ROC, informedness, markedness and correlation. Journal of Machine Learning Technologies 2011;2(1):37-63.

30.   Hendriks BH, Balthasar AJ, Lucassen GW, et al. Nerve detection with optical spectroscopy for regional anesthesia procedures. J Transl Med 2015;13(1):380.

31.   Arifler D, MacAulay C, Follen M, Richards-Kortum R. Spatially resolved reflectance spectroscopy for diagnosis of cervical precancer: Monte Carlo modeling and comparison to clinical measurements. J Biomed Opt 2006;11(6):064027.

32.   Chang VT-C, Merisier D, Yu B, Walmer DK, Ramanujam N. Towards a field-compatible optical spectroscopic device for cervical cancer screening in resource-limited settings: effects of calibration and pressure. Optics Express 2011;19(19):17908-17924.

33.   Spliethoff JW, Prevoo W, Meier MA, et al. Real-time in vivo tissue characterization with diffuse reflectance spectroscopy during transthoracic lung biopsy: a clinical feasibility study. Clinical cancer research 2016;22(2):357-365.

6

Nerve detection using optical spectroscopy, an evaluation in four different settings: in human and swine, in-vivo and post mortem

Identification of peripheral nerve tissue is crucial in both surgery and regional anesthesia. Recently, optical tissue identification methods are presented to facilitate nerve identification in transcutaneous procedures and surgery. Optimization and validation of such techniques require large datasets. The use of alternative models to human in vivo, like human post mortem, or swine may be suitable to test, optimize and validate new optical techniques. However, differences in tissue characteristics and thus optical properties, like oxygen saturation and tissue perfusion are to be expected. This requires a structured comparison between the models.

Nerve and surrounding tissues in human (in vivo and post mortem) and swine (in vivo and post mortem) were structurally compared macroscopically, histologically and spectroscopically. Diffuse reflective spectra were acquired (400-1600 nm) after illumination with a broad band halogen light. An analytical model was used to quantify optical parameters including concentrations of optical absorbers.

Several differences were found histologically and in the optical parameters. Histologically nerve and adipose tissue (subcutaneous fat and sliding fat) showed clear similarities between human and swine while human muscle enclosed more adipocytes and endomysial collagen. Optical parameters revealed model dependent differences in concentrations of β-carotene , water, fat, and oxygen saturation. The similarity between optical parameters is however sufficient to yield a strong positive correlation after cross model classification.

This study shows and discusses similarities and differences in nerve and surrounding tissues between human in vivo and post mortem, and swine in vivo and post mortem; this could support the discussion to use an alternative model to optimize and validate optical techniques for clinical nerve identification.

Lasers in Surgery and Medicine

G.C. Langhout, T.M. Bydlon, M, van der Voort, M. Müller, J. Kortsmit, G. Lucassen, A.J.R. Bal-

thasar, G-J van Geffen, T. Steinfeldt, H.J.C.M. Sterenborg, B.H.W. Hendriks, T.J.M. Ruers

Introduction

Identification of peripheral nerves is crucial in both surgery and regional anesthesia. During surgery, nerves have to be identified and spared to prevent morbidity including pain, numbness, weakness and paralysis. For regional anesthesia, real time feedback of the tissue type at the tip of a needle may improve accurate deposition of the analgesic and therefore improve the quality and onset of a nerve block.

Nerve identification techniques currently being used, like nerve elicitation of motor response or paresthesia, have low sensitivities (30 %-70 % for electrical stimulation and 40 % for mechanical stimulation[1,2]) which indicate the clear need for more reliable techniques. Diffuse reflectance spectroscopy (DRS) is an optical technique which can characterize tissue based on differences in the optical absorption and scattering properties. In DRS, tissue is illuminated with a broad spectral light and the diffusely reflected light is measured. Each biological tissue has its intrinsic absorption and scattering properties which directly influence the reflected light that will be measured. Based on the measured spectrum, optical absorbers like hemoglobin, water, lipids and β-carotene can be quantified. Both the quantified absorbers and the scattering parameters are used for further tissue identification. A number of studies show the potential of nerve identification using diffuse reflectance spectroscopy[3-8]. Two in vivo human studies are published but both were performed with a small number of measurements[6,8]. Optimization of the technique for in vivo human clearly demands validation on a large study population. Tissue classification algorithms utilized with optical spectroscopy data often rely on principal component analysis[9], classification and regression trees[10,11], or K- nearest neighbor principle[5]. A large number of measurements in the training sets of these algorithms will yield more reliable classification results. However, in vivo human validation of nerve detecting techniques has limitations. Especially the acquisition of extensive measurements in patients requires much preparation, attention and care. Other models may be more appropriate, allowing more numerous, extensive and repeated measurements, contributing to a robust construction and validation of identification models. Examples of such models are human post mortem (i.e. cadaver) or in animal.

This study aims to expose and understand the similarities and differences to validate nerve measurements between human in vivo, human post mortem, swine in vivo and swine post mortem. This could be of value when choosing a model to validate optical techniques for nerve identification. To this end spectroscopic data, histological slides and anatomy were compared between the four models.

Material and Methods

Diffuse reflectance spectra were acquired from the nerves and surrounding tissues in four different models: human in vivo, human post mortem, swine in vivo and swine post mortem. Nerves included the femoral and sciatic nerve. All nerve measurements were performed by placing the instrument on the nerve, the nerve was never punctured. Surrounding tissue was categorized as subcutaneous fat, muscle and sliding fat. Sliding fat is defined as the fat surrounding the entire nerve bundle[5]. During measurements, the tissue of interest was covered and the surgical lights were dimmed to minimize the influence of environmental light.

Human in vivo measurements

Human in vivo measurements were performed at The Netherlands Cancer Institute – Antoni van Leeuwenhoek under approval of the protocol and ethics review board (NL40893.031.12). Patients undergoing inguinal lymph node dissection or resection of a soft tissue tumor located in the groin were included. Patients were selected based on the likelihood of exposure of the femoral or sciatic nerve. Eighteen patients were included, the diameter of the femoral or sciatic nerve at the measurement location varied from 1 to 13 mm. Comprehensive tissue classification and extensive description of the measured spectra of this human in vivo series are described earlier[12].

Human post mortem measurements

Human post mortem measurements included measurements in four freshly frozen whole body specimens. Fresh frozen bodies are cooled down to -30 degrees Celsius without further preservation. After acclimatization to room temperature, the femoral nerve at both legs was exposed from the inguinal ligament over a trajectory of at least 10 cm. Branches of the femoral nerve were measured to a size of at least 2 mm diameter. The body was then rotated to allow exposure of the sciatic nerve. The sciatic nerve was exposed from 2 to 3 cm caudal from the ischial tuberosity towards the knee.

Swine in vivo measurements

Swine in vivo measurements were conducted under approval of the animal ethics committee (Utrecht University, Utrecht, the Netherlands). During the measurements, animals were anesthetized using isoflurane. The sciatic nerve was exposed over a trajectory of at least 10 cm. A total of six sciatic nerves were measured on three domestic pigs, diameter 4 to 8 mm.

Swine post mortem measurements

Swine post mortem measurements were performed on six sciatic nerves, from three

animals. Similar to the in vivo swine measurements, the nerve was exposed over a trajectory of at least 10 cm, the diameter of the measured nerves was 4 to 8 mm.

Anatomy

The differences between the anatomical structures in the four models were compared based on visual appearance, including size, shape and color. Macroscopic photos were acquired.

Histology

In human post mortem and swine, nerve tissue was resected and surgical biopsies from the surrounding tissues were acquired for histological analysis. The histological slides were stained using standard hematoxylin and eosin.

Instrumentation

Fiber optic probes, including one illumination fiber and one collecting fiber (Invivo Germany, Schwerin, Germany) were used to deliver broad spectrum light from a tungsten-halogen source. The diffusely reflected light, measured via the collecting fiber, was analyzed in the range of 400-1600 nm by two spectrometers (DU420A-BRDD and DU492A-1.7, Andor
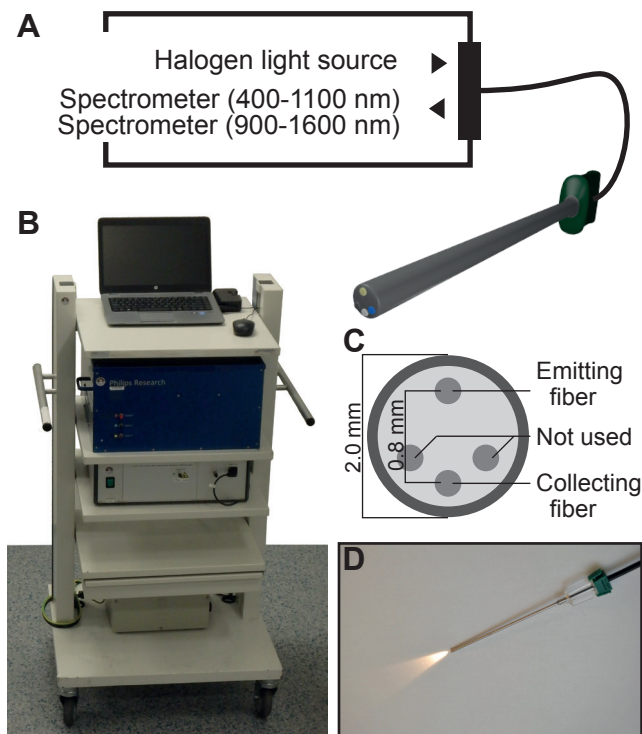

Figure 7.01. | Schematic and photograph of the measurement setup and probe. The tip of the probe is visualized at the middle right.

Technology, Belfast, Northern Ireland) covering the visible and near-infrared range. The distance between the illumination and collection fiber was 0.8 mm, the probe diameter at the tip was 2.0 mm. The setup is schematically represented in Figure 7.01. The measurement setup is controlled by a custom made LabView software interface (National Instruments, Austin, TX, USA). The instrumentation and calibration procedure of the DRS system has been described in detail elsewhere[13].

Spectral analysis

A widely accepted analytical model, first described by Farrell et al., was used to quantify validated physiological, morphological and metabolic parameters within the measured tissue[14]. These parameters include volume fractions or concentrations of the different chromophores and scattering parameters. The implementation of this model to analyze diffuse reflectance spectra over a wavelength of 400-1600 nm is described by Nachabé[13]. The analytical model was implemented into a Matlab software environment (Matworks Inc., Natrick, MA, USA).

Spectra used to fit the measured profile were from oxy- and deoxyhemoglobin, fat, water, β-carotene and collagen. Further, the effects of both Mie- and Rayleigh scattering, the scattering slope (b) and alpha on the spectrum were estimated. In the analysis, outliers were defined as greater than q3 + (q3-q1) or smaller than q1 – (q3-q1) with q1 the 25th and q3 the 75th percentile.

Classification

To evaluate whether classification algorithms intended for human in vivo can be trained and optimized on alternative models, we trained a 3-knn classification on each of the three alternative models and classified the human in vivo data with this algorithm. The classification results in terms of sensitivity, specificity and Matthews correlation coefficient (MCC) were compared with the classification of the human in vivo measurements using a cross-validation scheme. The MCC is used in machine learning as a measure of quality of classifications[15]. Per model, two classification runs were performed: one with all fitted parameters, the second with a subset of parameters. The parameter subset consists of the most distinctive parameters in the in vivo human cross-validation. The parameters in the subset were selected based on the effect on the classification result (MCC) after systematic omission of individual parameters.

Results

Anatomy

Macroscopically, the difference between human and swine is most notable in size; the diameter of the investigated nerves in human was approximately twice the diameter of the swine nerves. In comparison to swine, the appearance of human nerve shows small ribs, or grooves (Fig. 7.02), which may vary per case. There were no significant differences in appearance between human in vivo and post mortem specimens or swine in vivo and post mortem samples.

In the surrounding tissue, the amount of blood differs between the models. By eye, the most blood can be found in living human, followed by in vivo swine, human post mortem and swine post mortem. The color of the subcutaneous fat differed between the specimens.
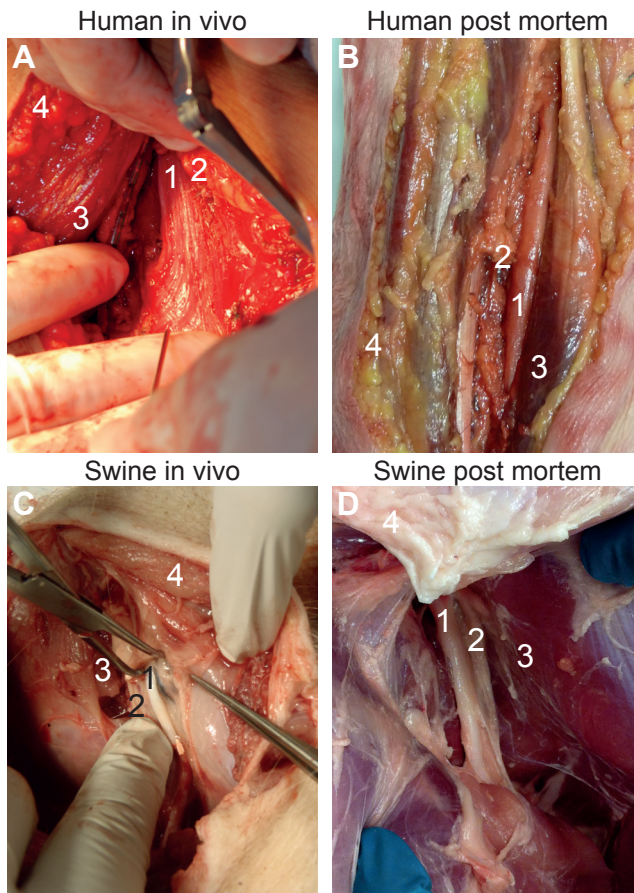

Figure 7.02. | Macroscopic images of the four measurement settings. All images show the sciatic nerve and surrounding tissue.

The subcutaneous fat in human cadaver was yellow, in swine (both in vivo or post mortem) was almost white, and human in vivo was yellow-white.

Histology

In histology, both human and swine nerves were composed of fascicles, enclosed by perineurium. A nerve (branch) is surrounded by an outer layer of connective tissue, the outer epineurium, which is surrounded by a fatty layer: sliding fat. Within the outer epineurium, fascicles are accompanied by adipocytes and loose connective tissue (inner epineurium). Within the inner epineurim, no differences were found in cell type or density between human or swine nervous tissue. Histological images of nerve and surrounding tissue for human and swine are displayed in Figure 7.03. While nerve and fat tissue (or adipose tissue) showed clear similarities between human and swine, differences at histological level were found in muscle. The density of muscle fibers in swine was remarkable higher compared to human. In human muscle considerable more adipocytes and endomysial collagen was present in surrounding the muscle fibers in the muscle.
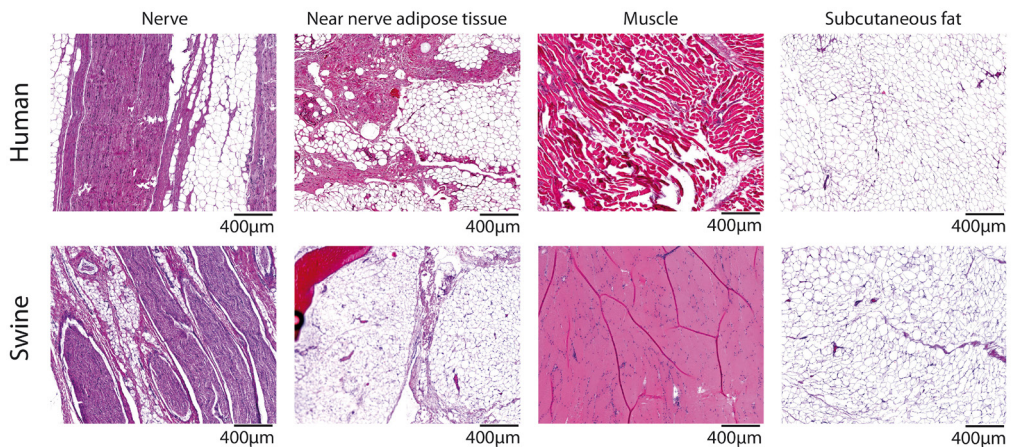
Figure 7.03. | Histological samples for the investigated tissue in both human and swine.

Optical parameters

Optical spectra

Typical examples of the measured spectra were visualized in Figure 7.04. Interpretation of DRS spectra, and an analysis of the spectra characteristics is discussed elsewhere[5].

General trends

The measured values of the optical parameters are visualized in Figure 7.05; measurements are grouped per tissue type and model. The significance of the differences in parameter values, based on a Kruskal Wallis test, are shown in Table 7.01.

nerve

parameter	in vivo human (mean)	ex vivo human	in vivo swine	ex vivo swine
water (vol. frac)	0,55	≈	≈	=
fat (vol. frac)	0,39	↓	↓	↓
fat/(water+fat)	0,57	=	↓	↓
hemoglobin (mg/ml)	2,67	↑	↓	=
O2 sat (%)	84,99	≈	≈	=
β-carotene (x10^{-8} Mol)	1,01	=	↓	↓

sliding fat

parameter	in vivo human (mean)	ex vivo human	in vivo swine	ex vivo swine
water (vol. frac)	0,46	=	=	≈
fat (vol. frac)	0,63	↓	=	↓
fat/(water+fat)	0,88	↓	=	↓
hemoglobin (mg/ml)	1,29	↓	=	↑
O2 sat (%)	81,30	=	=	=
β-carotene (x10^{-8} Mol)	1,65	=	↓	↓

muscle

parameter	in vivo human (mean)	ex vivo human	in vivo swine	ex vivo swine
water (vol. frac)	0,65	≈	↑	≈
fat (vol. frac)	0,10	=	≈	≈
fat/(water+fat)	0,15	=	=	≈
hemoglobin (mg/ml)	9,36	↑	↓	↓
O2 sat (%)	31,85	↑	↓	=
β-carotene (x10^{-8} Mol)	0,12	=	=	=

subcutaneous fat

parameter	in vivo human (mean)	ex vivo human	in vivo swine	ex vivo swine
water (vol. frac)	0,45	=	=	=
fat (vol. frac)	0,59	=	=	↓
fat/(water+fat)	0,83	=	=	↓
hemoglobin (mg/ml)	1,50	↑	≈	=
O2 sat (%)	82,74	=	↓	=
β-carotene (x10^{-8} Mol)	2,05	≈	↓	↓

Table 7.01. | Optically measured concentration. Significant differences (Kruskal Wallis p-value >0.01) are indicated by ↑ or ↓. P-values of <0.001 indicate that the groups show great similarity (=). P-values >0.001 and <0.01 are not significant different (≈).

When comparing nerve with surrounding tissue, the optically measured parameters show comparable trends throughout the four models. On nerve measurements show intermediate amounts of fat, that are high compared with muscle, but low when compared with sliding fat or subcutaneous fat. With regard to the amount of blood, which can only be judged reliably during in vivo measurement, on nerve measurements show higher amounts of blood compared to adipose tissues (sliding fat and subcutaneous fat) but low compared to muscle. Muscle shows high levels of blood and water, with the lowest level of oxygen saturation in all four models. The adipose tissues (subcutaneous fat and sliding fat) are characterized by a high amount of fat and relatively low amounts of water and blood. β-carotene is absent in all swine measurements.

Human in vivo versus post mortem.

The human post mortem measurements contain generally more blood compared with the other models, whereas the variation in oxygen saturation is less pronounced in human post mortem. For on nerve measurements, the content of water and fat appear slightly lower for post mortem compared to in vivo.

Human in vivo versus swine in vivo

For on nerve measurements, the fat fraction measured lower in swine compared to human. Slightly less blood was measured in swine and also the sum of the water and fat volume fraction was lower compared to human. In contrast, for muscle the sum of the water and fat volume fraction was higher for swine compared to human. As for nerve tissue, the amount of blood and the oxygen saturation in muscle were lower in swine compared to human. In adipose tissue in vivo measurements of water, fat and blood content were not different for human or swine.

Trainingset		MCC	Sensitivity	Specificity	Accuracy
Human in vivo (cross validation)		0.60	81%	80%	0.80
Human ex vivo	All parameters	0.47	61%	84%	0.73
	Parameter subset	0.44	73%	71%	0.72
Swine in vivo	All parameters	0.46	39%	98%	0.69
	Parameter subset	0.41	42%	93%	0.68
Swine ex vivo	All parameters	0.46	63%	82%	0.73
	Parameter subset	0.43	51%	89%	0.71

Table 7.02. | The 3-knn classification was trained on the data of human ex vivo, and swine in- and ex vivo and validated on the human in vivo dataset as measure for the similarities between the situations. As input for the training were used all available fit-parameters as well as the subset of parameters selected in the in vivo human cross validation.

Human versus swine post mortem

The on nerve measurements showed great similarities between human in vivo and swine post mortem for the amounts of water and blood. The fat content in swine nervous tissue measured lower compared to human. Both subcutaneous fat and sliding fat showed water content comparable to their human in vivo equivalent. For muscle, human in vivo contained more blood compared to swine post mortem.

Classification

The classification results for training on an alternative model and validation in human in vivo are summarized in Table 7.02. Cross validation within the human in vivo group resulted in an MCC of 0.6 with a sensitivity of 81 % and a specificity of 80 %. The most distinctive parameters were oxygen saturation, the amount of water and fat and the ratio between them, concentrations of hemoglobin and the amount of Mie scattering.

Training the classification algorithm on another model combined with classification on in vivo human indicates the similarity between the two models. In case of maximum resemblance, the accuracy will be comparable to cross-validation within in vivo human. All classifications resulted in an MCC well above 0, indicating a positive correlation. Training was performed using all available parameters but also using only a subset of parameters that were most distinctive in the human cross-validation. The limitation for the classification to use only the parameter subset from the in vivo human cross validation did not result in substantially lower scores. The classification of nerve tissue for human ex vivo and swine in vivo/ex vivo showed minimal differences in MCC and accuracy.

Discussion

Optical nerve identification techniques like DRS aim to fulfill a clinical demand on tissue identification at the tip of an instrument. Due to the small size of optical fibers, the technique could be integrated into surgical tools. During surgery, DRS may help to prevent nerve damage using surgical tools with optical tissue identification at the tip of the instrument. Multiple surgical instruments establish solid tissue contact prior to dissection and are therefore eminently suited for tissue identification. Examples are surgical staplers, harmonic scalpels[16] and vessel sealing devices[17]. In other medical areas, instruments with integrated optical fibers were also subject of research, an example is a tool for tissue biopsy used in radiology[18]. In regional anesthesia, feedback on the tissue type at the tip of a needle may improve accurate deposition of the analgesic around the nerve and therefore improve the quality and onset of a regional nerve block. A prototype of a needle stylet with integrated optical fibers was used presented earlier. The potential of optical techniques to identify nervous tissue was demonstrated by several authors[3-8,19]. Nerve tissue was discriminated between several surrounding tissue including bone and glandular tissue[7], muscle and adipose tissue[5,6,8] and blood vessel[19]. All these studies show good classification results, but none of them reaches perfect (100 %) tissue identification. Furthermore, these studies were performed in a controlled setting.

To move the technique from a controlled experimental setting into a mature clinically applied device is a long process that will require multiple optimization and validation cycles. Not all these cycles are necessarily executed in humans in vivo. In recent literature several models have been described including human post mortem[5], and swine in vivo[3]. Ideally, the optical properties and measured parameters in such models should closely resemble their human in vivo equivalent. A systematic comparison of optical properties between the different models would be useful for a broad range of optical techniques. This study aims to expose and understand the similarities and differences to validate nerve measurements between human in vivo, human post mortem, swine in vivo and swine post mortem. Nerve and surrounding tissue were compared between human and swine macroscopically, histologically, and in optical parameters measured by DRS. This could be of value when choosing a model to validate optical techniques for nerve identification.

Macroscopic examination of the tissue revealed differences in the color of adipose tissue between human and swine. The yellow color of adipose tissue is related to the β-carotene concentration[20]. In general, mammals are categorized as either white-fat or yellow-fat animals: the carotenoid content and color of adipose tissue in yellow-fat animals is due to their ability to absorb, transport and store carotenoids, whereas white-fat animals lack this ability; humans have yellow fat, while pigs, rats and mice have white-fat[21].

The quantified amount of blood in the tissue shows model dependency. The amount of blood is consistently high in human post mortem and low for swine in vivo. The low amount in swine in vivo might be due to the low arterial blood pressure during surgery;

advised mean arterial pressure (MAP) in swine is 60-70 mmHg[22]. Compared to surgery in humans, smaller decrease of arterial pressure is allowed. A decrease of systolic arterial pressure (SAP) higher than 20 % is often chosen to define perioperative hypotension in human[23]. Post mortem, the coagulation is disturbed for several reasons including temperature. In swine post mortem, the blood is drained, in human post mortem the body still contains substantial amounts of blood. Post mortem the distribution of blood between veins and arteries is shifted toward the venous system, also increasing the blood volume in capillaries[24]. As the coagulation system is largely disturbed post mortem, increased bleeding during preparation occurs. The combination of these factors may lead to the high measurements for the blood parameter in human post mortem compared to in vivo and low in swine post mortem.

Related to the amount of blood is the hemoglobin oxygen saturation. In post mortem tissue, cellular metabolism is assumed to have ceased, and oxygen is no longer consumed. Meanwhile, tissue preparation provides exposure to room air allowing the hemoglobin to saturate with oxygen, analogous to the increase in oxygen saturation if an air bubble is trapped in a blood gas syringe[25]. However, the measured oxygen saturation still shows low oxygen saturation in muscle. Although the difference in oxygen saturation between nerve and muscle is lower in the post mortem measurements, muscle tissue still shows lower values. A possible explanation is the presence of methemoglobin within the post mortem muscle; methemoglobin is the oxidized form of hemoglobin and could increase post mortem[26]. The presence of methemoglobin may influence the estimation of the oxygen saturation. Currently, methemoglobin is not included in the fitting algorithm.

The typical age of the specimen in the four different models (human in/ex vivo, swine in/ex vivo) differs. Human cadavers available for research are typically older than patients undergoing surgery. Swine used for training surgical procedures are typically full grown where domestic slaughter pigs are typically 3-8 months old. The differences in age may have had an impact on the histological appearance of the muscle tissue; the amount of adipocytes and endomysial collagen in human muscle was clearly higher compared to swine. Intramuscular connective tissue, including perimysium and endomysium, is known to increase with age[27]. In this research, patients and specimens were not selected based on age. Patients and specimens represent the typical age in their group.

Conclusion

In this study, three alternative models for the development of optical techniques for nerve identification were examined. Differences in macroscopy, histology and optically derived parameters were compared between human in vivo and the alternative models. Despite differences in appearance and histology, similarity between optical parameters is sufficient to yield a strong positive correlation after cross model classification. The presented similarities and differences could be of value in optical tissue recognition

techniques like DRS, multispectral camera's and Raman spectroscopy, especially when choosing a model for validation and optimization. When the distinguishing features of an identification algorithm are known, an alternative model could be selected with maximum similarities to human in vivo regarding these features.

Acknowledgements

7

References

1. 1. Urmey WF, Stanton J. Inability to consistently elicit a motor response following sensory paresthesia during interscalene block administration. Anesthesiology 2002; 96(3):552-554.

2. Perlas A, Niazi A, McCartney C, Chan V, Xu D, Abbas S. The sensitivity of motor response to nerve stimulation and paresthesia for nerve localization as evaluated by ultrasound. Region Anesth Pain M 2006; 31(5):445-450.

3. Brynolf M, Sommer M, Desjardins AE, van der Voort M, Roggeveen S, Bierhoff W, Hendriks BH, Rathmell JP, Kessels AG, Söderman M. Optical detection of the brachial plexus for peripheral nerve blocks: An in vivo swine study. Region Anesth Pain M 2011; 36(4):350-357.

4. Desjardins AE, Van der Voort M, Roggeveen S, Lucassen G, Bierhoff W, Hendriks BH, Brynolf M, Holmström B. Needle stylet with integrated optical fibers for spectroscopic contrast during peripheral nerve blocks. J Biomed Opt 2011; 16(7):077004.

5. Hendriks BH, Balthasar AJ, Lucassen GW, van der Voort M, Mueller M, Pully VV, Bydlon TM, Reich C, van Keersop AT, Kortsmit J. Nerve detection with optical spectroscopy for regional anesthesia procedures. J Trans Med 2015; 13(1):380.

6. Schols RM, ter Laan M, Stassen LP, Bouvy ND, Amelink A, Wieringa FP, Alic L. Differentiation between nerve and adipose tissue using wide-band (350–1,830 nm) in vivo diffuse reflectance spectroscopy. Laser Surg Med 2014; 46(7): 538-545.

7. Stelzle F, Knipfer C, Bergauer B, Rohde M, Adler W, Tangermann-Gerk K, Nkenke E, Schmidt M. Optical nerve identification in head and neck surgery after Er: YAG laser ablation. Laser Med Sci 2014; 29(5):1641-1648.

8. Balthasar A, Desjardins AE, van der Voort M, Lucassen GW, Roggeveen S, Wang K, Bierhoff W, Kessels AG, van Kleef M, Sommer M. Optical detection of peripheral nerves: an in vivo human study. Region Anesth Pain M 2012; 37(3):277-282.

9. Schols RM, Dunias P, Wieringa FP, Stassen LP. Multispectral characterization of tissues encountered during laparoscopic colorectal surgery. Med Eng Phys 2013; 35(7):1044-1050.

10. Langhout GC, Spliethoff JW, Schmitz SJ, Aalbers A, van Velthuysen ML, Hendriks BH, Ruers TJ, Kuhlmann KF. Differentiation of healthy and malignant tissue in colon cancer patients using optical spectroscopy: A tool for image-guided surgery. Laser Surg Med 2015; 47(7):559-565.

11. Evers DJ, Nachabe R, Peeters M-JV, van der Hage JA, Oldenburg HS, Rutgers EJ, Lucassen GW, Hendriks BH, Wesseling J, Ruers TJ. Diffuse reflectance spectroscopy: towards clinical application in breast cancer. Breast Cancer Res Tr 2013; 137(1):155-165.

12. Langhout GC, Kuhlmann KFD, Wouters MWJM, van der Hage JA, van Coevorden F, Müller M, Bydlon TM, Sterenborg HJCM, Hendriks BHW, Ruers TJM. Nerve detection during surgery: Optical spectroscopy for peripheral nerve localization. Laser Med Sci 2017; in press

13. Nachabé R, Evers DJ, Hendriks BH, Lucassen GW, van der Voort M, Rutgers EJ, Peeters M-JV, Van der Hage JA, Oldenburg HS, Wesseling J. Diagnosis of breast cancer using diffuse optical spectroscopy from 500 to 1600 nm: comparison of classification methods. J Biom Opt 2011; 16(8):087010-087012.

14. Farrell TJ, Patterson MS, Wilson B. A diffusion theory model of spatially resolved, steady□state diffuse reflectance for the noninvasive determination of tissue optical properties in vivo. Med Phys 1992; 19(4):879-888.

15. Powers DM. Evaluation: from precision, recall and F-measure to ROC, informedness, markedness and correlation. J Mach Learn Tech 2011; 2(1):37-63.

16. Miccoli P, Berti P, Dionigi GL, D'Agostino J, Orlandini C, Donatini G. Randomized controlled trial of harmonic scalpel use during thyroidectomy. Archives of Otolaryngology–Head Neck Surg 2006; 132(10):1069-1073.

17. Landman J, Kerbl K, Rehman J, Andreoni C, Humphrey PA, Collyer W, Olweny E, Sundaram C, Clayman RV. Evaluation of a vessel sealing system, bipolar electrosurgery, harmonic scalpel, titanium clips, endoscopic gastrointestinal anastomosis vascular staples and sutures for arterial and venous ligation in a porcine

model. J Urology 2003; 169(2):697-700.

18. Spliethoff JW, Prevoo W, Meier MA, de Jong J, Evers DJ, Sterenborg HJ, Lucassen GW, Hendriks BH, Ruers TJ. Real-time in vivo tissue characterization with diffuse reflectance spectroscopy during transthoracic lung biopsy: a clinical feasibility study. Clin Cancer Res 2015: 0807.

19. Balthasar A, Desjardins AE, van der Voort M, Lucassen GW, Roggeveen S, Wang K, Bierhoff W, Kessels AG, Sommer M, van Kleef M. Optical detection of vascular penetration during nerve blocks: an in vivo human study. Region Anesth Pain M 2012; 37(1):3-7.

20. Wu L, Guo X, Wang W, Medeiros DM, Clarke SL, Lucas EA, Smith BJ, Lin D. Molecular aspects of β, β-carotene-9′, 10′-oxygenase 2 in carotenoid metabolism and diseases. Exp Biol Med 2016; 241(17):1879-1887.

21. Krinsky NI, Mayne ST, Sies H. Carotenoids in health and disease. New York, United States: Taylor & Francis Inc (CRC press). 2004. 576 p.

22. Swindle MM, Smith AC. Swine in the laboratory: surgery, anesthesia, imaging, and experimental techniques. New York, United States: Taylor & Francis Inc (CRC press). 2015.

23. Lonjaret L, Lairez O, Minville V, Geeraerts T. Optimal perioperative management of arterial blood pressure. Integr Blood Press Control 2014, 7:49.

24. Koeppen B. Stanton BA. Berne and Levy Physiology. Atlanta, United States: Elsevier Inc. 2008; 394 p.

25. Biswas C, Ramos J, Agroyannis B, Kerr D. Blood gas analysis: effect of air bubbles in syringe and delay in estimation. Br Med J 1982; 284(6320):923-927.

26. Reay DT, Insalaco SJ, Eisele J. Postmortem methemoglobin concentrations and their significance. J Forensic Sci 1984; 29(4):1160-1163.

27. Fang S, Nishimura T, Takahashi K. Relationship between development of intramuscular connective tissue and toughness of pork during growth of pigs. J Anim Sci 1999; 77(1):120-130.

7

Optimal endobronchial tool sizes for targeting lung lesions based on 3D modeling

For patients with suspicious lung lesions found on chest x-ray or CT, endo/trans-bronchial biopsy of the lung is the preferred method for obtaining a diagnosis. With the addition of new screening programs, a higher number of patients will require diagnostic biopsy which will prove even more challenging due to the small size of lesions found with screening. There are many endobronchial tools available on the market today and a wide range of new tools under investigation to improve diagnostic yield. However, there is little information available about the optimal tool size required to reach the majority of lesions, especially peripheral ones. In this manuscript we investigate the percentage of lesions that can be reached for various diameter tools if the tools remain inside the airways (i.e. endobronchial biopsy) and the distance a tool must travel "off-road" (or outside of the airways) to reach all lesions.

To further understand the distribution of lung lesions with respect to airway sizes and distances from the airways, six 3D models of the lung were generated. The airways were modeled at two different respiratory phases (inspiration and expiration). Three sets of 1,000 lesions were randomly distributed throughout the lung for each respiratory phase. The simulations showed that the percentage of reachable lesions decreases with increasing tool diameter and decreasing lesion diameter. A 1mm diameter tool will reach <25 % of 1 cm lesions if it remains inside the airways. To reach all 1cm lesions this 1mm tool would have to navigate through the parenchyma up to 8.5 mm. CT scans of 21 patient lesions confirm these results reasonably well.

The smaller the tool diameter the more likely it will be able to reach a lung lesion, whether it be for diagnostic biopsy, ablation, or resection. However, even a 1 mm tool is not small enough to reach the majority of small (1-2 cm) lesions. Therefore, it is necessary for endobronchial tools to be able to navigate through the parenchyma to reach the majority of lesions.

T.M. Bydlon, G.C. Langhout, F. Lalezari, K.J. Hartmink, J. Nijkamp, S.G. Brouwer de Koning,

J.A. Burgers, B.H.W. Hendriks, T.J.M. Ruers

Introduction

For patients with suspicious lung lesions found on chest x-ray or CT, endobronchial and/ or transbronchial biopsy of the lung is the preferred method for obtaining a diagnosis, with transthoracic CT-guided biopsy and surgical biopsy as alternative approaches. The NELSON study found that 62.7 % of lesions were located in the periphery of the lung compared to the pleural wall (10 %), middle (11.6 %), or central (15.3 %) airways[1]. In the central airways, approximately 4 endobronchial (tools remain in the airways) biopsies are needed to obtain an adequate diagnostic yield which has been reported to be 70-90 %[2]. For peripheral lesions, fluoroscopy-guided transbronchial (tools traverse the airway wall) biopsy is the standard technique. Reported rates for diagnostic yield in peripheral lesions are 30-78 %[2-5] and are especially low for small lesions <2 cm in diameter (30-34 %)[4,5]. Attempts have been made with endobronchial ultrasound (EBUS) probes, electromagnetic (EM) navigation, virtual navigation bronchoscopy, and bronchoscopic transparenchymal nodule access to improve diagnostic yield; however, none of these techniques have gained wide acceptance[6,7]. Overall ~60 % of patients will return for a second procedure (transthoracic or surgical biopsy) if diagnostic yield is insufficient[3,6].

In the last decade several large population studies have been completed to assess the benefits of low-dose CT (LDCT) screening in the general population which has led to some countries implementing screening programs[8-17]. Given the increasing number of small, peripheral lesions detected by these screening programs, better biopsy tools will be required to achieve good diagnostic yield and follow-up.

There are many types of new lung tools that have been reported in the literature and some that are now entering the market. These new tools aim to improve diagnostic yield by providing better navigational guidance to the lesion (example, EM tracking[18-20]) or by evaluating the tissue prior to biopsy (examples, EBUS[21], radial endobronchial ultrasound [REBUS][21], optical coherence tomography[22-27], fluorescence spectroscopy[28,29], diffuse reflectance spectroscopy[28-30], Raman spectroscopy[31-33], or differential path length spectroscopy[30,34-36]). These new tools will improve diagnostic yield but only if they can physically reach the lesion. After evaluating the current literature we were unable to find sufficient information on the ideal tool size required to be effective in targeting the majority of lung lesions endobronchially. The goal of this manuscript was to therefore investigate the percentage of lesions that can be reached for various diameter tools if the tools remain inside the airways (i.e. endobronchial biopsy) and the distance a tool must travel "off-road" (or outside of the airways) to reach all lesions.

Methods

3D simulations of the human airways and randomly distributed lesions

A 3D model of the human airways, based on a deterministic algorithm that incorporates both duct branching and space division, has been developed by Hiroko Kitaoka et al.[37,38] This model was used to generate an airway tree (Model Type 1) with 3311 branches. In the model the region of interest was set to 0 (whole lung), lung capacity at beginning of inspiration to 0.35, lung capacity at end of inspiration to 1.0, inspiratory time to 0.4, and a supine body posture assumed. For this exercise, only two time points in the respiratory cycle were used – when the lung is fully inflated (here forth referred to as 'inspiration') and when fully exhaled ('expiration'). This model also generated a 3D volume of the entire lung.

Lung lesions were randomly generated using MATLAB (MathWorks, Natick, MA). Results from the NELSON trial[13] showed the distribution of lesions in the x-z (transverse) and x-y (coronal) planes. These distributions were used to define a probability distribution function (PDF) in the x- and y-axes; for the z-axis a uniform PDF was used for simplicity. A PDF was also defined for the left and right lung. The PDF's were contained within the lung volume by manually selecting the minimum and maximum x, y, and z coordinates from the generated lung volume image; this was repeated 3 times to ensure the correct lung volume was used. The x, y, and z coordinates of 1000 points (i.e. lesions) were randomly drawn based on these PDF's and 3 lung volumes. Three sets of lesions was drawn for the inspiration models and another 3 for the expiration models (in total 6 models of airways and lesions were created). A single set couldn't be generated for both inspiration and expiration since the airways are in motion and the lung lesions are defined by fixed x, y, and z coordinates. The majority of lung lesions generated were found in the upper half of the lung or in the periphery, as expected based on the NELSON distributions. Figure 8.01 shows the expiration airway model with the three sets of 1000 randomly generated lung lesions.

The airway model is exported in VTK-format and consists of vertices and triangular faces. MATLAB was used to calculate the diameter of the airways at each face by iteratively stepping through each face, finding the opposite face, and calculating the distance between the two respective planes. When an opposite face could not be determined the diameter at that face was set to NaN (not a number).

Next, for each of the 1000 lesions in the 6 models (3 different distributions x 2 respiratory states), a spherical mesh was created to represent the lesion with diameters ranging from 1 mm to 5 cm in 1 mm increments. The intriangulation function in MATLAB was used to determine if there were any vertices or faces of the airway mesh that were inside the lesion mesh. For the faces and vertices that were found to be within the lesion mesh, the corresponding airway diameter was recorded. This was repeated for all lesion diameters,
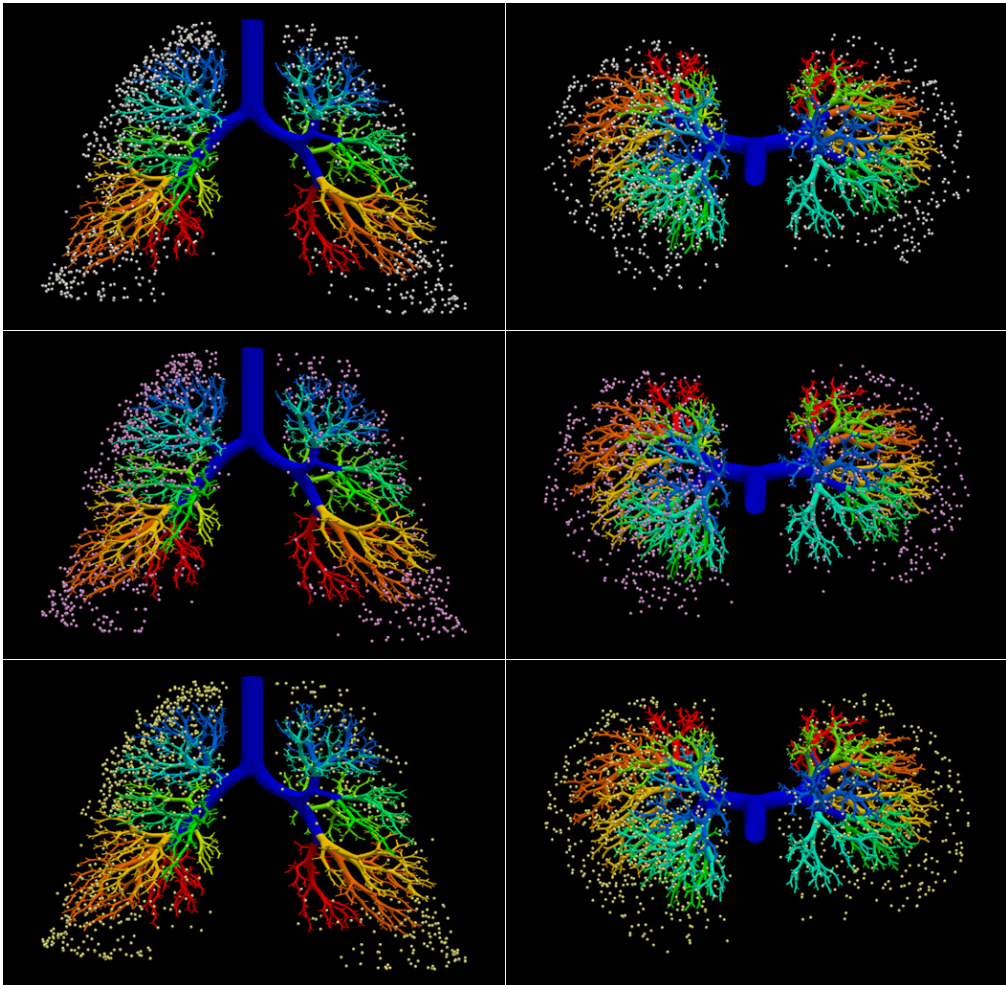
Figure 8.01. | Simulated airway model at expiration showing 2mm lesions as spheres distributed randomly throughout the lung. The different colored lesions represent the 3 repeated models (white = model 1; pink = model 2; yellow = model 3). Images were created in ParaView 4.3.1.

lesions, and models. To calculate the percentage of reachable lesions we counted the number of lesions that intersected with an airway whose diameter was larger than the tool size and divided by the total number of lesions (i.e. 1000); this percentage was calculated for tool sizes ranging from 1-9 mm in 0.5 mm increments.

In these models, lesions are not always connected to an airway. Therefore, it is important to understand how far a tool must reach beyond the bronchial wall (i.e. going "off-road" in the parenchyma as in the case of transbronchial biopsy) to reach the boundary of a lesion. Figure 8.02 shows how this off-road distance was calculated. For example, given a lesion with radius r1, a small device (Device1) can be navigated inside the airways until it reaches an airway with diameter D1 which is approximately the same size as the tool itself.

A larger device (Device2) can't be navigated as far down the airways and gets stuck when the airway diameter is D2. At this point the tool would have to exit the airway and travel through the parenchyma to reach the lesion. In the case of Device1 this distance is simply the difference between r2 and r1, where r2 is taken as the radius of the first spherical lesion mesh which intersects with an airway greater than or equal to diameter D1. For Device2 the off-road distance would then be the difference between r3 and r1.

A few limitations should be noted regarding these simulations. First, the smallest airway diameter that is calculated from the Kitaoka airway tree is 0.1 mm. If every branch termination was this small we could make conclusions about tool sizes down to 0.1 mm. However, not every branch termination was smaller than 1mm, therefore, we will only draw conclusions based on tool diameters >1 mm. Second, this analysis does not take into account any information about how the airways stretch or deform when a tool is navigated through them. Because the airways have some elasticity a tool may be able to be navigated into airways smaller than the tool diameter. Lastly, expiration and inspiration
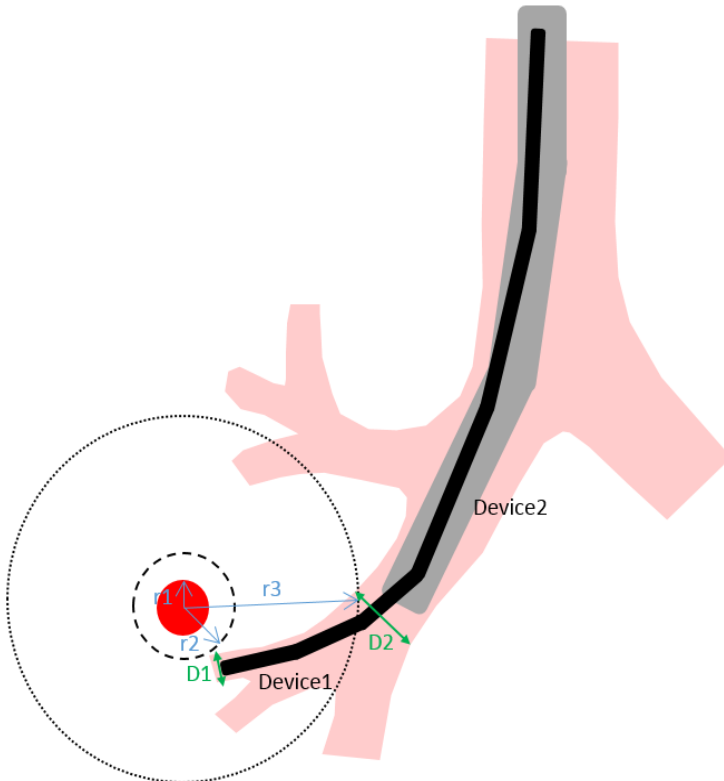

Figure 8.02. | Depiction of how to calculate the off-road distance.

states were treated as two separate models with different lesion distributions and cannot be compared exactly.

CT image analysis

This manuscript involves a retrospective analysis of CT images from lung cancer patients at the Netherlands Cancer Institute – Antoni van Leeuwenhoek Hospital. All patients underwent CT imaging as part of their standard clinical diagnostic care; no additional imaging examinations were performed for the data in this manuscript. The hospital ethics committee was consulted; under Dutch law the study did not require IRB approval (or patient informed consent). Only the authors associated with the hospital (GCL, FL) had access to the imaging data and performed the image analysis; measurement data was fully anonymized and de-identified. Images were restricted to patients with lung lesions >1 cm and <4 cm without prior radiotherapy. Helical CT Single Breath Hold Scans were reconstructed with 1.0 mm slice thickness and 1.0 mm slice increment. For lesions that were in contact with an airway, the airway diameter was measured. The distance between the lesion and closest airway of 1, 2, 4 and 6 mm diameter was measured. Measurements were performed in the VUE PACS (Carestream Health, Rochester, NY, USA) viewing software using Cross-sectional MPR visualization.

Results

From the CT scans 21 lesions were included. The lesions were non-small cell lung carcinoma and sarcoma or melanoma metastases, ranging in diameter from 9.7 mm to 3.6 cm (1.6 cm mean, 1.3 cm median). Figure 8.03 shows the lesions projected in a 3D model derived from a CT scan without lesions: isosurface function in MATLAB and exported to Blender (Blender Foundation, Amsterdam, The Netherlands) for visualization. The size of the lesion represents the average diameters in the x, y and z direction. The location is the location of the measured lesion to the center of a 3D box enclosing the lungs.
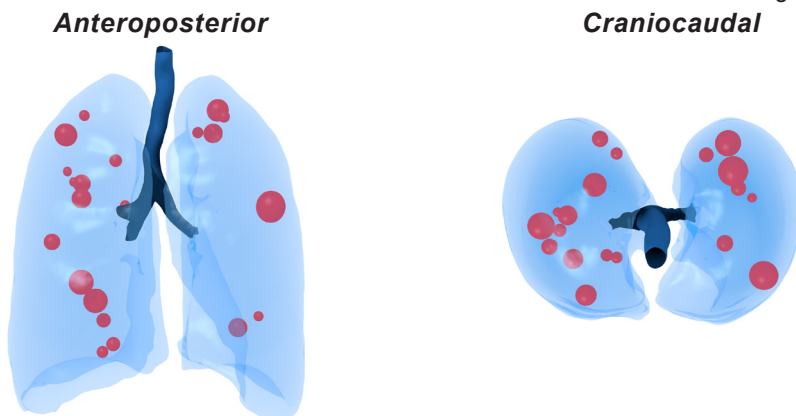
Anteroposterior   **Craniocaudal**

Figure 8.03. | 3D model of the lungs with the lesions (size and location) measured from the CT scans.

Most lesions appear in the right lung or upper lobes, similar to the NELSON trial[13] and simulated distributions.

In Figure 8.04 and Figure 8.05 the simulated 3D data and the CT data are shown together for comparison. Figure 8.04 shows the percentage of reachable lesions versus various sized tools for different lesion sizes. Each of the 3 simulated models is shown as a separate color but for the most part these 3 models have very similar results. As would be expected, the smaller the tool size, the more lesions that can be reached. And the larger the lesion, the more likely it can be reached even with a larger tool. Although the number of lesions
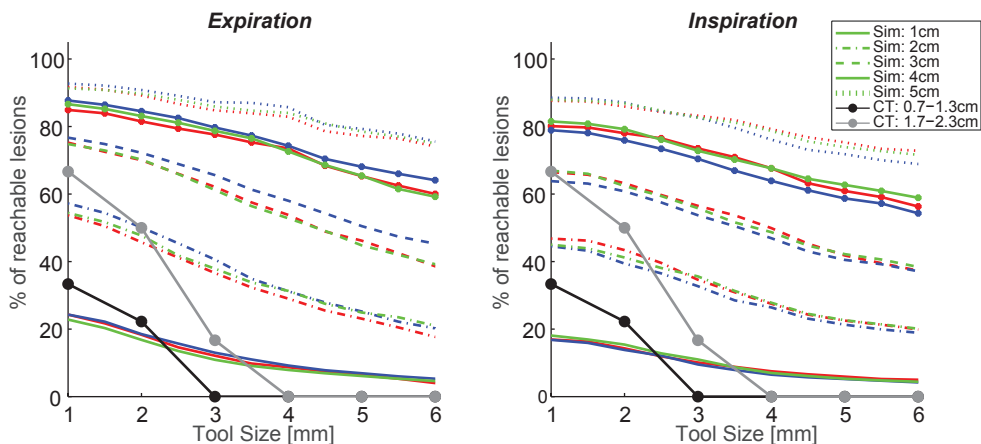
Figure 8.04. | *Percentage of lesions within reach of different sized tools if the tool remains inside the airways. Colors indicate the simulated model (1- red, 2 – blue, 3 – green); black and gray are the CT data for lesions of 0.7-1.3cm and 1.7-2.3cm diameter respectively.*
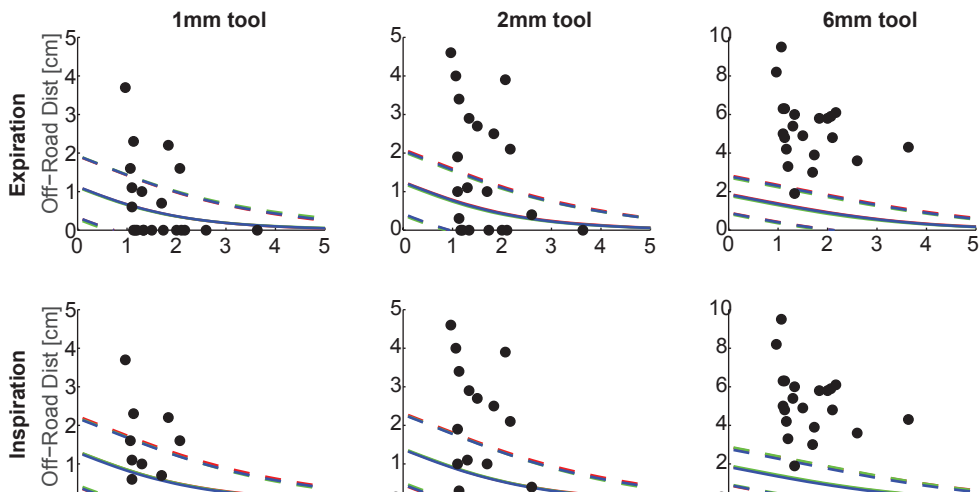
Figure 8.05. | *Distance a tool must travel off-road to reach a lesion. Colors indicate the simulated model (1- red, 2 – blue, 3 – green) and the lines represent the average and standard deviations. The black dots are the lesions measured from the CT scans.*

acquired from the CT scans is limited, there is reasonable agreement for the lesion sizes. In the CT data the majority of the lesions which touched an airway were next to 1 or 2 mm airways; only one was next to a 3 mm airway and one next to a 5 mm airway.

Figure 8.05 shows the simulated average (and standard deviation) distance a tool would have to travel off-road to reach various sized lesions. Only one simulated model is shown since the other two models are nearly identical. For all tool sizes, the larger the lesion size the shorter the off-road distance. For example, a 6.3 mm bronchoscope would have to go nearly 2 cm to reach the smallest lesions, while a 1 mm tool would only need to travel off-road ~1 cm. The CT data overlaps reasonably well with the 1 mm and 2 mm diameter tools, however, diverges for the 6 mm diameter tool.

Discussion

The 3D simulations were used to better understand how small an endobronchial tool must be to reach the majority of lung lesions and how far a tool must travel beyond the bronchial wall through the parenchyma (off-road) if a lesion is not connected to the airways.

The simulations show that the percentage of small (<1 cm) lesions that can be reached, even with a 1mm tool, is quite low at only 17.3 % (inspiration) and 23.8 % (expiration). To provide further insight into this, in one of the inspiration models 989/1000, 1 mm diameter lesions did not touch an airway; this only slightly decreases to 918/1000 for 5 mm lesions. It is possible that these small lesions are touching an airway but they would be <1 mm in diameter as this was the limit of our model. For the small lung lesions that will most likely be found with LDCT screening, this means that in endobronchial biopsy, the biopsy tool has to pass through the bronchiolar wall towards the lesion (transbronchial biopsy). For lesions 1 cm in diameter, a 1mm tool would have to travel on average 8.5 mm (inspiration) or 6.7 mm (expiration) off-road, and farther for larger sized tools. To consider these results in another context, a standard 6.3 mm diameter bronchoscope would reach <10 % of 1 cm lesions, <30 % of 2 cm lesions, and <50 % of 3 cm lesions. Most pulmonologists would agree that a bronchoscope this size can only reach central lesions which according to the NELSON study consisted of 15.3 % of the overall lesions in the lung[1]; thus within the range of the percentages found here.

The CT data supports the results derived from the simulations; reasonable overlap is seen in both Figure 8.04 and Figure 8.05. Compared to the 1000 simulated lesions in each model, the CT data is limited; with additional CT data it is assumed that the distributions in Figure 8.04 would match the simulated distributions more closely. Regardless of the data size, the CT lesions 0.7-1.3 cm in diameter are close to the 1 cm simulated curve, while the 1.7-2.3 cm CT lesions are close to the 2 cm simulated curve with the error between CT and simulation increasing with increasing tool size. On average, the off-road distance measured from the CT scans is close to the average calculated from the simulations for the 1 mm and 2 mm diameter tools, however, quite different for a 6 mm tool. This is likely

due to the fact that the airway diameters are slightly different between the simulated and CT data. From the CT scans the trachea measures ~1.8-2 cm, the main bronchi ~1-1.4 cm, and the lobar bronchi ~6-9 mm. In the simulated data the trachea is ~1.4-1.5 cm, the main bronchi ~1-1.2 cm, and the lobar bronchi ~1-1.1 cm; 6 mm sizes do not occur until the segmental branches. The diameter difference in the lobar bronchi is likely the reason for the deviation between the CT and simulated data in both Figure 8.04 and Figure 8.05. Since the lobar bronchi are larger in the simulated data, a large tool (i.e. 6 mm bronchoscope) can be navigated further into the airways and hence the off-road distance to distal lesions is shorter compared to the CT data where a large tool will get stuck sooner. To confirm this assumption, we approximated the position of each CT nodule in the airway model and calculated the nearest airway diameter and off-road distance. The diameter of the closest airways were slightly larger when the CT nodules were placed in the airway model compared to the CT scans; and the off-road distance was smaller, especially for the 6 mm diameter tool.

As was already mentioned in the Methods section there are some limitations with the models used in this analysis which may impact the conclusions that can be drawn from the results. First, our 3D lung model had 3311 branches. The smallest diameter airway in this model was 0.1 mm, but this was not at the ends of every branch, therefore conclusions cannot be drawn for tools <1 mm in diameter. Regardless, the ability to make a <1 mm diameter tool with all the required functionality is almost impossible at this time and may therefore not be relevant.

The second, and likely more impactful, limitation of these models is that there is no stretching or deformation of the airways that is taken into account in determining the airway to lesion distances. Biological tissues have some elasticity and the airways will stretch when the endobronchial tools are advanced. Therefore, it is likely that in reality more lesions are reachable and the distance that the tools would need to travel is likely to be shorter.

It is also assumed that a tool traveling along an optimal path can be accurately navigated and localize any lesion. Obviously there are limitations to this today. However, with new techniques like electro-magnetic navigation bronchoscopy or image-guided bronchoscopy the ability to accurately navigate a tool along an optimal path may become more reasonable. Highly steerable, flexible tools would also be required for this.

Looking at the current literature and products on the market there are a variety of tools becoming available to pulmonologists to assess airways, biopsy tissue, and treat abnormalities. Given all of these new tools that could impact patient care it is important to understand how impactful they can be given their current sizes. Additionally for anyone designing new endobronchial tools it is important to understand the design criteria needed to target the majority of lung lesions.

Medtronic's superDimension™ Navigation system and Veran Medical Technologies' SPiN

SYSTEM™ are probably the most widely known systems that are on the market to provide better navigational guidance, like a GPS, in the lung to localize lesions. superDimension™ consists of a tracking tool enabled with an electro-magnetic (EM) sensor and separate biopsy tools (1.7-1.9 mm), like brushes, needles, forceps, etc., which are designed to fit down the working channel of a standard bronchoscope. From our simulations, the ~2 mm EM sensor and biopsy tools would reach only 13.8-18.5 % of 1 cm lesions if the sensor remains in the airways. The benefit of a tracked technology is that the tools can still be located even when they must be used off-road. Overall, the clinical usefulness of EM navigational guidance is still under consideration. Some argue that it is a safe and effective tool for obtaining a diagnosis in high risk individuals that can't undergo invasive procedures[18]. While other reports are less optimistic as diagnostic yield can be heavily impacted by a bronchus sign on CT and respiratory motion[19,20].

Ultrasound techniques, including linear endobronchial ultrasound (EBUS) and radial endobronchial ultrasound (REBUS) are beginning to play a larger role in the diagnosis and staging of lung malignancies by providing additional imaging of the airways[21]. Linear EBUS probes are typically quite large (>6 mm diameter) and therefore restricted to the central airways. REBUS probes on the other hand, are much smaller (1.4 mm), potentially reaching more peripheral lesions. From the simulations a 1.4mm REBUS probe would directly reach 16.4-22.0 % of 1 cm lesions. It should be noted however that REBUS has a penetration depth of a few centimeters and would therefore be able to image lesions beyond the airway wall; thus the percentage of "reachable" lesions would be at least 4x higher than a tool that needs to be in direct contact with the tissue which is the case for a biopsy. Although REBUS can potentially image more lesions than EBUS, the probe must be exchanged with forceps or a needle to take the actual tissue sample as it's too large for the working channel to accommodate both tools.

A variety of optical based techniques can be found in the literature where they are predominately used to image the structure of the airways, like ultrasound, or to provide real-time biochemical and morphological information related to tissue composition. Light-based techniques are an attractive option because they are non-destructive to the tissue and are compact enough to fit through the working channel of a bronchoscope[22]. Tissue characterization tools like Raman spectroscopy[31-33], diffuse reflectance spectroscopy (DRS)[28-30], fluorescence spectroscopy[28,29], and differential path-length spectroscopy (DPS) [30,34-36] have been investigated for lung cancer detection, achieving >92 % sensitivity and specificity with Raman[31,32] and >80 % sensitivity and specificity with DRS and DPS[28-30,39]. These technologies have not yet been investigated for endobronchial access and it is unknown how small these types of tools could be made. Like ultrasound, they can also measure tissue beyond the airway wall with a penetration depth on the order of millimeters, thus increasing the percentage of reachable lesions 2-fold. Another optical technique, autofluorescence bronchoscopy, is already on the market and shows improved performance in sensitivity but is still limited to the central airways due to its size and

specificity is low[31]. To our knowledge the only group that has investigated the feasibility of peripheral airway optical sensing is that of Suter et al.[23,24,26,27]. They developed an optical coherence tomography (OCT) imaging catheter integrated inside a 21-gauge TBNA needle to target peripheral airways which was tested in ex-vivo swine lungs[23]. OCT uses light scattering to produce an image of the tissue structure, similar to ultrasound but with much finer resolution and at the expense of imaging depth. The integration of both the imaging and biopsy needle into a single catheter shows real hope that a fully integrated tool could eventually be made. From our simulations, their 21-gauge needle (assuming a 2mm penetration depth) would reach ~28-36 % of 1 cm lesions.

From the 3D simulations and CT analyses, we have shown that for most lung lesions that will be detected with LDCT screening the small size of these lesions will make it challenging to reach, biopsy, and treat them endobronchially. In the majority of patients biopsy tools and/or treatment devices such as ablation needles will need to traverse the bronchial walls and proceed off-road to successfully reach the lesions; or we need tools that are <1 mm in diameter; a challenging task. Typically the tool tip will need to travel 1-2 cm off-road to reach and biopsy/treat a lesion. Given this information, any new technology being developed for navigational guidance, tissue confirmation, or treatment needs to be made small enough and should be able to traverse the bronchial wall to have the greatest impact in the pulmonology workflow.

Acknowledgements

8

References

1. Nanda Horeweg CMvdA, Erik Thunnissen, Kristiaan Nackaerts,, Carla Weenink HJMG, Jan-Willem J. Lammers, Joachim G. Aerts, Ernst T. Scholten,, Joost van Rosmalen WM, Matthijs Oudkerk, and Harry J. de Koning. Characteristics of Lung Cancers Detected by Computer Tomography Screening in the Randomized NELSON Trial. Am J Respir Crit Care Med. 2013;187(8):848-54.

2. Ofiara LM, Navasakulpong A, Ezer N, Gonzalez AV. The importance of a satisfactory biopsy for the diagnosis of lung cancer in the era of personalized treatment. Curr Oncol. 2012 Jun;19(Suppl 1):S16-23.

3. Kadam Adam Lee AAR, Leah Amir. Cost–effectiveness of endobronchial percutaneous biopsy compared with transthoracic biopsy for diagnosis of peripheral lung lesions. Lung Cancer Management. 2014;3(2):135-48.

4. Mazzone P, Jain P, Arroliga AC, Matthay RA. Bronchoscopy and needle biopsy techniques for diagnosis and staging of lung cancer. Clin Chest Med. 2002 Mar;23(1):137-58, ix.

5. Ishida T, Asano F, Yamazaki K, Shinagawa N, Oizumi S, Moriya H, et al. Virtual bronchoscopic navigation combined with endobronchial ultrasound to diagnose small peripheral pulmonary lesions: a randomised trial. Thorax. 2011 Dec;66(12):1072-7.

6. Midthun DE. Overview of the initial evaluation, treatment and prognosis of lung cancer. 2014; Available from: http://www.uptodate.com/contents/overview-of-the-initial-evaluation-treatment-and-prognosis-of-lung-cancer?source=see_link.

7. Gilbert C, Akulian J, Ortiz R, Lee H, Yarmus L. Novel bronchoscopic strategies for the diagnosis of peripheral lung lesions: present techniques and future directions. Respirology. 2014 Jul;19(5):636-44.

8. Ru Zhao Y, Xie X, de Koning HJ, Mali WP, Vliegenthart R, Oudkerk M. NELSON lung cancer screening study. Cancer Imaging. 2011;11 Spec No A:S79-84.

9. Horeweg N, de Koning HJ. Reply: stage distribution of lung cancers detected by computed tomography screening in the NELSON Trial. Am J Respir Crit Care Med. 2013 Oct 15;188(8):1035-6.

10. Horeweg N, van der Aalst CM, Vliegenthart R, Zhao Y, Xie X, Scholten ET, et al. Volumetric computed tomography screening for lung cancer: three rounds of the NELSON trial. Eur Respir J. 2013 Dec;42(6):1659-67.

11. Oudkerk M, Heuvelmans MA. Screening for lung cancer by imaging: the Nelson study. JBR-BTR. 2013 May-Jun;96(3):163-6.

12. Horeweg N, van Rosmalen J, Heuvelmans MA, van der Aalst CM, Vliegenthart R, Scholten ET, et al. Lung cancer probability in patients with CT-detected pulmonary nodules: a prespecified analysis of data from the NELSON trial of low-dose CT screening. Lancet Oncol. 2014 Oct 1.

13. Horeweg N, van der Aalst CM, Thunnissen E, Nackaerts K, Weenink C, Groen HJ, et al. Characteristics of lung cancers detected by computer tomography screening in the randomized NELSON trial. Am J Respir Crit Care Med. 2013 Apr 15;187(8):848-54.

14. Aberle DR, Adams AM, Berg CD, Black WC, Clapp JD, Fagerstrom RM, et al. Reduced lung-cancer mortality with low-dose computed tomographic screening. N Engl J Med. 2011 Aug 4;365(5):395-409.

15. Aberle DR, Berg CD, Church TR, Fagerstrom RM, Galen B, et al. The National Lung Screening Trial: overview and study design. Radiology. 2011 Jan;258(1):243-53.

16. Mazzone P. The rationale for, and design of, a lung cancer screening program. Cleve Clin J Med. 2012 May;79(5):337-45.

17. Pedersen JH, Ashraf H, Dirksen A, Bach K, Hansen H, Toennesen P, et al. The Danish randomized lung cancer CT screening trial--overall design and results of the prevalence round. J Thorac Oncol. 2009 May;4(5):608-14.

18. Mahajan AK, Patel S, Hogarth DK, Wightman R. Electromagnetic navigational bronchoscopy: an effective and safe approach to diagnose peripheral lung lesions unreachable by conventional bronchoscopy in high-risk patients. J Bronchology Interv Pulmonol. 2011 Apr;18(2):133-7.

19. Seijo LM, de Torres JP, Lozano MD, Bastarrika G, Alcaide AB, Lacunza MM, et al. Diagnostic yield of electromagnetic navigation bronchoscopy is highly dependent on

the presence of a Bronchus sign on CT imaging: results from a prospective study. Chest. 2010 Dec;138(6):1316-21.

20. Chen A, Pastis N, Furukawa B, Silvestri GA. The effect of respiratory motion on pulmonary nodule location during electromagnetic navigation bronchoscopy. Chest. 2015 May;147(5):1275-81.

21. Dooms C, Muylle I, Yserbyt J, Ninane V. Endobronchial ultrasound in the management of nonsmall cell lung cancer. Eur Respir Rev. 2013 Jun 01;22(128):169-77.

22. Zeng H, McWilliams A, Lam S. Optical spectroscopy and imaging for early lung cancer detection: a review. Photodiagnosis Photodyn Ther. 2004 Sep;1(2):111-22.

23. Tan KM, Shishkov M, Chee A, Applegate MB, Bouma BE, Suter MJ. Flexible transbronchial optical frequency domain imaging smart needle for biopsy guidance. Biomed Opt Express. 2012 Aug 1;3(8):1947-54.

24. Hariri LP, Villiger M, Applegate MB, Mino-Kenudson M, Mark EJ, Bouma BE, et al. Seeing beyond the bronchoscope to increase the diagnostic yield of bronchoscopic biopsy. Am J Respir Crit Care Med. 2013 Jan 15;187(2):125-9.

25. Hariri LP, Mino-Kenudson M, Mark EJ, Suter MJ. In vivo optical coherence tomography: the role of the pathologist. Arch Pathol Lab Med. 2012 Dec;136(12):1492-501.

26. Hariri LP, Mino-Kenudson M, Lanuti M, et al. Diagnosing lung carcinomas with optical coherence tomography. Ann Am Thorac Soc. 2015 Feb;12(2):193-201.

27. Hariri LP, Mino-Kenudson M, Applegate MB, Mark EJ, Tearney GJ, Lanuti M, et al. Toward the guidance of transbronchial biopsy: identifying pulmonary nodules with optical coherence tomography. Chest. 2013 Oct;144(4):1261-8.

28. Spliethoff JW, Evers DJ, Klomp HM, van Sandick JW, Wouters MW, Nachabe R, et al. Improved identification of peripheral lung tumors by using diffuse reflectance and fluorescence spectroscopy. Lung Cancer. 2013 May;80(2):165-71.

29. Fawzy YS, Petek M, Tercelj M, Zeng HS. In vivo assessment and evaluation of lung tissue morphological and physiological changes from non-contact endoscopic reflectance spectroscopy for improving lung cancer detection. Journal of Biomedical Optics. 2006 Jul-Aug;11(4):-.

30. Bard MP, Amelink A, Skurichina M, Noordhoek Hegt V, Duin RP, Sterenborg HJ, et al. Optical spectroscopy for the classification of malignant lesions of the bronchial tree. Chest. 2006 Apr;129(4):995-1001.

31. Magee ND, Villaumie JS, Marple ET, Ennis M, Elborn JS, McGarvey JJ. Ex vivo diagnosis of lung cancer using a Raman miniprobe. J Phys Chem B. 2009 Jun 11;113(23):8137-41.

32. Huang Z, McWilliams A, Lui H, McLean DI, Lam S, Zeng H. Near-infrared Raman spectroscopy for optical diagnosis of lung cancer. Int J Cancer. 2003 Dec 20;107(6):1047-52.

33. Short MA, Lam S, McWilliams A, Zhao J, Lui H, Zeng H. Development and preliminary results of an endoscopic Raman probe for potential in vivo diagnosis of lung cancers. Opt Lett. 2008 Apr 1;33(7):711-3.

34. Bard MP, Amelink A, Hegt VN, Graveland WJ, Sterenborg HJ, Hoogsteden HC, et al. Measurement of hypoxia-related parameters in bronchial mucosa by use of optical spectroscopy. Am J Respir Crit Care Med. 2005 May 15;171(10):1178-84.

35. Aerts JG, Amelink A, van der Leest C, Hegmans JP, Hemmes A, den Hamer B, et al. HIF1a expression in bronchial biopsies correlates with tumor microvascular saturation determined using optical spectroscopy. Lung Cancer. 2007 Sep;57(3):317-21.

36. Amelink A, Sterenborg HJ, Bard MP, Burgers SA. In vivo measurement of the local optical properties of tissue by use of differential path-length spectroscopy. Opt Lett. 2004 May 15;29(10):1087-9.

37. Kitaoka H, Takaki R, Suki B. A three-dimensional model of the human airway tree. J Appl Physiol (1985). 1999 Dec;87(6):2207-17.

38. Kitaoka H. Welcome to 4D Respirology. [cited 2014-2015]; Available from: http://www7b.biglobe.ne.jp/~lung4cer/indexEng.html.

39. Evers DJ, Nachabe R, Klomp HM, van Sandick JW, Wouters MW, Lucassen GW, et al. Diffuse reflectance spectroscopy: a new guidance tool for improvement of biopsy procedures in lung malignancies. Clin Lung Cancer. 2012 Nov;13(6):424-31

8

General discussion

General discussion

The general concept in surgical oncology has always been resection of the diseased tissue while preserving maximum function. For many malignancies, incomplete tumor resection is one of the main risk factors for local tumor recurrence[1-5]. Intra-operative imaging could prevent incomplete resection or contribute to early detection of tumor residue. Early detection of incomplete tumor resection (tumor residue) allows for early re-excision. In case of detection of positive surgical margins during the primary surgery would even allow for immediate resection of the residual tumor. Chapter two describes the use of an intra-operative fluorescence camera and demonstrates the detection of residual tumor deposits during breast cancer surgery. In the same chapter, two major disadvantages are discussed. The first being the inability to differentiate between a superficial tumor deposit and a stronger more compact deposit at a certain depth, this problem is caused by optical scattering. The second problem is that a contrast agent is designed to target only one type of tissue: in chapter two tumor was targeted. When the tumor is in close relation to vital structures, it could be desirable to visualize both tumor and vital surrounding structures to minimize accidental damage to vital structures like nerves or blood vessel. Both these problem were assessed in chapter three using another technique: Photoacoustic imaging. Photoacoustic imaging (PAI) relies on the thermal expansion after optical absorption. As optical absorption is tissue specific, PAI benefits from the optical tissue contrast. The thermal expansion creates an ultrasound wave, which is not disturbed by optical scattering. Combined with an array of US sensors, the source of the signal could be determined in three dimensions, even when covered with a layer of optical scattering tissue. PAI could therefore differentiate between superficial and deeper laying sources. Visualization of both tumor (melanoma) and blood vessels was also demonstrated. This was possibly due to the difference in absorption spectrum between hemoglobin and melanin. The difference in absorption spectrum results in specific increase or decrease of the PAI signal when illuminating with light of various wavelengths.

Although PAI provides three dimensional imaging and visualizes both tumor and blood vessels, three major disadvantages were faced. First, the image acquisition is time consuming, especially in multispectral mode (acquisition with light of several wavelengths successively). Furthermore, the system needs considerable physical space and the centimeters big ultrasound detector needs acoustical contact with the tissue, disturbing the surgical procedure. Third, the image quality depends on the optical absorption of the tissue of interest which makes imaging of tissue with little optical absorption problematic. Chapter three describes the imaging of melanoma and hemoglobin, two strong optical absorbers. To visualize tissues with lower optical absorption with PAI, contrast agents may be needed. As in fluorescence imaging, contrast agents pose regulatory issues and are subject to pharmacodynamics in the body. A technique that could identify several tissues based on intrinsic optical differences could overcome these issues. In chapter 4-8, tissue identification based on intrinsic differences in absorption and scattering is explored. As

demonstrated in this thesis, DRS is able to identify both tumor and surrounding tissue. The technique requires only small, micrometer scale, fiber optics which could be integrated into several surgical tools. The acquisition is near real time. In this perspective, DRS could overcome the three disadvantages of PAI. However, the technique does not provide spatial information. The measured volume is analyzed as a point measurement. DRS seems therefore suited for tissue identification rather than finding and localizing targets.

This thesis provides an evaluation of three techniques for intraoperative imaging on the ability to identify both tumor and surrounding vital structures. The dependency on other techniques to find and localize the target tissue, and the constraints for integration in clinical surgery are included in the evaluation. Imaging techniques discussed are: near infra-red fluorescence (NIRF) imaging, Photoacoustic imaging (PAI) and Diffuse Reflectance Spectroscopy (DRS). These three approaches did not acquire broad clinical acceptance yet. In this chapter we try to discuss their potential and constraints and offer future prospective on optical tissue identification for surgical application.

Evaluation of the imaging modalities

NIRF imaging

I Identification of both tumor and surrounding tissue. The visualization of both tumor and vital structures can be achieved in multiple ways. The tumor can be stained either with molecular targeted fluorescent molecules[6-8] or by natural accumulation[9-11]. As shown in chapter two, the fluorescence signal is a grayscale image which could be visualized as pseudo color overlay on a simultaneous acquired color image. The overlay supplies information about the relation to surrounding structures. Imaging two fluorescence agents in one image allows targeting two different tissues at the same time. Using different molecules to target the tumor and vital structures separately, would allow for classification based on the spectral differences between the different contrast agents. Spectral discrimination of multiple NIRF contrast agents is technically possible but makes the setup technically complex. The use of multiple contrast agents increases the complexity in pharmacokinetics and regulatory aspects.

A barrier for rapid clinical application of contrast agents is regulatory approval. Today, only the non-targeted molecules like indocyanine green (ICG) and fluorescein are clinically approved by The European Medicines Agency (EMA), and the US Food and Drug Administration (FDA)[12]. Clinical approval for targeted agents is crucial for widespread intra-operative use of fluorescence imaging.

Finding and localizing targets. Chapter two describes a proof-of-principle study; surgery was performed on breast phantoms with fluorescent inclusions to simulate tumor. The phantom was constructed to mimic the optical properties of breast tissue. Tumor mimicking

9

inclusions were recognized up to 2 cm of depth. However, the translation into clinical practice might reveal lower penetration depths. The background signal in this phantom study was absent. In patients, the contrast agent is administered and accumulates in the target area, leaving a background signal in the body tissue. Furthermore, the background signal is not expected to be perfectly homogeneous, making the recognition of hot spots more challenging. Therefore, the presented sampling depth during in vivo measurements in patients is expected to be lower compared to this phantom study. This means that for tumor or lymph node localization, additional techniques are necessary for tumors deeper than the penetration depth. Demands on the precision of additional techniques for navigation/orientation are relatively mild as a sampling depth of 1-2 cm is enough for guidance in the proximity of the target. The NIRF system delivers excellent overview, especially when combining the fluorescent signal with an RGB image of the surgical field.

Integration into surgery. In this thesis (Chapter two), a NIRF camera system for intra-operative use was evaluated for integration into clinical practice. The resection of the inclusion under NIRF guidance was feasible and intuitive. The conventional surgical procedure is affected by the presence of an extra device in the surgical area which has to be sterilely draped. Furthermore, the surgical lights were shut off during imaging. The overlay image is easy to correlate to the surgical field of view. The integration into surgery is supported by successful surgical procedures described elsewhere[6], using the same camera system.

Photoacoustic imaging

Identification of both tumor and surrounding tissue. PAI relies on the detection of ultrasound caused by thermal expansion after optical absorption. Optical absorption is tissue dependent and a function of the wavelength. In multispectral PAI, tissue is differentiated based on the wavelength specific signal intensity after illumination with pulsed light. In chapter three, both tumor (melanoma) and vital structures (blood vessel) could be visualized and identified using this principle. However, both melanin and hemoglobin are strong optical absorbers. To visualize a tumor with lower optical absorption, optical contrast agents may be necessary. Contrast agents in PAI can be dyes already used in clinical practice, such as methylene blue and ICG[13]. Experimental nanoparticles[14,15], with extreme optical absorption and specific absorption spectra, are suggested since 2001 but did not gain clinical approval so far. The use of NIRF contrast agents for photoacoustic imaging would enable hybrid imaging with NIRF and PAI simultaneously. PAI using NIRF contrast agents has been demonstrated in experimental animals, targeting integrin $\alpha v \beta 3$ (expressed in tumor cells as well as in neovasculature).

Photoacoustic imagers are equipped with a highly sensitive ultrasound transducer. The use of this transducers to perform conventional ultrasound imaging allows overlay imaging of PAI and conventional ultrasound in the same imaging planes; as shown in chapter three. The combination of PAI and conventional ultrasound image (hybrid PAI) makes the

identification of both tumor and surrounding tissue possible.

Finding and localizing targets. PAI, with an array ultrasound transducer delivers a two dimensional - or even three dimensional overview. The penetration depth depends on the optical absorption of the tissue and the ultrasound attenuation. With a common sampling depth of one to several centimeters, PAI could be used to localize targets.

Integration into surgery. Several aspects of PAI interfere with standard surgery. First, the technique requires acoustical contact with the tissue of interest, comparable to conventional intra-operative ultrasound. In addition, the pulsed laser illumination is commonly infra-red, to utilize the low body absorption in this wavelength region. However, the use of pulsed infra-red laser light might require laser safety regulation (e.g. laser safety goggles), which affects normal surgical procedure. Thirdly, the use of multispectral PAI requires consecutive illumination per wavelength per slice. Multispectral three-dimensional PAI is therefore time-consuming which hampers swift surgery.

Diffuse reflectance spectroscopy

Identification of both tumor and surrounding tissue. Tissue identification in DRS is based on differences in optical absorption and scattering; both are tissue properties and depending on the composition of the tissue. DRS was used to identify tumor tissue in colon in this thesis and breast[16-19], liver[20-22] and lung[23-25] elsewhere. The healthy surrounding structures were often included in the classification algorithm. The identification of peripheral nerve using DRS is elaborated in this thesis. Tissue identification without the need for additional contrast agents gives DRS the potential to identify both tumor, or other target tissue, and vital surrounding structures.

Furthermore, the optical contrast agents used in NIRF imaging (fluorescence agents) and PAI (strong optical absorbers) could be detected using DRS. This makes it possible to combine the imaging techniques, without the use composed (hybrid) contrast agents. In hybrid contrast agents, agents for different modalities are linked so that the combination is visible on both modalities. Example of a hybrid contrast agent is a PET tracer bound to a fluorescent agent[26].

Finding and localizing targets. DRS overcomes several problems faced with fluorescence imaging and PAI: it is fast, does not rely on contrast agents and identifies both malignant and benign structures. However, it does not provide spatial information. Finding and localizing targets should therefore depend on other methods. Conventionally, finding targets is based on palpation, vision, and (pre-operative) imaging.

Integration into surgery. Some intrinsic drawbacks such as the requirement for tissue contact and the cable connection to the spectrometers may interfere with standard surgical procedure. However, multiple daily used surgical tools share these requirements. Examples are intra-operative ultrasound, radio frequent dissection devices (harmonic

scapel, Ligasure and Tissuelink dissecting sealer) and water jet dissection tools. Even simple electro-coagulation tools, used in almost every surgical procedure require tissue contact and a wire connection. This proofs that if such a tool delivers clear benefits, the requirements for tissue contact and the cable connection will not prevent broad clinical acceptance and daily use.

Application

As discussed in chapter two, the fluorescence camera can be used to localize spots of high concentrations of contrast agents, corresponding to residual tumor deposits. The resolution of this optical technique goes up to micrometer scale but strongly diminish with increasing overlying scattering tissue. The localization of superficial sources therefore seems the best suited application.

Photoacoustic imaging where laser illumination is integrated into the ultrasound receiver, like the setup used in chapter three enables hybrid ultrasound and PAI. As explained in chapter three, information about optical absorption of the tissue could be combined with the ultrasound image to create an overlay image. This approach shares similarities with duplex ultrasound where ultrasound imaging is combined with Doppler for flow measurements. In clinical practice, the ultrasound is used to localize vessels and the duplex mode is switched on selectively. We showed that the PAI signal could be detected in depth without being disturbed by optical scattering. The ability to visualize targets at several depths makes this technique suited for guidance in (surgical) biopsy or surgical planning. Simultaneous imaging of blood vessels and the combination with conventional ultrasound is most valuable when the target is in close relation to vital structures.

For DRS, we showed that the possibility to identify multiple malignant and benign tissues, including vital structures likes nerves. A possible application of DRS could be during colorectal surgery, to confirm tissue type or to alert in case of nervous tissue. Colorectal surgery poses problems of compromised visual feedback and close relation of tumor to nervous structures, especially for oncology in the pelvis. We showed that DRS is able to discriminate colorectal cancer from healthy surrounding tissue and peripheral nerves could be identified. In chapter eight we discussed the application of the DRS technique into tools on millimeter scale. The scale of the optical fibers in DRS allows for integration into various surgical tools. With DRS integrated, these tools could read and identify the tissue before manipulation, dissection or biopsy.

Correlation with pre-operative imaging

Optical tissue identification techniques in general are considered safe, fast, inexpensive, make use of non-ionizing radiation and enable real-time anatomical and functional imaging[27]. Optical intra-operative imaging shows interesting and unique features including high resolution and the ability to visualize metabolic and physiologic parameters

in (near) real time[28]. Despite these advantages over conventional (anatomical) imaging, a considerable part of the published research focuses on the identification or anatomy which is well imaged using conventional techniques. For example, optical intra-operative imaging was used to identify and locate lymph nodes[29-35] and liver metastases[9,11]. These applications might be chosen because information from pre-operative imaging was difficult to translate to the surgical field during surgery.

One of the problems depicted in chapter two was the inability of NIRF imaging to determine the depth of the origin of the signal; scattering makes it impossible to distinguish between a large superficial source and a stronger, more compact source at depth. However, pre-operative imaging tells us the size, shape and orientation of the lesion. When this information is available during the procedure, differentiation between superficial of deeper laying sources based on optical imaging alone is no longer relevant.

An increasing proportion of the patients scheduled for surgery is pre-operatively imaged using three-dimensional CT or MR imaging. Ideally, the information of prior imaging should be made available during surgery in a way that it is easy to interpret and relate to in the surgical field. When this integration is accomplished, the focus in intra-operative optical imaging could shift from anatomical imaging and orientation to features unique for optical imaging like functional imaging, high resolution and tissue classification based on histological composition. In such way, the patient could benefit from 'best of both worlds'.

To facilitate synergy with surgical navigation, the camera could be mounted on an intra-operative X-ray imaging (C-arm) and tracked with surgical navigation. C-arm systems with integrated optical tracking for surgical navigation are described recently[36]. The tracked C-arm allows automated registration of the patient's anatomy as imaged with CT or MRI to the patient's position on the table. With the NIRF camera integrated, surgical navigation could combine the intra-operative optical imaging with pre-operative MRI or CT. Combining the specificity and resolution of optical imaging with penetration depth and undistorted body imaging of CT/MRI.

The combination of a hybrid PAI system with surgical navigation, as already presented for conventional ultrasound alone[37], could ease the localization of deeper lying targets. Surgical navigation tracks the patient and surgical tools, visualizing the relation between these tools and patients anatomy based on pre-operative MR- or CT imaging.

For DRS, the main problem is the lack of spatial information. Surgical navigation facilitates localization of targets and could also log the DRS tissue identification and link this to anatomical structures. Combining these systems, each DRS measurement correlates to a physical location. The combination creates a system that is able to supply the surgeon with spatial anatomical data based on prior CT- and MR imaging combined with real time tissue identification and analyzes of metabolic parameters like oxygen saturation and concentration of molecules like FAD (flavin adenine dinucleotide) and NADH (reduced nicotinamide adenine dinucleotide)

Surgical devices with DRS

The hardware requirements for DRS in surgical devices are the incorporation of two or three fiber optical wires, typically 50 μm in radius (core) and less than 1 mm width. Integration of the DRS technique into surgical devices for dissections makes sense: In case of incomplete tumor resection, the surgical tool was at some point in contact with malignant cells. Therefore, tissue identification at the tip of the instrument could detect incomplete resection. Early detection of positive margins allows re-excision during the surgical procedure. It would be revolutionary when the dissection tool warns for nearby tumor cells and in therefore preventing incomplete resection. Analogous to this, detection of close proximity to nerves, vessels, ureters or the common bile duct could prevent unintended transection of these vital structures. Minimal interference with the surgical procedure is achieved when the DRS-sensing works continuous and real time during the use of the instrument.

In another approach, the tissue identification is available on demand and either incorporated into existing surgical devices or as separate pointing device. Then, the demand for continuous and real-time measurement is less strict. An example of integration into a surgical device is a smart optical stapler: After placing and closure of the stapler, measurements determine the presence of tumor before firing the stapler, allowing reposition of the device before creating tumor positive resection margins. In addition, other parameters, such as oxygen saturation could be analyzed to define an adequate resection plane.

Eventually, image guided surgery will focus on the unique properties of optical imaging: the ability to visualize metabolic and physiologic parameters, high resolution and real time tissue identification. Optical techniques for anatomical imaging and finding targets would become less interesting due to a higher level of integration of conventional (pre-operative) anatomical imaging techniques like CT, ultrasound or MR.

References

1. Park CC, Mitsumori M, Nixon A, Recht A, Connolly J, Gelman R, et al. Outcome at 8 years after breast-conserving surgery and radiation therapy for invasive breast cancer: influence of margin status and systemic therapy on local recurrence. Journal of Clinical Oncology. 2000;18(8):1668-75.

2. Nagtegaal ID, Marijnen CA, Kranenbarg EK, van de Velde CJ, van Krieken JHJ, Investigators PRCtCC. Circumferential margin involvement is still an important predictor of local recurrence in rectal carcinoma: not one millimeter but two millimeters is the limit. The American journal of surgical pathology. 2002;26(3):350-7.

3. Hirokawa F, Hayashi M, Asakuma M, Shimizu T, Inoue Y, Uchiyama K. Risk factors and patterns of early recurrence after curative hepatectomy for hepatocellular carcinoma. Surgical oncology. 2016;25(1):24-9.

4. Blewett C, Miller J, Ramlawi B, Young J, Urschel J. Local recurrence after total or subtotal esophagectomy for esophageal cancer. Journal of experimental & clinical cancer research: CR. 2001;20(1):17-9.

5. Kreike B, Hart AA, van De Velde T, Borger J, Peterse H, Rutgers E, et al. Continuing risk of ipsilateral breast relapse after breast-conserving therapy at long-term follow-up. International Journal of Radiation Oncology Biology Physics. 2008;71(4):1014-21.

6. Van Dam GM, Themelis G, Crane LM, Harlaar NJ, Pleijhuis RG, Kelder W, et al. Intraoperative tumor-specific fluorescence imaging in ovarian cancer by folate receptor-[alpha] targeting: first in-human results. Nature medicine. 2011;17(10):1315-9.

7. Verbeek FP, van der Vorst JR, Tummers QR, Boonstra MC, de Rooij KE, Löwik CW, et al. Near-infrared fluorescence imaging of both colorectal cancer and ureters using a low-dose integrin targeted probe. Annals of surgical oncology. 2014;21(4):528-37.

8. Warram JM, de Boer E, van Dam GM, Moore LS, Bevans SL, Walsh EM, et al. Fluorescence imaging to localize head and neck squamous cell carcinoma for enhanced pathological assessment. The Journal of Pathology: Clinical Research. 2016.

9. van der Vorst JR, Schaafsma BE, Hutteman M, Verbeek FP, Liefers GJ, Hartgrink HH, et al. Near-infrared fluorescence-guided resection of colorectal liver metastases. Cancer. 2013;119(18):3411-8.

10. Kelder W, Nimura H, Takahashi N, Mitsumori N, Van Dam G, Yanaga K. Sentinel node mapping with indocyanine green (ICG) and infrared ray detection in early gastric cancer: an accurate method that enables a limited lymphadenectomy. European Journal of Surgical Oncology (EJSO). 2010;36(6):552-8.

11. Ishizawa T, Fukushima N, Shibahara J, Masuda K, Tamura S, Aoki T, et al. Real-time identification of liver cancers by using indocyanine green fluorescent imaging. Cancer. 2009;115(11):2491-504.

12. De Boer E, Harlaar N, Taruttis A, Nagengast W, Rosenthal E, Ntziachristos V, et al. Optical innovations in surgery. British Journal of Surgery. 2015;102(2):e56-e72.

13. Luke GP, Yeager D, Emelianov SY. Biomedical applications of photoacoustic imaging with exogenous contrast agents. Annals of biomedical engineering. 2012;40(2):422-37.

14. Manohar S, Ungureanu C, Van Leeuwen TG. Gold nanorods as molecular contrast agents in photoacoustic imaging: the promises and the caveats. Contrast media & molecular imaging. 2011;6(5):389-400.

15. Oraevsky AA, Karabutov AA, Savateeva EV, editors. Enhancement of optoacoustic tissue contrast with absorbing nanoparticles. European Conference on Biomedical Optics; 2001: International Society for Optics and Photonics.

16. Brown JQ, Bydlon TM, Richards LM, Yu B, Kennedy SA, Geradts J, et al. Optical assesssment of tumor resection margins in the breast. Selected Topics in Quantum Electronics, IEEE Journal of. 2010;16(3):530-44.

17. Nachabé R, Evers DJ, Hendriks BH, Lucassen GW, van der Voort M, Rutgers EJ, et al. Diagnosis of breast cancer using diffuse optical spectroscopy from 500 to 1600 nm: comparison of classification methods. Journal of biomedical optics. 2011;16(8):087010-2.

18. de Boer L, Molenkamp B, Bydlon T, Hendriks B, Wesseling J, Sterenborg H, et al. Fat/water ratios measured with diffuse reflectance spectroscopy to detect breast

tumor boundaries. Breast cancer research and treatment. 2015;152(3):509-18.

19. de Boer LL, Hendriks BH, van Duijnhoven F, Peeters-Baas M-JTV, Van de Vijver K, Loo CE, et al. Using DRS during breast conserving surgery: identifying robust optical parameters and influence of inter-patient variation. Biomedical Optics Express. 2016;7(12):5188-200.

20. Evers D, Nachabé R, Hompes D, van Coevorden F, Lucassen G, Hendriks B, et al. Optical sensing for tumor detection in the liver. European Journal of Surgical Oncology (EJSO). 2012.

21. Nachabé R, Evers DJ, Hendriks BH, Lucassen GW, van der Voort M, Wesseling J, et al. Effect of bile absorption coefficients on the estimation of liver tissue optical properties and related implications in discriminating healthy and tumorous samples. Biomed Opt Express. 2011;2(3):600-14.

22. Tanis E, Spliethoff J, Evers D, Langhout G, Snaebjornsson P, Prevoo W, et al. Real-time in vivo assessment of radiofrequency ablation of human colorectal liver metastases using diffuse reflectance spectroscopy. European Journal of Surgical Oncology (EJSO). 2016;42(2):251-9.

23. Spliethoff JW, Evers DJ, Klomp HM, van Sandick JW, Wouters MW, Nachabe R, et al. Improved identification of peripheral lung tumors by using diffuse reflectance and fluorescence spectroscopy. Lung cancer. 2013.

24. Spliethoff JW, Prevoo W, Meier MA, de Jong J, Klomp HM, Evers DJ, et al. Real-time in vivo tissue characterization with diffuse reflectance spectroscopy during transthoracic lung biopsy: a clinical feasibility study. Clinical cancer research. 2016;22(2):357-65.

25. Evers DJ, Nachabé R, Klomp HM, van Sandick JW, Wouters MW, Lucassen GW, et al. Diffuse reflectance spectroscopy: a new guidance tool for improvement of biopsy procedures in lung malignancies. Clinical lung cancer. 2012;13(6):424-31.

26. Zhang Y, Hong H, Severin GW, Engle JW, Yang Y, Goel S, et al. ImmunoPET and near-infrared fluorescence imaging of CD105 expression using a monoclonal antibody dual-labeled with 89Zr and IRDye 800CW. American journal of translational research. 2012;4(3):333.

27. Keereweer S, Kerrebijn JD, Van Driel PB, Xie B, Kaijzel EL, Snoeks TJ, et al. Optical image-guided surgery—where do we stand? Molecular Imaging and Biology. 2011;13(2):199-207.

28. Solomon M, Liu Y, Berezin MY, Achilefu S. Optical imaging in cancer research: basic principles, tumor detection, and therapeutic monitoring. Medical Principles and Practice. 2011;20(5):397-415.

29. Kitai T, Inomoto T, Miwa M, Shikayama T. Fluorescence navigation with indocyanine green for detecting sentinel lymph nodes in breast cancer. Breast cancer. 2005;12(3):211-5.

30. Tagaya N, Yamazaki R, Nakagawa A, Abe A, Hamada K, Kubota K, et al. Intraoperative identification of sentinel lymph nodes by near-infrared fluorescence imaging in patients with breast cancer. The American Journal of Surgery. 2008;195(6):850-3.

31. Hirche C, Murawa D, Mohr Z, Kneif S, Hünerbein M. ICG fluorescence-guided sentinel node biopsy for axillary nodal staging in breast cancer. Breast cancer research and treatment. 2010;121(2):373-8.

32. van der Vorst JR, Schaafsma BE, Verbeek FP, Keereweer S, Jansen JC, van der Velden L-A, et al. Near-infrared fluorescence sentinel lymph node mapping of the oral cavity in head and neck cancer patients. Oral oncology. 2013;49(1):15-9.

33. Brouwer OR, Klop WMC, Buckle T, Vermeeren L, van den Brekel MW, Balm AJ, et al. Feasibility of sentinel node biopsy in head and neck melanoma using a hybrid radioactive and fluorescent tracer. Annals of surgical oncology. 2012;19(6):1988-94.

34. Crane LM, Themelis G, Buddingh KT, Harlaar NJ, Pleijhuis RG, Sarantopoulos A, et al. Multispectral real-time fluorescence imaging for intraoperative detection of the sentinel lymph node in gynecologic oncology. JoVE (Journal of Visualized Experiments). 2010(44):e2225-e.

35. Troyan SL, Kianzad V, Gibbs-Strauss SL, Gioux S, Matsui A, Oketokoun R, et al. The FLARE™ intraoperative near-infrared fluorescence imaging system: a first-in-human clinical trial in breast cancer sentinel lymph node mapping. Annals of surgical oncology. 2009;16(10):2943-52.

36. Elmi-Terander A, Skulason H, Söderman M, Racadio J, Homan R, Babic D, et al. Surgical Navigation Technology Based on Augmented Reality and Integrated 3D Intraoperative Imaging: A Spine Cadaveric Feasibility and Accuracy Study. Spine. 2016;41(21):E1303.

37. Marks L, Young S, Natarajan S. MRI–ultrasound fusion for guidance of targeted prostate biopsy. Current opinion in urology. 2013;23(1):43.

9

Curriculum Vitae

Curriculum Vitae

Gerrit Cornelis Langhout

Ervaring

2018	**Basisarts ouderengeneeskunde**, *de Rijnhoven*, Harmelen
2017	**Arts-assistent heelkunde** (ANIOS), *Martini ziekenhuis*, Groningen
2016-2017	**Arts-onderzoeker** heelkunde, *Nederlands Kanker Instituut, Antoni van Leeuwenhoek ziekenhuis,* Amsterdam
2015-2016	**Arts-assistent heelkunde** (ANIOS), *Albert Schweitzer ziekenhuis*, Dordrecht
2014-2015	**Arts-assistent snijdende specialismen** (ANIOS), *Antoni van Leeuwenhoek ziekenhuis*, Amsterdam
2012-2014	**Arts-onderzoeker** heelkunde, *Nederlands Kanker Instituut, Antoni van Leeuwenhoek ziekenhuis*, Amsterdam
2010-2012	**Teach the teacher cursus**, assistent, *Wenckebach instituut,* Groningen.
2006-2009	**Student assistent**, *Universiteit Twente*, Enschede
	Cardiovasculair systeem, Neurofysiologie, Optische beeldvorming van het maagdarmkanaal, Histopathologie van nier en urinewegen, Introductie in Matlab, Lichamelijk onderzoek
2006-2007	**Student assistent**, *Skillslab Technische Geneeskunde,* Enschede
2011-2014	**Zelfstandig ondernemer**, Langhout Site Deployment. (KvK 51554526)
	Ondersteuning (technische productie) op festivals, concerten, tv-shows en andere evenementen.
	Vrienden van Amstel, Symphonica in Rosso, Groots met een zachte G, Troonswisseling 2013, the Voice of Holland, the Wall (Pink Floyd), Opening Rijksmuseum, Gouden loekie, 3FM Serious Request

Onderwijs

2008-2012	**Master Geneeskunde**, *Rijksuniversiteit Groningen*, BIG registratie: 69916423001.
2007-2012	**Master Technische Geneeskunde**, *Universiteit Twente*, Enschede.
2007 en 2011	**Technische stages**, Radiotherapie en Medische oncologie, *Universitair Medisch Centrum Groningen.*
	Onderwerp: *Tumor respons evaluatie in GIST tumoren na imatinib behandeling met behulp van PET; a 3D spherial approach.*
2007-2008	**Pre–Master Geneeskunde**, *Rijksuniversiteit Groningen*, Groningen.
2004-2007	**Bachelor Technische Geneeskunde** Cum Laude, *Universiteit Twente*, Enschede.
	Onderwerp bachelor thesis: *Haptic feedback in navigation for neurosurgery.*
1998-2004	**VWO**, *Fivelcollege*, Delfzijl.
2012	**Master thesis**, *Antoni van Leeuwenhoek*, afdeling chirurgie en Universiteit Twente, BMPI, Amsterdam en Enschede
	title: *Tumor specific photoacoustic imaging of lymph nodes.*
	Prof. Dr. T.J.M. Ruers, Dr. S. Manohar, Prof. Dr. H. Zwart, MSc. D.J. Grootendorst, Drs. A.G. Lovink

Cursussen en certificaten

2015	**Advanced Trauma Life Support** (ATLS), *Stichting ATLS*, Tilburg.
2014	**Fundamental Critical Care Support** (FCCS), *Nederlandse Vereniging voor Intensive Care* (NVIC), Houten.
2013	**Good Clinical Practice** (GCP-WMO), EMWO certified, *EMWO/NKI-AVL*, Amsterdam.
2011	**Artikel 9**, *Rijksuniversiteit Groningen*, Groningen.
2007	**Stralingshygiene niveau 3**, *Radboud Universiteit*, Nijmegen.

Sportprestaties

2005	**Nederlands kampioen short-track**, estafette ploeg, Senior men
2002 en 2003	**Clubkampioen wielrennen**, junioren, *Noordelijke Wielervereniging Groningen*
2002-2003	**KNSB Jong Oranje** short-track
2001	**Nederlands kampioen short-track** schaatsen, junior C
1998	**Baanrecord**, langebaan schaatsen, Kardinge, Groningen

Interesses

Zeilen, Orion 20 kajuitzeilboot

Windsurfen en mijn surfbusje (oldtimer) rijdend houden

Articles

2018   **In vivo nerve identification in head and neck surgery using diffuse reflectance spectroscopy**

Laryngoscope Investigative Otolaryngology, GC Langhout, KFD Kuhlmann, ... , TJM Ruers

2018   **Nerve detection during surgery: Optical spectroscopy for peripheral nerve localization**

Laser Med Sci 2018, GC Langhout, KFD Kuhlmann, ... , TJM Ruers.

2017   **Nerve detection using optical spectroscopy, an evaluation in four different models: in human and swine, in-vivo and post mortem**

LiSM 2017, GC Langhout, TM Bydlon, …, TJM Ruers

2017   **Optimal endobronchial tool sizes for targeting lung lesions based on 3D modeling**

PLOS One 2017, TM Bydlon, GC Langhout, F Lalezari, K Hartmink, …, TJM Ruers

2015   **Nerve detection with optical spectroscopy for regional anesthesia procedures**

JoTM 2015, B.H.W. Hendriks, A.J.R. Balthasar, ... , G.C. Langhout, G-J van Geffen

2015   **Real-time in vivo assessment of radiofrequency ablation of human colorectal liver metastases using diffuse reflectance spectroscopy**,

EJSO 2015, E. Tanis, J.W. Spliethoff, D.J. Evers, G.C. Langhout, ... , T.J.M. Ruers

2015   **Differentiation of healthy and malignant tissue in colon cancer patients using optical spectroscopy: A tool for image-guided surgery**

LiSM 2015, G.C. Langhout, JW Spliethoff, ..., T.J.M. Ruers

2014   **Detection of melanoma metastases in resected human lymph nodes by non invasive multispectral photoacoustic imaging**

IJBI 2014, G.C. Langhout, DJ Grootendorst, ... , T.J.M. Ruers

2011   **Article: Near-Infrared Fluorescence (NIRF) Imaging in Breast-Conserving Surgery: Assessing Intraoperative Techniques in Tissue-Simulating Breast Phantoms**

EJSO 2010, R.G. Pleijhuis, G.C. Langhout, W. Helfrich, G. Themelis, ... , G.M. van Dam

Congress presentations

2016   Oral presentation: **Beeldvorming bij appendicitis acuta: recente landelijke cijfers**

Chirurgendagen symposium, Veldhoven, The Netherlands

2014   Oral presentation: **Colorectal cancer identified using optical spectroscopy**

ESSO, Liverpool, UK

2014   Poster presentation: **Colorectal cancer identified using optical spectroscopy**

ESMO, Madrid, Spain

2014   Oral presentation: **Dectecting nerves using diffuse optical spectroscopy during surgery**

Chirurgendagen symposium, Veldhoven, The Netherlands

2013   Poster presentation: **Differentiation of benign and malignant tissue in colon cancer patients using optical spectroscopy**

ESMO congress, Amsterdam, the Netherlands

2013	Oral presentation: **Application of optical spectroscopy to differentiate malignant from healthy colon tissue during surgery**
	Chirurgendagen symposium, Veldhoven, The Netherlands.
2013	Oral presentation: **Detection of tumor positive lymph nodes in melanoma patients using multispectral photoacoustic imaging**
	Chirurgendagen symposium, Veldhoven, The Netherlands
2012	Poster presentation: **Tumor specific imaging in human lymph nodes with photoacoustic imaging**
	ESSO 2012, Valencia, Spain
2010	Oral presentation: **Near-Infrared Fluorescence (NIRF) Imaging in Breast-Conserving Surgery: Assessing Intraoperative Techniques in Tissue-Simulating Breast Phantoms**
	ISCOMS 2010, Groningen, The Netherlands

Acknowledgements

2017	Article: **Diffuse reflectance spectroscopy as a tool for real-time tissue assessment during colorectal cancer surgery**
	J biomed Opt 2017, Elisabeth J. M. Baltussen, Petur Snaebjornsson, Susan G. Brouwer de Koning, ..., Theodoor J.M. Ruers.
2016	Article: **Real-time In Vivo Tissue Characterization with Diffuse Reflectance Spectroscopy during Transthoracic Lung Biopsy: A Clinical Feasibility Study**
	Clin Cancer Res 2016, Jarich W. Spliethoff, Warner Prevoo, ..., Theodoor J.M. Ruers.
2015	Acknowledgement for artwork (Article): **Een routine lokale infiltratie anesthesie als ongebruikelijke oorzaak voor trismus**
	Nederlands tijdschrift voor KNO 2015, J.F. Petersen, L.E. Smeele, A.J.M. Balm
2015	Contribution to book, **Frontiers in Biophotonics for Translational Medicine**: Chapter: Handheld Probe-Based Dual Mode Ultrasound/Photoacoustics for Biomedical Imaging, *Springer 2015 ISBN: 978-981-287-626-3 (Print) 978-981-287-627-0 (Online)*
2009	Acknowledgement in book, **Essentials of neurophysiology : basic concepts and clinical applications for scientists and engineers**
	M.J.A.M. van Putten, Springer / 2009 ISBN 3-540-69889-2

Dankwoord

Dankwoord

Dit onderzoek was niet mogelijk geweest zonder het vertrouwen dat de deelnemende patiënten hebben gesteld in het onderzoek. Allereerst wil ik dan ook alle patiënten bedanken die hebben deelgenomen aan de klinische studies waarop dit proefschrift is gestoeld. Naast de patiënten wil ik graag een aantal mensen in het bijzonder bedanken:

Prof. dr. Theo J.M. Ruers, promotor. Beste Theo, bedankt voor het vertrouwen om dit promotietraject met mij te willen starten. Uw gedrevenheid, enthousiasme zijn aanstekelijk. Van binnenuit heb ik kunnen meemaken hoe de onderzoeksgroep over de afgelopen jaren uitgroeide tot de multidisciplinaire, volwassen maar bovenal indrukkende groep die het nu is. Ik ben ontzetten bij dat ik bij u kan promoveren.

Prof. dr. Dick J.C.M. Sterenborg. Beste Dick, dank voor alle ondersteuning, begeleiding en sturing. Naast al je kennis, inzicht en ervaring heb ik je bijna jeugdig enthousiasme steeds aanstekelijk en inspirerend gevonden. Je energie is aanstekelijk.

Koert, je bent een voorbeeld. Ik waardeer je begeleiding, je bent eerlijk, kritisch en altijd opgewekt en opbouwend. Ik heb veel van je geleerd.

Prof. dr. Benno H.W. Hendriks. Beste Benno, bedankt voor de tijd, de betrokkenheid en in de inkijk bij Philips Research in Eindhoven. Je creativiteit, inzicht en technisch niveau, gecombineerd met een ontzettend praktische inslag heeft mij verwonderd en geïnspireerd.

Geachte leden van de promotiecommissie: Hartelijk dank voor uw interesse en tijd die u hebt genomen om dit proefschrift kritisch door te lezen en te beoordelen.

Ik bedank prof. dr. Go van Dam voor de kennismaking met het onderzoek. Binnen een hechte groep met Tim Buddingh, Lucie Crane, Niels Harlaar, Marleen van Oosten en Rick Pleijhuis besloot ik dat intra-operatieve optica het onderzoeksgebied is waarin ik verder wilde.

Diederik, op veel gebieden zijn wij twee uitersten, als team haast complementair. Je doelmatigheid, efficiëntie en charisma hebben mij zowel verbaasd als geïnspireerd. Jarich, jou wereld zit vol uitdagingen die je te lijf gaat met enthousiasme, ijver, creativiteit en een vleugje naïviteit. Ik heb met ontzettend veel plezier met je samengewerkt. Lisanne, Esther, Bram en Lisanne, beste kamergenoten. Bedankt voor de bemoedigende woorden, de zinvolle suggesties en de wetenschappelijke discussies; ik kan oprecht schrijven dat jullie dit proefschrift naar een hoger niveau hebben getild. In dit opzicht bedank ik ook Jasper en de rest van de navigatiejongens. Hoewel de onderzoeksgroep soms in tweeën gesplitst lijkt zijn we vaker twee handen op een buik.

Dear Manfred and Torre, it was always a pleasure working with you.

Beste collega zaalartsen van het AvL: Arne, Caroline, Danique, Eva, Henriette, Jacqueline, Jasper, Jony, Lisette, Marije, Niels, Nick, Noor, Pieter, Rosanne, Tessa en Thialda. Pas als je weg bent merk je pas hoe ongelooflijk het warme bad in het AvL is. Ik kijk met een

enorm goed gevoel terug op de tijd als arts-assistent in het AvL. Beste Jos en Arend, hartelijk dank voor het vertrouwen mij een plek te bieden, bedankt voor jullie begeleiding en geduld. Ik bedank ook de WAN hoofden, de verpleging en de afdelingsassistenten voor de geweldige samenwerking.

Vikash, Barry, Caroline en Joost, jullie zijn voor mij de oudste assistenten zoals je ze iedereen gunt. Enthousiast, kundig en enorm gemotiveerd om mij te betrekken en kennis te laten maken met de klinische praktijk. Ontzettend bedankt voor alle hulp, inzichten, vertrouwen en de goede tijd. Beste Kim, Bas en Inez, jullie zijn voor mij oudere broers en zussen in een goed gezin. Annabel, Kasper, Eveline, Florine, Hanna, Michael, Mili, Sergei en Suzanne ik ben ontzettend blij dat ik met jullie heb mogen samenwerken. Ik bedank ook alle chirurgen, de verpleging en het secretariaat voor de fijne en leerzame tijd in het ASz. In het bijzonder wil ik Peter Plaisier en Jurgen Avontuur bedanken voor de het vertrouwen, steun en begeleiding en Joost van der Hoeven, Bas Lamme, Getruid Marres, Eric Belt en Maarten Lijkwan voor de begeleiding, kennis, kunde en leermomenten.

Mijn jongste aandachtsgebied, de ouderengeneeskunde combineert mijn brede interesse in de geneeskunde met betrokken patientencontact en werken in een hecht team. Anneke en Suzanne, ik heb het idee dat ik onder jullie vleugels elke dag groei in dit vak. Marloes Sanne, Anne en Ramil jullie zijn oprecht even gezellig als een assistentengroep.

Beste Martijn, Patricia, Rebecca, Tirza en Marieke. Ik heb het getroffen met jullie als broers en zussen. Van jongs af aan heb ik altijd een hechte band gevoeld. Het is fantastisch hoe genegenheid, uitdaging, prikkeling en ondersteuning met elkaar in evenwicht zijn. Pascal, iedereen zou een vriend als jij moeten hebben. Enthousiast, energiek en relativerend. Rein, jouw nuchtere blik en open deur zijn voor mij een rustpunt, je brede interesse een gangmaker.

Mijn ouders. Bedankt voor het warme nest, de opvoeding en het mogelijk maken van de meest uiteenlopende plannen. Jullie hebben mij alle kansen gegeven om mijzelf te ontwikkelen. Bedankt voor jullie onvoorwaardelijke steun en interesse. Ondanks de zes kinderen in het gezin heb ik nooit het gevoel gehad tijd of aandacht te kort te komen. Nu ik zelf vader ben geworden weet ik dat zoiets veel inspanning moet hebben gekost en waardeer ik jullie des te meer.

Noortje, mijn dochter. Hoewel een cliché, ben jij het mooiste dat er op de wereld is.

Lieve Nicole, al jaren mijn steun en toeverlaat en sinds 2016 zelfs mijn vrouw. Ik ben erg blij dat ik mijn leven met jou mag delen. Bedankt voor je liefde, aandacht en inspiratie.